Ore-proximal surveys in southern Bergslagen: Vena gruvfält and Tunaberg

Alexander Lewerentz, Edine Bakker, Peter Hedin & Dino Leopardi

May 2020

SGU-rapport 2020:16

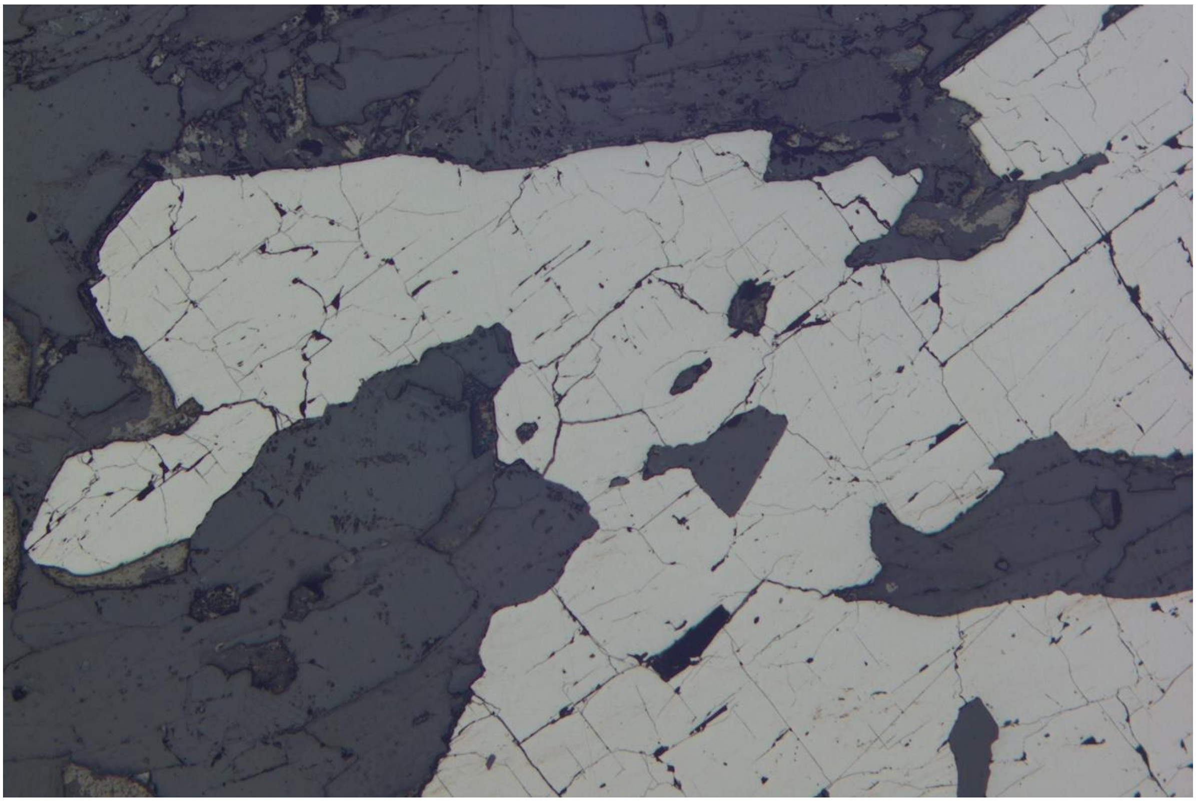

Geological Survey of Sweden

Cover photo: Photomicrograph in reflected light of a cobaltite crystal, light-grey, in a sample from Fredriksgruvorna within Vena gruvfält (sample ALZ180037A). Field of view c. 2 mm.
Photographer: Dino Leopardi

Authors: Alexander Lewerentz (SGU), Edine Bakker (SGU),
Peter Hedin (SGU), and Dino Leopardi (Lund University)
Reviewed by: Dick Claeson
Head of Unit: Ildikó Antal Lundin

Editor: Lina Rönnåsen

Geological Survey of Sweden
Box 670, 751 28 Uppsala
phone: +46 (0)18-17 90 00
e-mail: sgu@sgu.se

TABLE OF CONTENTS

SAMMANFATTNING

Inom ramen för det från näringsdepartementet erhållna ”Uppdrag att kartlägga innovationskritiska metaller och mineral” (diarienummer: N2018/01044/FÖF) har olika geologiska undersökningar i Bergslagen bedrivits. Regeringsuppdraget avrapporterades till näringsdepartementet den 1 mars 2020 och denna SGU-rapport är ett mer detaljerat komplement till den tidigare publicerade regeringsrapporten (Claeson m.fl. 2020).

Områdena kring Vena gruvfält och Tunaberg har valts ut som särskilt intressanta eftersom man här under 1700- och 1800-talen utvann kobolt (Tegengren m.fl. 1924), vilken är en av de av EU och regeringen utpekade innovationskritiska metallerna. Målet med undersökningarna har varit att öka kunskapen om områdets koboltmineraliseringar, med syftet att bättre förstå de bakomliggande bildningsprocesserna och Bergslagens potential för innovationskritiska metaller och mineral. Undersökningarna inkluderade geologisk kartering och provtagning, mikroskopering av tunnslip, mineralkemiska analyser, litogeokemiska analyser, geofysiska mätningar av magnetfält, elektrisk ledningsförmåga och tyngdkraft, samt petrofysiska analyser.

Vid Vena gruvfält påträffades höga halter av kobolt, i synnerhet i gruvfältets sydöstra ände, med halter upp till 1,37 procent, förekommande tillsammans med bland annat koppar, bly och zink. Tredimensionell modellering visar att Cu-Co-mineraliseringarna möjligen kan fortsätta till flera hundra meters djup. Vid Skuru gruvor, en av områdets äldre järnmalmsgruvor, påträffades ovanligt höga halter av sällsynta jordartsmetaller om totalt 0,71 procent, en tidigare okänd förekomst. Geofysiska undersökningar visar att områdets mineraliseringar följer tydliga tyngdkrafts- och magnetfältsanomalier.

Området kring Tunaberg uppvisar en mycket variationsrik geologi, med åtminstone tre typer av mineraliseringar: marmorbunden koppar-koboltmineralisering, vulkanitbunden bly-zinkmineralisering och skarnbunden järnoxidmineralisering. Höga halter av koppar och kobolt påträffades framför allt i området kring Koppartorp, medan den högsta zinkhalten återfanns i varp från Börjelstorpsgruvan. Utöver dessa ämnen påträffades i sulfidmineraliseringarna även ställvis förhöjda halter av bland annat silver, guld och barium. Järnhaltiga skarnbergarter påträffades både norr och söder om sulfidmineraliseringarna kring Koppartorp, vilka till viss del uppvisade förhöjda manganhalter men inte förekomst av ytterligare metaller.

Ytterligare information på svenska om undersökningarna och dess resultat kan läsas i Claeson m.fl. (2020).

ABSTRACT

As part of a special government assignment for investigation of critical raw materials in Sweden, two areas in southern Bergslagen were subject to geological and geophysical survey activities during 2018 and 2019: Vena gruvfält and Tunaberg. The assignment was completed and reported back to the Ministry of Enterprise and Innovation on 1 March 2020 (Claeson et al. 2020).

These two areas were chosen because of their history of cobalt mining in the 18th and 19th centuries (Tegengren et al. 1924), since cobalt is classified as a critical raw material by the European Commission. The goal of the investigations was to increase the understanding of the areas' cobalt mineralisations, with the aim to better understand the underlying formation processes and the potential for critical raw materials in Bergslagen. The survey activities included geological mapping and sampling, microscopy of thin section, mineral chemical analyses, lithogeochemical analyses, geophysical measurements of the magnetic field, electric resistivity and the gravitational field, as well as petrophysical analyses.

Elevated cobalt concentrations were confirmed at Vena gruvfält, especially in the southeast part of the area, with up to 1.37% cobalt in a whole-rock sample. Within the Co-bearing sulphide mineralisation, elevated levels of copper, lead, and zinc were also detected. Three-dimensional modelling shows that the copper-cobalt mineralisations may continue to depths of several hundreds of metres. At Skuru gruvor, one of the areas historical iron ore mines, anomalous concentrations of rare earth elements were found (0.71% total REE), a previously unknown REE occurrence. Geophysical investigation shows that the area's mineralisations tightly follow positive magnetic and gravimetric anomalies.

The Tunaberg area displays a complex geology, with at least three different types of mineralisations: marble-hosted copper-cobalt mineralisations, supracrustal rock-hosted lead-zinc mineralisations, and skarn-hosted iron-oxide mineralisations. The analyses show that high concentrations of cobalt and copper were especially frequent near Koppartorp, whereas the highest zinc concentrations were detected in waste piles at Börjelstorpsgruvan. Additional elements analysed and found in elevated concentrations from the sulphide-mineralized rocks include silver, gold and barium. Iron-rich skarns were found both north and south of the main sulphide-mineralised area. Except for local manganese enrichment, no other element was found to occur at elevated concentrations.

VENA GRUVFÄLT

Alexander Lewerentz, Edine Bakker, Peter Hedin och Dino Leopardi

This chapter is a revised and extended version of the previous report by Lewerentz et al. (2019).

Background and previous studies

Vena gruvfält – the Vena mining area – is located just east of the hamlet of Åmmeberg, Askersund Municipality, southern Örebro County. The area hosts hundreds of historical mines (Fig. 1), where iron and sulphide ores were mined from at least the 16th century and onwards (Erdmann 1889). The Vena copper and cobalt mines were active between the years of 1770 and 1880, which resulted in production of in total c. 416 metric tonnes of ore with an average concentration of 0.1–0.5% Co (Kommerskollegium 1877; 1880; 1881; Tegengren m.fl. 1924).

A description of the large-scale geology of the Bergslagen Ore Province is presented in Stephens et al. (2009). The area around Vena gruvfält was previously mapped and surveyed by Erdmann (1889), Henriques (1964), and Wikström & Karis (1991). The primary volcanic stratigraphy in the area was studied by Kumpulainen et al. (1996). Descriptions of the mineralisations at Vena gruvfält and its immediate vicinity are available in Blomberg & Holm (1902), Tegengren et al. (1924), Geijer & Magnusson (1944), Henriques (1964), and Sundblad (1994). Vena gruvfält constitutes type locality for the Pb-Cu-Sb-Bi-sulfosalt minerals kobellite (Setterberg 1839) and izoklakeite (Zakrzewski & Makovicky 1986).

Airborne geophysical surveys were done over the region including Vena in 1980, as part of the regional surveys of southwestern Bergslagen during 1970's and 1980's. Gravity data have been collected over the years with relatively sparse sampling in the area. These provided the data for the geophysical map compilations in Stephens et al. (2009). In 1982, detailed surface surveys with magnetometry and induced polarisation was done around the Lövfallsgruvorna area, just southeast of Vena district (Fig. 1). Only a handful of petrophysical samples have previously been collected in the area, and hence information about bedrock density and magnetic properties that can be used for correlation with geophysical measurements have been lacking.

Field observations and sampling

Geological mapping was conducted by Edine Bakker and Alexander Lewerentz during two periods: 28 August – 14 September 2018, and 13 May – 31 May 2019. Dino Leopardi (Lund University) has as part of his M.Sc. thesis work partaken in the fieldwork, as well as examined and analysed previously collected material. The geological mapping was mainly concentrated to the historical mining area and its immediate vicinities, which included examination of outcrops but also old mine pits and waste piles. Further away from the actual mining area, outcrops and historical iron ore mines were more sporadically investigated. West of lake Åmmelången, near Dampetorp farm, a small cluster of historical mines and their surroundings were surveyed in more detail. In addition to fieldwork, drill cores from both Dampetorp, available in SGU's archives in Malå, and Vena gruvfält, held in archives in Zinkgruvan, were described and sampled. We would like to extend our thanks to Zinkgruvan Mining AB, and especially Anja Hagerud and Filip Ivarsson, for providing access to core material and assistance at the core logging facilities at Zinkgruvan.

In total 293 localities were described and added to SGU's outcrop database (swe: *hälldatabasen*), 98 samples analysed for whole-rock geochemical characterisation, and 49 thin sections or ore sections prepared for petrographic and mineral chemical analyses (Fig. 2). Coordinates for below mentioned, depictured and discussed outcrops and samples are presented in Table 1.

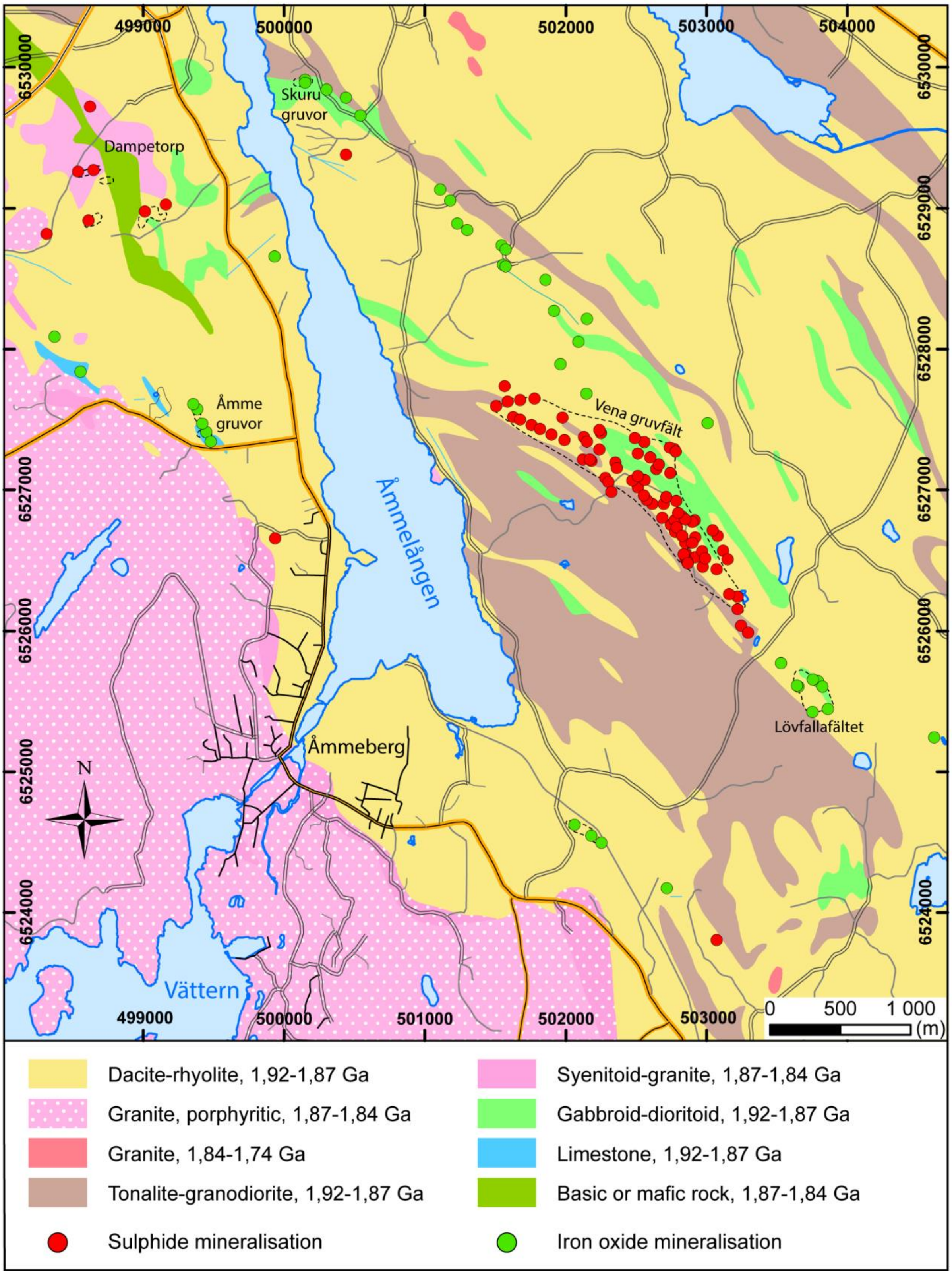

Figure 1. Geological map of the studied area, including locations for the many historical iron oxide and sulphide mines. Most sulphide mineralisations are found within the actual Vena gruvfält, with minor occurrences also present at Dampetorp west of lake Åmmelången. Iron mineralisations include Lövfallafältet southeast of Vena gruvfält, minor occurrences northwest of Vena gruvfält towards Skuru gruvor, as well as Åmme gruvor west of lake Åmmelången. Geological information is drawn from SGU's bedrock databases, mineralisations from the mineral resources database. Coordinates in SWEREF99tm.

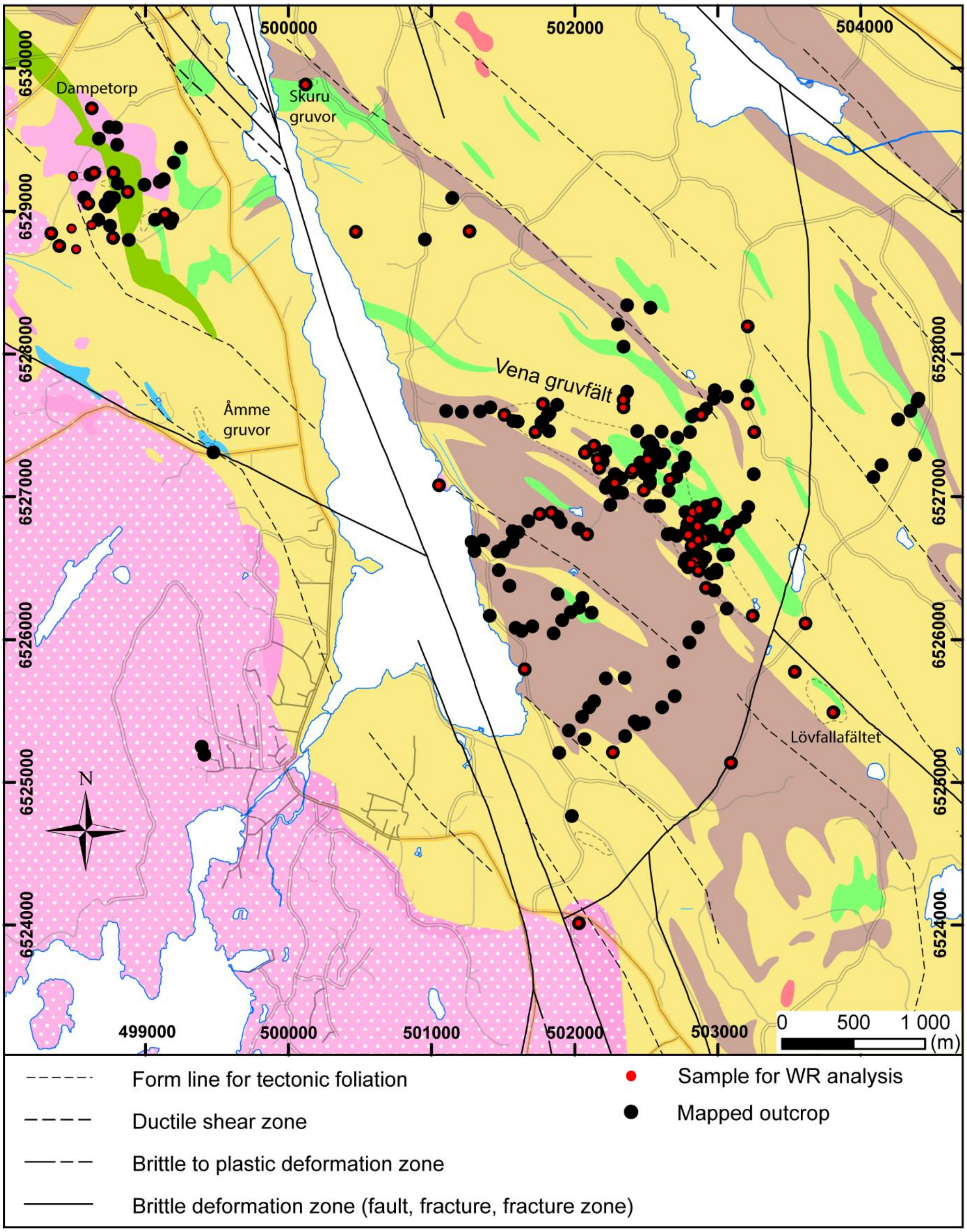

Figure 2. Geological map of the studied area with deformation zones and other structures shown. Black dots mark mapped outcrops, red dots mark locations for whole-rock geochemical samples. Rock types in accordance with the legend in Figure 1. Coordinates in SWEREF99tm.

Table 1. List of coordinates in SWEREF99TM for selected outcrops and samples.

Outcrop ID*	SWEREF99TM N	SWEREF99TM E
ALZ180002	6525791	501649
ALZ180033	6527650	503210
ALZ180033	6527650	503210
ALZ180037	6526481	502864
ALZ180045	6526604	502858
ALZ180052	6526692	502849
ALZ180067	6526735	502649
ALZ180072	6526907	502871
ALZ180076	6526946	502984
ALZ180082	6526923	502853
ALZ180085	6524013	502029
ALZ180086	6526617	501300
ALZ180087	6527078	501051
ALZ180089	6526650	502816
ALZ190034	6526164	503246
ALZ190040	6528809	498776
ALZ190046	6529253	498615
ALZ190059	6525457	502052
ALZ190065	6529051	498603
ALZ190067	6529134	498878
ALZ190072	6529439	499251
EDB180007	6528798	500953
EDB180034	6527198	502170
EDB180057	6527274	502771
EDB180069	6527256	502189
EDB190023	6526658	502819
EDB190035	6528755	498399

*Sample IDs are identical to their respective Outcrop IDs, with the addition of a letter: e.g. ALZ180054B.

Description of mapped rocks

Metavolcanic rocks of the Mariedamm unit occupy most of the mapped area (Kumpulainen et al. 1996). They are Svecokarelian in age and include mainly rocks of rhyolitic to andesitic composition. Mineral assemblages include quartz, plagioclase, K-feldspar, biotite and muscovite, locally with addition of orthopyroxene, clinopyroxene, amphibole, zoisite, clinozoisite, garnet, cordierite, and andalusite. Tourmaline, zircon, apatite, monazite, and rutile occur as accessory minerals. See Appendix 1 for a sample-specific mineralogical summary.

The degree of deformation and metamorphic recrystallisation is very variable within the area; some outcrops exhibit fairly well-preserved primary volcanic textures and structures (Fig. 3a, 3e), whereas others are migmatised to an extent where all primary features are obliterated (Fig. 3b). Even the least affected rocks always show a penetrative foliation. The least-affected volcanic rocks can be subdivided into three principal groups:

1. Quartz-rich and feldspar-poor, ash-siltstones to -sandstones, often showing compositional or textural layering, locally with mm- to cm-wide biotite-rich zones (Fig. 3c–d).

2. Fine-grained rocks with phenocrysts of quartz, K-feldspar and amphibole up to 10 mm across, locally also xenolith-bearing (Fig. 3a).
3. Lapillistones or lapilli tuffs with up to cm-sized pumice fragments in a fine-grained, quartz-rich matrix (Fig. 3e–f).

Figure 3. A. Rhyolite-dacite with phenocrysts of amphibole (EDB180007). Photo: Edine Bakker. **B.** Migmatitic rock of presumably volcanic origin, observation from the Dampetorp area where the migmatisation generally is stronger (ALZ190040). **C-D.** Field and microscope photograph (cross-polarised light; xpl) of a quartz-rich, fine-grained supracrustal rock. Elongate porphyroblasts of amphibole, up to 0.5 mm along the c-axis, indicate a volcanic origin (ALZ180052B). Photo: Alexander Lewerentz. **E.** Weakly deformed metavolcanic rock with primary accretionary lapilli structure (EDB180069). Photo: Edine Bakker. **F.** Micrograph (plane-polarised light; ppl) of c. mm-sized lapilli fragments in a fine-grained, quartz-rich matrix. The primary textures are overprinted by tectonic foliation, which is accentuated by parallell-orientated biotite grains (ALZ180067A). Photo: Alexander Lewerentz. Abbreviations according to Whitney & Evans (2010).

Groups 1 and 3 strongly indicate an extrusive formation environment, whereas group 2 possibly also includes sub-volcanic, intrusive rocks. The presence of carbonate horizons indicates that the volcanic rocks, or at least parts of the stratigraphy, were deposited in a marine environment.

The origin of the fine-grained, quartz-rich rocks, here interpreted as volcanic ash-siltstones (Fig. 3c), is previously debated. Different interpretations include hydrothermally altered volcanic rocks (Åberg 1988), volcanic rocks with partial sedimentary influx (Åberg 1988; Wikström & Karis 1991), and purely sedimentary rocks (Henriques, 1964). The occurrence of amphibole porphyroblasts indicates a composition more expected for rocks of volcanic origin, i.e. primary deposited or possibly reworked volcanic material; however, partial influx of detritus cannot be ruled out. Localised, hydrothermally altered zones constitute a plausible explanation for the genesis of the biotite-rich horizons.

Recrystallisation, deformation and anatexis is generally stronger both in the areas southwest and northeast of Vena gruvfält, as well as in the Dampetorp area. As a result of variable degree of coarsening due to metamorphism, these rocks show inhomogeneous grain size, ranging from fine-grained to finely medium-grained, which obscures the primary grain size. This makes more precise volcanogenetic interpretations extremely difficult. The degree of anatexis varies from sporadic, mm-wide, K-feldspar-rich veinlets to extensive migmatisation with well-developed K-feldspar-rich leucosomes and biotite-rich melanosomes up to a few cm in width. Some of the most extensively migmatised rocks are mapped as of volcanic origin merely by spatial reference to less-affected rocks. Folding, locally ptygmatic, and accompanied oblique shearing of the tectonic foliation are common structures. Metamorphic assemblages are further discussed in the chapter *Metamorphism*.

Carbonates and skarns were found in outcrops, waste piles and drill cores. Our observations indicate that they occur as up to metre-thick horizons within the volcanic stratigraphy. These vary between almost pure calcite marbles (Simeonov 1990, Wasström 1991a, 1991b, 1991c) and horizons entirely replaced by garnet-pyroxene-epidote skarns (Fig. 4). This variation may reflect the degree of volcanic material influx during primary deposition. Skarns were also observed and sampled from waste piles near Galtgruvan. The sampled material comprises a fine- to coarse-grained inequigranular rock, with dissemination of up to 50 vol.% sulphides. Major minerals include garnet, clinozoisite-epidote, diopside-hedenbergite, plagioclase, calcite, and quartz, minor minerals K-feldspar, titanite, and actinolite-tremolite. Muscovite, chlorite, zircon and siderite occur as accessory phases or alteration products.

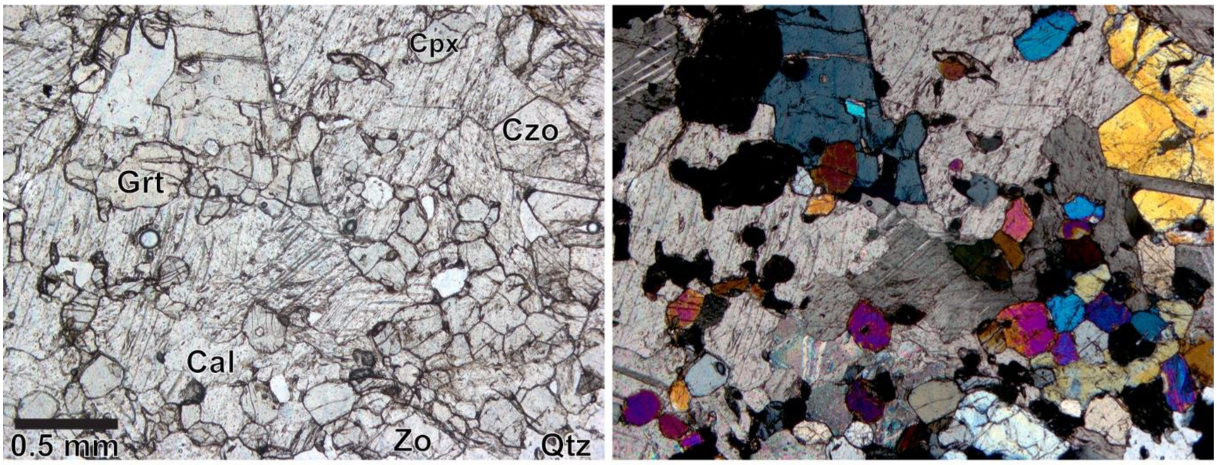

Figure 4. Photomicrographs of a mineralized skarn sampled from waste piles at Galtgruvan (ALZ180089A), which is composed of calcite, clinozoisite, zoisite, garnet, clinopyroxene and quartz. Left photo in ppl and right in xpl. Photos: Alexander Lewerentz.

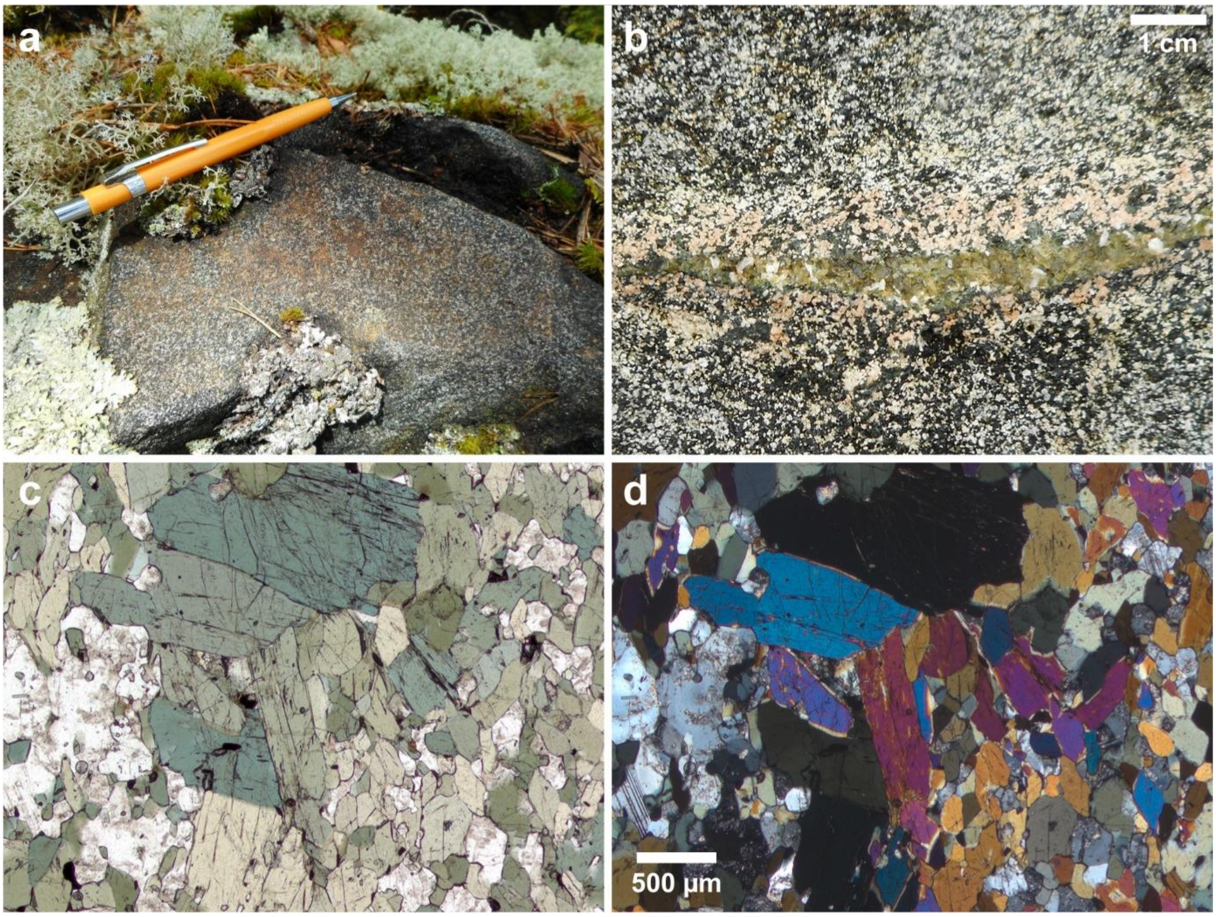

Figure 5. A. Amphibolite (ALZ180045). **B.** K-feldspar associated with an epidote-healed fracture in amphibolite (ALZ180082). **C.** Micrograph in ppl, and **D.** in xpl, of an amphibolite in thin section with hornblende and plagioclase as the major minerals (ALZ180033). Photos: Alexander Lewerentz.

Amphibolite occurs as thin, stretched bodies that can be traced for hundreds of meters within the metavolcanics (Fig. 1). They are mostly equigranular and varies from fine-grained to finely medium-grained (Fig. 5a), although unevenly grained to porphyroblastic varieties were also observed. Tectonic foliation is observed in biotite-bearing outcrops, whereas others are massive due to the lack of platy minerals. Major minerals include hornblende, plagioclase, chlorite, epidote, and biotite, with minor quartz, K-feldspar, and titanite, as well as accessory apatite, graphite, carbonates, and rutile (Fig. 5c–d). See Appendix 1 for a sample-specific mineralogical summary. K-feldspar predominantly occurs in association with localised, epidote-healed fractures (Fig. 5b).

Granodiorite-tonalite of Svecokarelian age mainly occurs to the southwest of Vena gruvfält (Fig. 1); however, our observations indicate that their lateral extent previously has been exaggerated. These rocks are generally finely medium-grained (Fig. 6a), but both finer and coarser grained rocks are locally observed. In some outcrops they are equigranular, inequigranular in others, and more rarely porphyritic with phenocrysts of K-feldspar. Xenoliths of metavolcanic rocks are locally present. Outcrops with enclave-bearing rocks indicate magma mingling incorporate material from a different magma source. Most outcrops exhibit tectonic foliation, some are gneissose and partially migmatised (Fig. 6b). Main minerals include quartz, plagioclase that is locally sericitized, K-feldspar locally with myrmekite, and biotite, with minor muscovite, as well as accessory apatite, zircon, pyrrhotite, hematite, and covellite (Fig. 6c–d). Moreover, occurrences of garnet porphyroblasts and retrograde biotite chloritization is further described below.

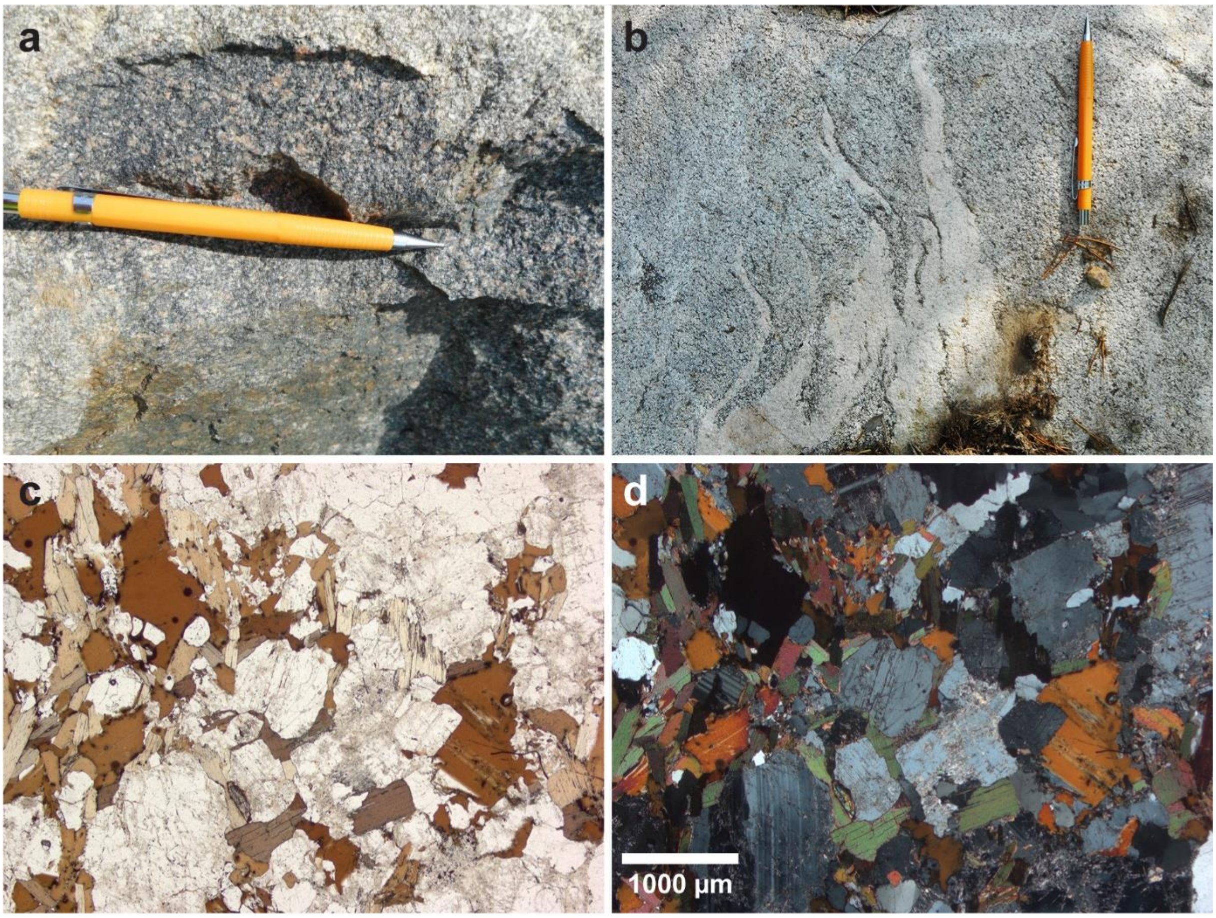

Figure 6. A. Equigranular, finely medium-grained granodiorite (ALZ180086). **B.** Partially migmatised granodiorite (ALZ180017). **C.** Photomicrograph of a finely medium-grained granodiorite in ppl, and **D.** xpl, showing plagioclase, K-feldspar, quartz and biotite as the main minerals (ALZ180085A). Photos: Alexander Lewerentz.

Granite to alkali granite occur as lenses within the metavolcanics, which vary from metres to tens of metres in size. The rocks are inequigranular and medium- to coarse-grained. They are leucocratic and remarkably reddish pink in colour, which reflects a K-feldspar-rich mineral assemblage that generally lacks mafic minerals. In addition to K-feldspar, quartz and minor biotite is also observed. Some outcrops show a massive fabric (Fig. 7a); however, in most cases a distinct tectonic foliation is accentuated by the parallelization of platy biotite crystals (Fig. 7b). These rocks are interpreted as syn-orogenic, possibly locally derived melts that formed as a response to migmatisation of the volcanic rocks. The anomalously red colour may be due to fluid-induced hematite staining of K-feldspar (Putnis et al. 2007), which would indicate pervasive metamorphic fluid flow and subsequent fluid-rock interaction.

Syenitoid occurs mainly as a larger body in the southern and western parts of the studied area (Fig. 1), which vastly extends farther west and south. Most outcrops show a massive, coarse-porphyritic, rapakivi-textured rock with phenocrysts of K-feldspar in a medium-grained matrix of quartz, plagioclase and minor biotite (Fig. 8a). In one outcrop on the east side of Lake Åmmelången (Fig. 1), the syenitoid is equigranular and lack phenocrysts but in every other aspect similar to other syenitoids in the study area (Fig. 8b). None of the mapped syenitoids show tectonic foliation nor any other macroscopic-scale metamorphic textures or structures. In addition to previously stated major minerals, accessory chlorite, epidote and zircon are also observed. Under the microscope, K-feldspar show a dusted appearance (Fig. 8 c–d), which is indicative of interaction with a late-stage magmatic fluid or later crustal fluid (Putnis et al. 2007). Together with bulging grain boundaries that indicate some degree of recrystallization (Fig. 8c–d), this possibly implies emplacement in a late-orogenic setting or just shortly after the termination of the Svecokarelian orogeny.

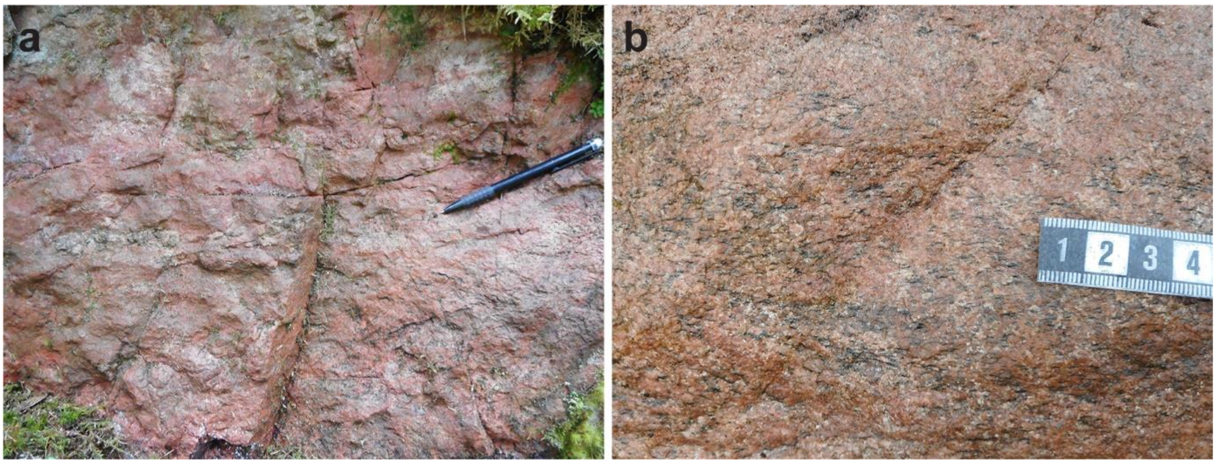

Figure 7. A. Inequigranular, K-feldspar-rich alkali granite that seemingly exhibits a massive fabric (ALZ190059). **B.** Alkali granite with tectonic foliation accentuated by the parallelization of biotite (ALZ190065). Photo: Alexander Lewerentz.

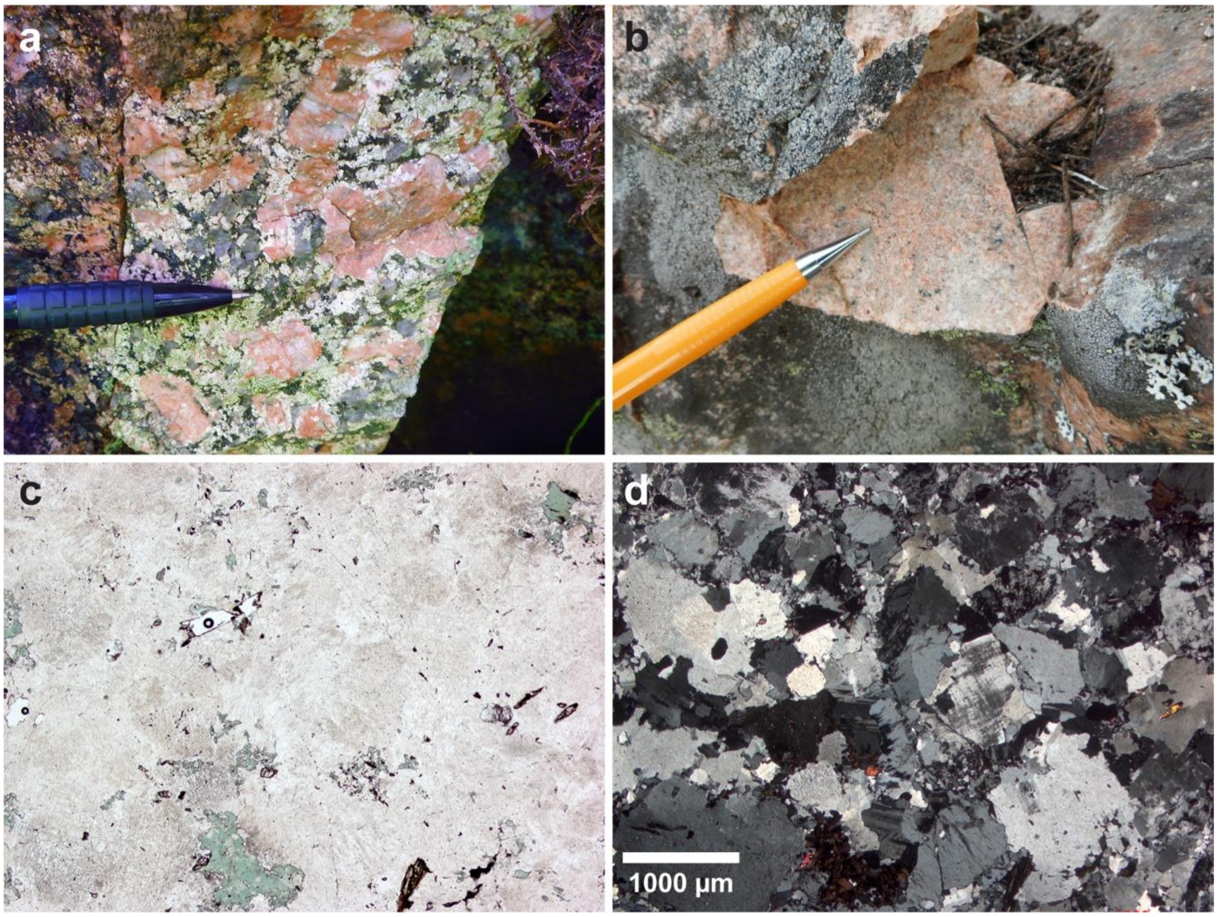

Figure 8. A. Massive, medium-grained, coarse-porphyric syenitoid ("Askersund granite") with phenocrysts of K-feldspar that show rapakivi texture (ALZ190046). **B.** Field photograph of equigranular syenitoid comprised of K-feldspar, quartz, plagioclase with minor chlorite, epidote and zircon (ALZ180087). **C.** Photomicrograph in ppl, and **D.** xpl, of the rock in B. Bulging grain boundaries indicate some degree of recrystallisation. Photos: Alexander Lewerentz.

Pegmatite occurs as dykes that show a massive fabric and crosscut tectonic foliation (Fig. 9a). The thickness of the dykes varies from centimetre to metre scale. They mainly comprise quartz and K-feldspar, with subordinate plagioclase, micas and tourmaline.

Composite mafic-felsic rock, an intrusive rock or rock suite comprised of two distinct components, occurs mainly in the Dampetorp area. Based on the previously mapped extents of this rock (Fig. 1), the rock is interpreted as a composite mafic-felsic dyke (cf. Nilsson 1992). The felsic component varies from fine- to medium-grained and in some cases contain phenocrysts or xenocrysts and xenoliths. Quartz, K-feldspar and plagioclase are common minerals. The mafic component is generally aphanitic to fine-grained, locally with phenocrysts of plagioclase. Field relations between the two components are seemingly complex: in some outcrops it is evident that the felsic component intrudes and fractures the mafic component (Fig. 9b), whereas other outcrops are harder to interpret or even indicate the opposite relationship (Fig. 9c).

Dolerite is found in one outcrop just east of Lake Åmmelången, where it previously has not been mapped (Fig. 9d). The rock is aphanitic and shows a massive fabric. Due to poor exposure, the orientation of the c. 10 m wide dyke was not mapped out; however, lineament interpretation of the aeromagnetic data indicates presence of a north-northwest–south-southeast trending dyke that intersects the observed outcrop. Two generations of post-Svecokarelian dolerite dykes occur in the area: the west-northwest–east-southeast trending 1.60–1.56 Ga Breven-Hällefors dolerites (BHD) and the north-northwest–south-southeast trending 0.98-0.95 Ga Blekinge-Dalarna dolerites (BDD; Söderlund et al. 2005). A BDD affinity is more likely for the dolerite dyke based on the geophysical evidence. Further evidence comes from lithogeochemical characterization that shows relatively high contents of Zr and Sr, which according to Risku-Norja (1992) and Solyom et al. (1992) is typical of BDD.

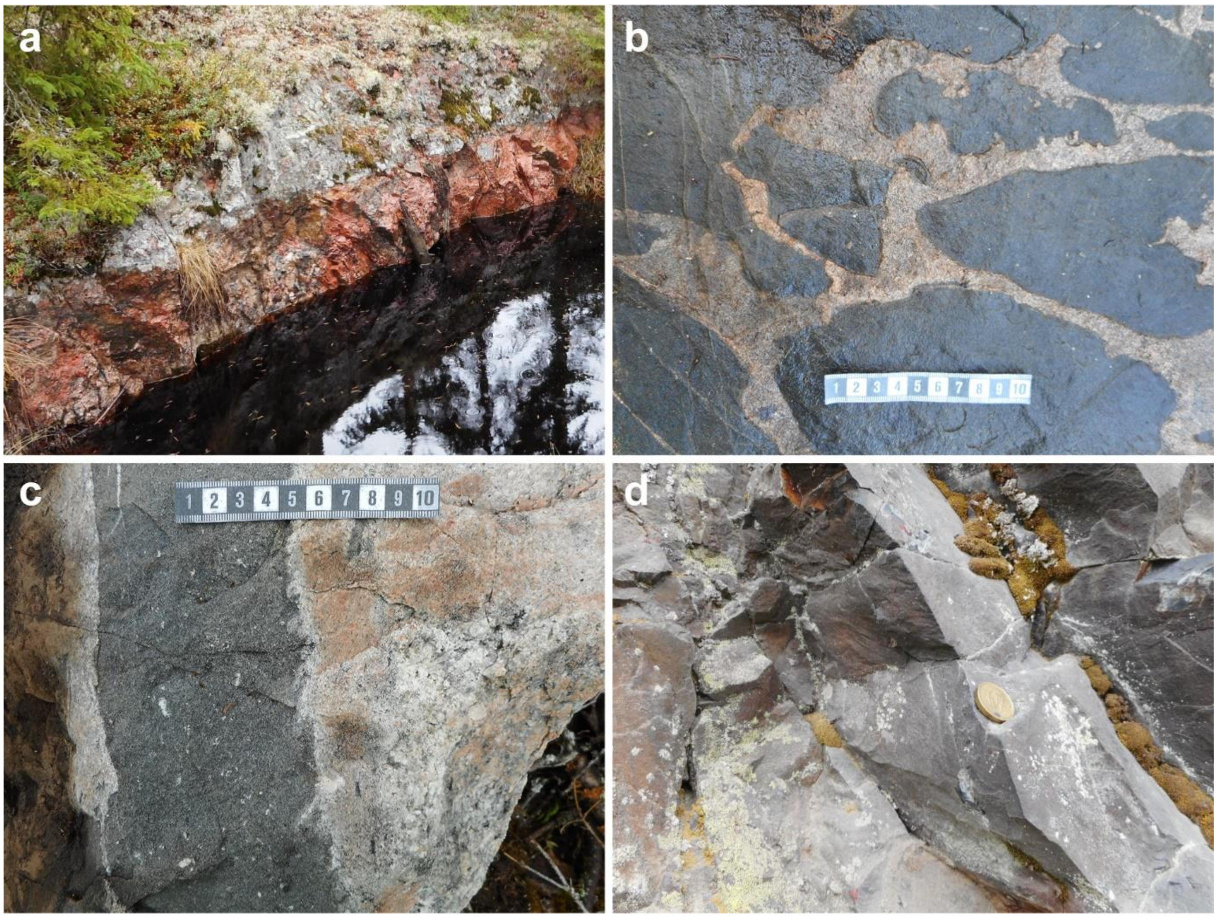

Figure 9. A. Pegmatite dyke, here as part of the wall to one of the area's many historical mine pits (EDB180057). Photo: Edine Bakker. **B.** Composite mafic-felsic rock in which the felsic component evidently intrudes into and occurs as fracture filling between fragments of the mafic component (ALZ190072). Photo: Alexander Lewerentz. **C.** Composite mafic-felsic rock, in which the mafic component rather seems to intrude into the felsic component (ALZ190067). Photo: Alexander Lewerentz. **D.** Dolerite dyke (ALZ180002). Photo: Alexander Lewerentz.

Structural observations

All measurements are given according to the right-hand rule. Steeply dipping and northwest-southeast striking penetrative foliation or gneissose structures are observed in most of the area's Svecokarelian rocks. Mineral lineation occurs within these planar structures. Folding of the foliation is locally observed with axes measured at c. 145/50, which together with measurements of planar structures may indicate a regional-scale, southeast-verging, tight to isoclinal fold (Fig. 10a). This would concur with previous interpretation that Vena gruvfält lies within an isoclinal fold (Wikström & Karis 1991). Preliminary interpretations Lewerentz at al. (2019) mention the possibility of additional foliation and fold generations; however, collection of additional data shows that the previously postulated two foliation groups are statistically inseparable.

The Dampetorp area is structurally more complex than Vena gruvfält. Gneissose structures have highly variable orientations and no regional trend is evident (Fig. 10b). This is possibly due to that the structures were wrapped around the post-metamorphic intrusion of the Askersund granite.

Field relations and geochronology

The oldest rocks in the area are Svecokarelian (sub-)volcanic rocks of the Mariedamm unit (c. 1.90 Ga; Kumpulainen et al. 1996). Preliminary U-Pb SIMS analyses of zircon grains from a rhyolite in the southeast parts of Vena gruvfält indicate a formation age of c. 1.89 Ga (SGU, unpublished data), additional analyses are planned for and final results to be published in a separate SGU report. Skarn rocks likely represent limestone or carbonate-bearing horizons within the volcanic succession and are coeval with the volcanism.

Amphibolites occur as long-stretched bodies within the metavolcanic rocks. These are parallel to tectonic foliation and may therefore represent sills. Alternatively, they are dykes that later were

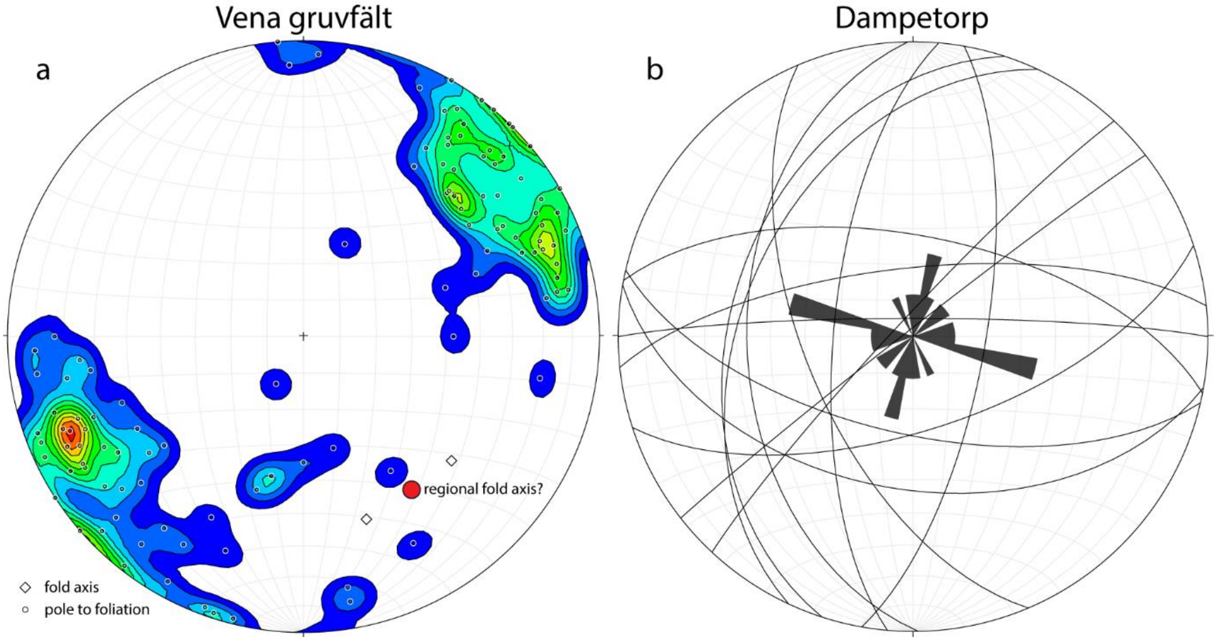

Figure 10. A. Stereographic projection of poles measured foliations (n = 115) and fold axes (n = 2) in the area around Vena gruvfält. These may indicate a regional isoclinal fold structure with fold axis at c. 145/45. Poles to foliation are contoured with 1% area contours (interval 1, 3σ). **B.** Stereographic projection of measured foliations in the Dampetorp area (n = 14). As demonstrated by the rose diagram, these show a much more complex pattern, which possibly indicates that the foliation partially wraps around the intrusion of the Askersund granite. Both plots are equal-area projections on the southern hemisphere.

parallelized by tectonic shearing. The amphibolites likely intruded shortly after emplacement of the metavolcanic rocks (Stephens et al. 2009).

Svecokarelian granodiorites intruded at 1.90–1.87 Ga (Stephens et al. 2009). Xenoliths of metavolcanic rocks observed at Vena gruvfält clearly show that they postdate emplacement of the volcanic rocks.

Svecokarelian regional orogenic metamorphism took place c. 1.87–1.84 Ga (Stephens et al. 2009) and affected the previously formed rocks in the area around Vena gruvfält. Bodies of alkali granite are interpreted as syn-orogenic, localised melts, related to this event.

Late- to post-orogenic, unmetamorphosed syenitoids belonging to or associated with the Askersund granite were emplaced at 1848±15 Ma (Persson & Wikström 1993), prior to which regional orogenic metamorphic activity must have ceased. Unmetamorphosed pegmatites observed in the Vena gruvfält area are likely late derivates related to these intrusions. Some 13 km northwest of Dampetorp, the Askersund granite is intruded by the likewise unmetamorphosed Nygård norite pluton, whose emplacement age has been determined to 1850±9 Ma (Claeson & Andersson 2000). The composite mafic-felsic dyke observed near Dampetorp is possibly related to or of the same age as the Nygård pluton. As an implication of the lack of metamorphic record in these rocks, Vena gruvfält cannot have been affected in a major way by the, in some studies postulated, 1.83–1.79 Ga metamorphic event or events (Persson & Sjöström 2002, Stephens et al. 2009).

Dolerites emplaced either at 1.60–1.56 Ga or 0.98–0.95 Ga represent the youngest rocks in the area. See description above for further information.

Description of mineralisations

Ore mineral assemblages

Reflected light microscopy and scanning electron microscope (SEM) analysis of polished thin sections show that the mineralisation at Vena gruvfält was formed in several (minimum three), partly overlapping steps, which resulted in the precipitation and remobilization of different assemblages of ore minerals (Fig. 11a–f). The most common sulphide minerals are chalcopyrite, followed by pyrrhotite, sphalerite, and pyrite (Appendix 1B). The earliest formed ore minerals, by relative comparison, are pyrite and pyrrhotite. Some sphalerite and galena formed together with cobalt minerals, but mostly later together with chalcopyrite. The mineralisation is mostly disseminated with local aggregates and veinlets (Fig. 11c–f). In cobalt-rich samples, megacrysts of cobaltite locally occur, inclusions of metamorphic biotite indicate that these are porphyroblasts.

Supergene alteration of sulphide minerals includes the breakdown of chalcopyrite into secondary copper minerals like covellite and delafossite. Pyrrhotite is commonly altered to pyrite and magnetite along edges and cracks, of which pyrite locally alters further into marcasite. Late cracks filled with siderite or hematite also occur. The interpreted paragenetic sequence of the formation of the mineralisation is presented in Table 2.

The focus of the investigation has been the occurrence of cobalt within Vena gruvfält. Cobaltite has been identified in at least five samples. Besides cobaltite, the cobalt-bearing minerals costibite, willyamite, danaite (Co-arsenopyrite), cobaltoan pyrite, cattierite-vaesite, carrollite and possibly glaucodot have been observed (Fig. 12). A parallel study also identified Co-pentlandite in the form of exsolution lamellae in pyrrhotite as well as skutterudite (Leopardi 2020). Cobaltite locally contain inclusions of sphalerite and molybdenite (Fig. 11b). Bismuthinite occurs as inclusions, as well as at the edges of cobaltite. Native bismuth and galena are exsolved from or included in danaite (Fig. 12c). Galena occurs intergrown with costibite (Fig. 12a–b). A more detailed description of the different ore mineral assemblages is offered by Leopardi (2020).

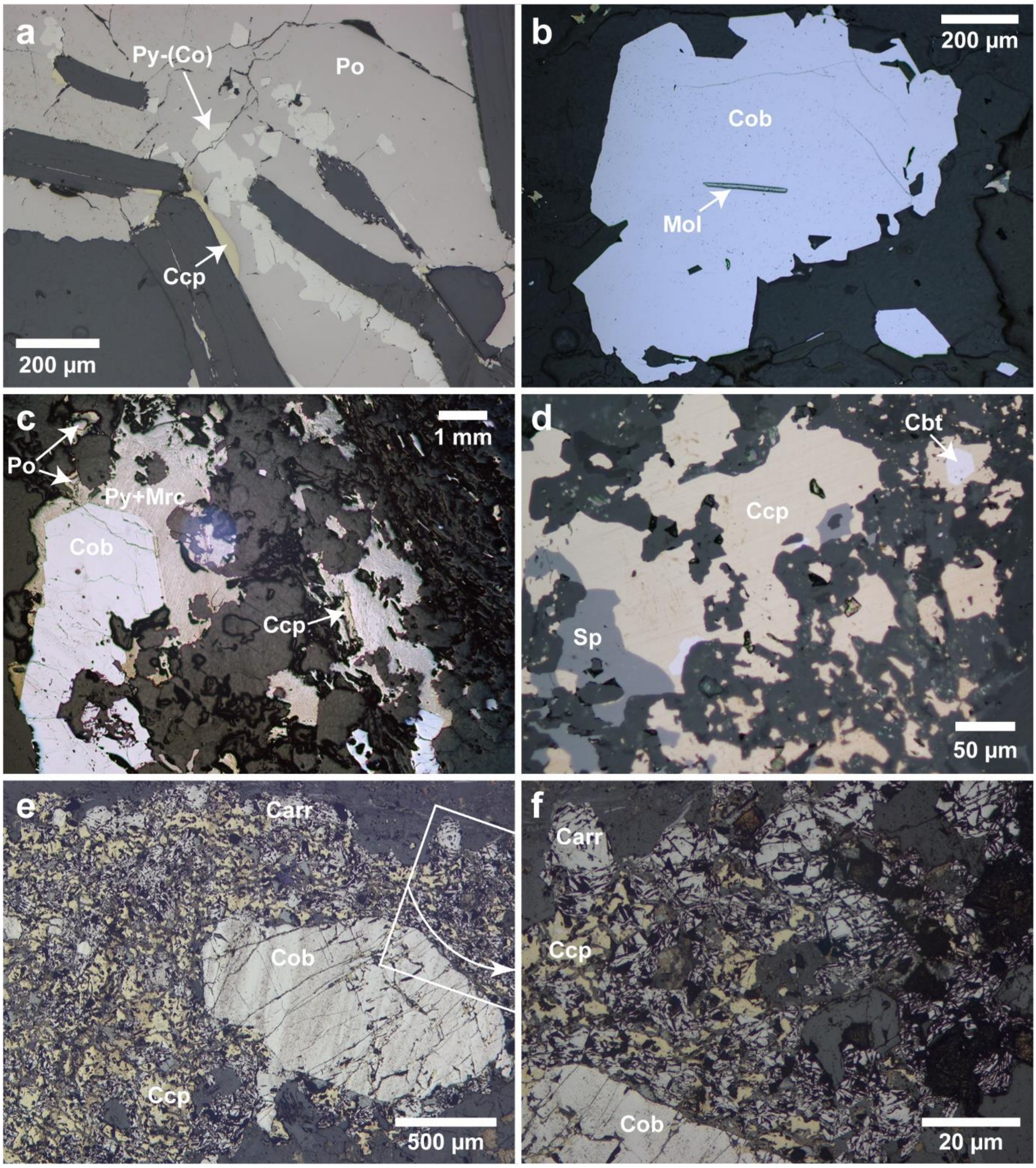

Figure 11. Photomicrographs in reflected light. **A.** Co-Pyrite in pyrrhotite with chalcopyrite on the edges (ALZ190088A, drill core VENA9004, interval 567,40–567,65 m; Wasström 1991c). Photo: Dino Leopardi. **B.** Inclusion of molybdenite in cobaltite (Cob; EDB190021A, drill core VENA9002, interval 415,3–416,65 m; Wasström 1991a). Photo: Edine Bakker. **C.** Cobaltite surrounded by pyrite + marcasite and lesser pyrrhotite and chalcopyrite (drill core as B). Photo: Edine Bakker. **D.** Costibite (Cbt) intergrown and surrounded by disseminated chalcopyrite and sphalerite (EDB190023B). Photo: Edine Bakker. **E.** Strongly fractured cobaltite, carrollite (Carr) and chalcopyrite (ALZ180072A), and **F.** close-up of the upper right part of E. Carrollite appears more brittlely deformed than cobaltite. Photo: Dino Leopardi.

Table 2. Paragenetic sequence diagram of the sulphide mineralization at Vena gruvfält. The darker the colour of the block, the more abundant the mineral is in a certain relative time period. Question marks point out that the relative timing is uncertain due to limited number of observations. The blue box outlines the main Co-mineralising event and the associated Co-minerals. For the secondary and supergene minerals, the predecessor mineral is indicated.

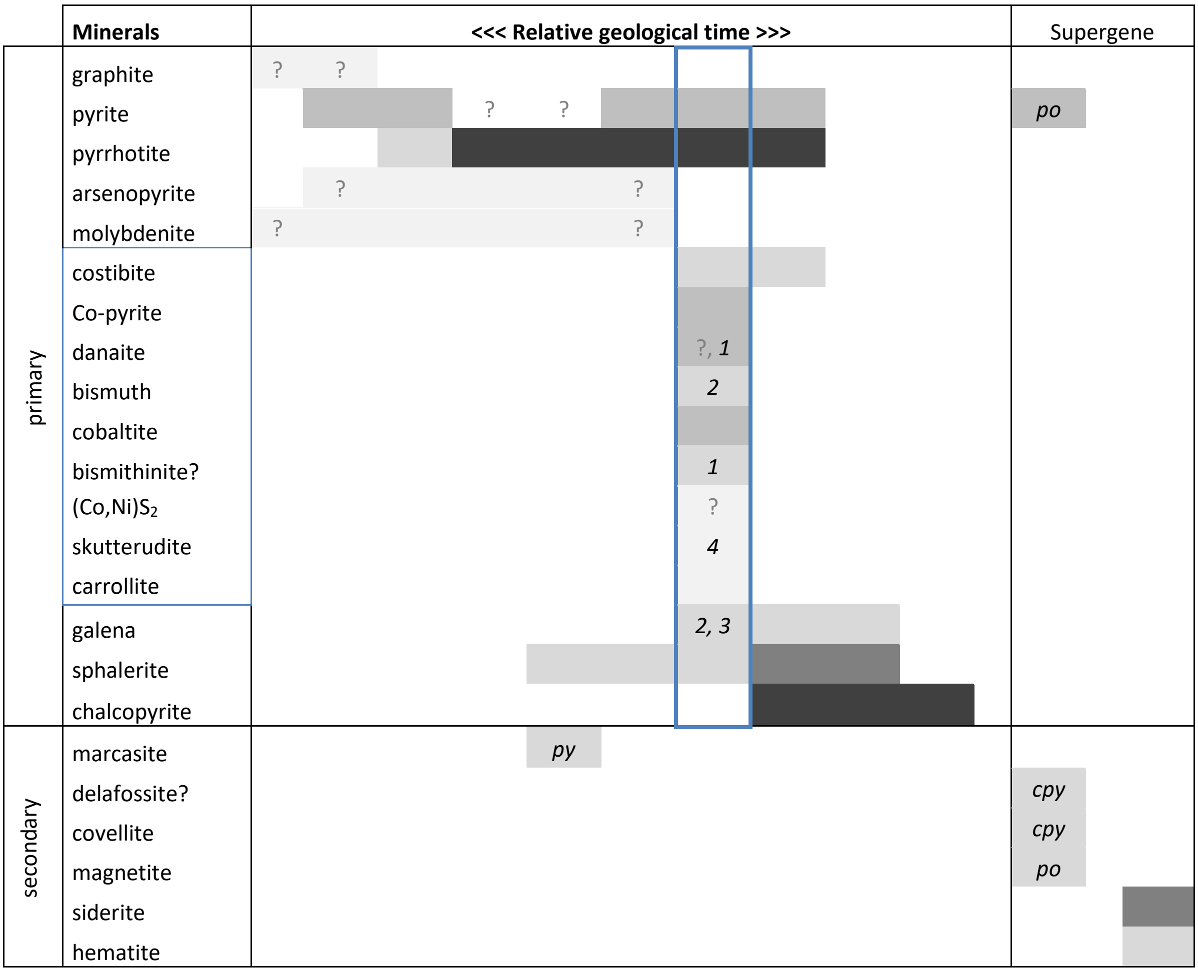

1 = intergrown with cobaltite
2 = exsolved from or included in danaite
3 = intergrown with costibite
4 = included in danaite

Iron-oxide mineralisations occur to the south, south-east and north of Vena gruvfält (Fig. 2), many of which have previously been mined for iron ore. Magnetite is the main ore mineral, but minor sulphides also occur, such as pyrrhotite, pyrite and chalcopyrite. These mineralisations are hosted by or occur in association with skarn bands or lenses within the metavolcanic sequence, i.e. much like many other marble-/skarn-hosted magnetite deposits in Bergslagen (e.g. Jansson & Allen 2013). The associated skarn assemblages comprise mainly amphiboles, epidote group minerals and garnet. Minor contents of quartz, feldspars and biotite likely indicate a protolith made up of a mixture of calcareous and volcanic or sedimentary material. A sample collected from Skuru gruvor (6529885/500122) stands out from the rest of the sampled iron-oxide mineralisations: this sample is strongly enriched in LREE with ΣREE = 0.71 wt.%. The main REE-bearing mineral was identified as allanite-(La) or a 50/50-component between allanite-(La) and allanite-(Ce), which is intergrown with magnetite, pyrrhotite, chalcopyrite, and apatite-(F), as shown in Figure 13. In addition to allanite, thin sheets of the fluorocarbonate mineral parisite-(La) were identified. The sheets show no signs of deformation whatsoever, which strongly indicates post-tectonic remobilisation of LREE, especially for La. See Appendices 1 and 3 for detailed assemblages and mineral compositions.

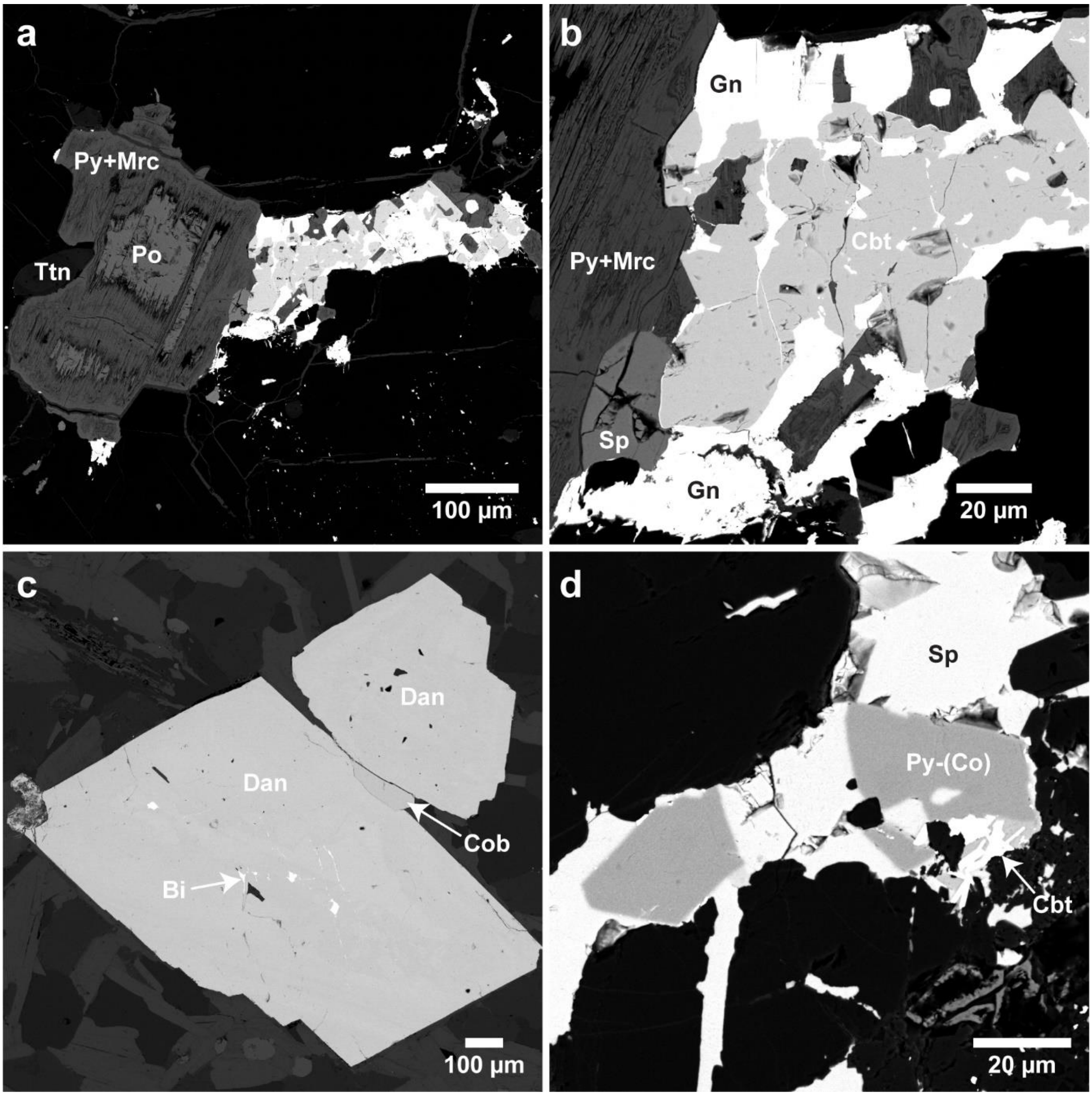

Figure 12. Back-scattered electron images (SEM-BSE). **A**. Pyrrhotite breaks down into pyrite and marcasite on the left-hand side, on the right-hand side costibite (Cbt) occurs intergrown with galena and pyrite (ALZ180089A-2). **B**. Close-up of A, which shows that costibite is partly intergrown with and partly overgrown by galena. Pyrite and sphalerite are also present. **C.** Danaite (Dan) crystal with inclusions or exsolutions of native bismuth (white) and cobaltite along its edges (ALZ180037A). **D.** Cobaltoan pyrite and costibite intergrown with and overgrown by sphalerite (ALZ180089A-2). Photos: Alexander Lewerentz.

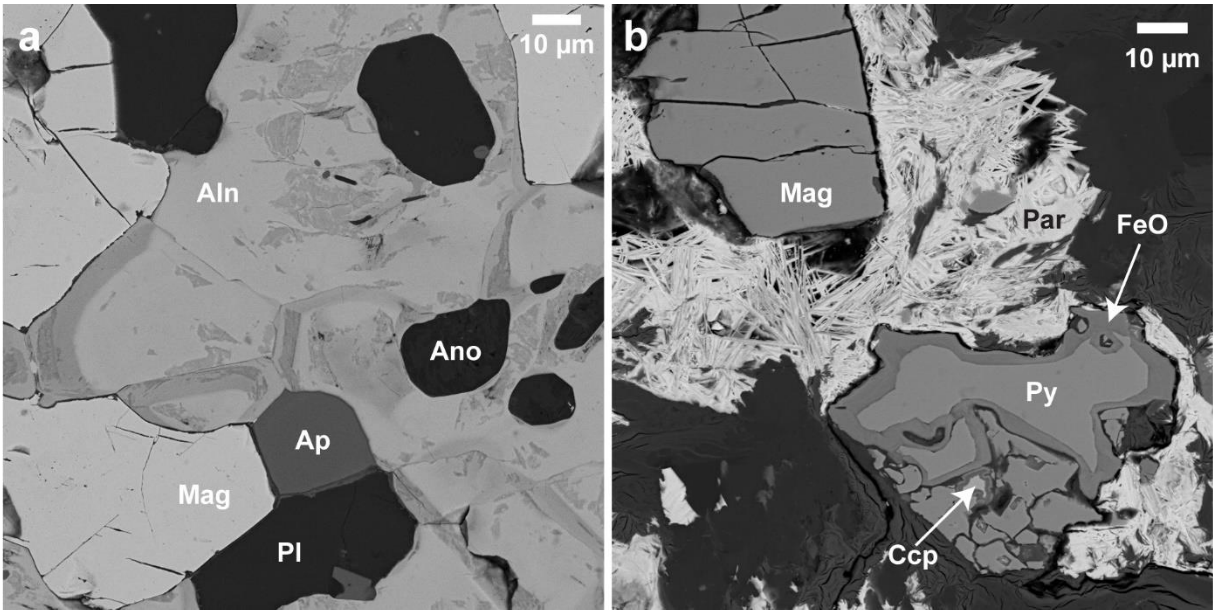

Figure 13. SEM-BSE images from a thin section of a sample from Skuru gruvor (ALZ190037A). **A.** Allanite-(La) that is intergrown with magnetite, plagioclase, and apatite-(F), and hosts inclusions of anorthoclase. Note the irregular zonation within the allanite, where darker grey zones have considerably lower REE content than lighter grey domains. **B.** Undeformed, thin sheets or laths of parisite-(La) (Par) fills an open space between magnetite and pyrite, magnetite on the other hand is clearly deformed (fractured) and pyrite partially replaced by an iron oxide mineral along the rim. Photos: Alexander Lewerentz.

Alteration mineral assemblages

Several minerals commonly occur together with the sulphide mineralisation. The relationship between these minerals and the mineralisation has not been studied in detail, but several observations can be made that are outlined below. In addition, a more detailed description of the alteration is offered by Leopardi (2020). Quartz and biotite are the most common gangue minerals surrounding the mineralisation. They supposedly represent a major component of the original host rock, but inclusions of sulphide minerals also occur inside quartz crystals of rounded quartz aggregates, which indicates that some of the mineralizing fluids were probably silica-saturated. Vice versa, grains of quartz and biotite locally occur as inclusions in sulphide minerals, which suggests partly simultaneous formation or several generations of both sulphides and gangue minerals. Molybdenite appears to have a genetic link with biotite or the pre-metamorphic minerals that biotite formed from, as indicated by generally higher abundance in biotite-rich samples and occurrence as thin laths between biotite cleavage planes.

Ti-bearing minerals like titanite, rutile and ilmenite are more common in mineralised samples and some titanite have inclusions of quartz and sulphide minerals (Leopardi, 2020). Rutile is especially common in the strongly Co-mineralised sample ALZ190034A (6526164/503246), where it occurs mostly together with early pyrite and pyrrhotite and formed before the main cobalt-mineralising event (Fig. 14a). Titanite is part of the calcareous skarn assemblage and apparently formed later, occurring mostly together with sphalerite and galena (Fig. 14b).

Chlorite, mostly in the Fe- and Mg-rich varieties clinochlore and chamosite, occurs sometimes intergrown with sulphide minerals. Chamosite occasionally forms a rim around pyrite and could be a product of the breakdown of pyrite (Fig. 14c). In contrast, clinochlore occurs intergrown with the chalcopyrite and sphalerite mineralisation (Fig. 14d). Another mineral that is associated with this phase of the mineralisation is clinozoisite (Fig. 14e). In addition, the Mg-rich minerals anthophyllite and cordierite occur in the close vicinity of the mineralisations (see also Leopardi 2020). Pyrrhotite, chalcopyrite and danaite locally occurs as inclusions in or intergrown with aggregates of apatite (Fig. 14f). Epidote and amphibole are commonly associated with sulphide mineralisation hosted by amphibolites. Locally, abundant tourmaline appears together with the sulphide mineralisation.

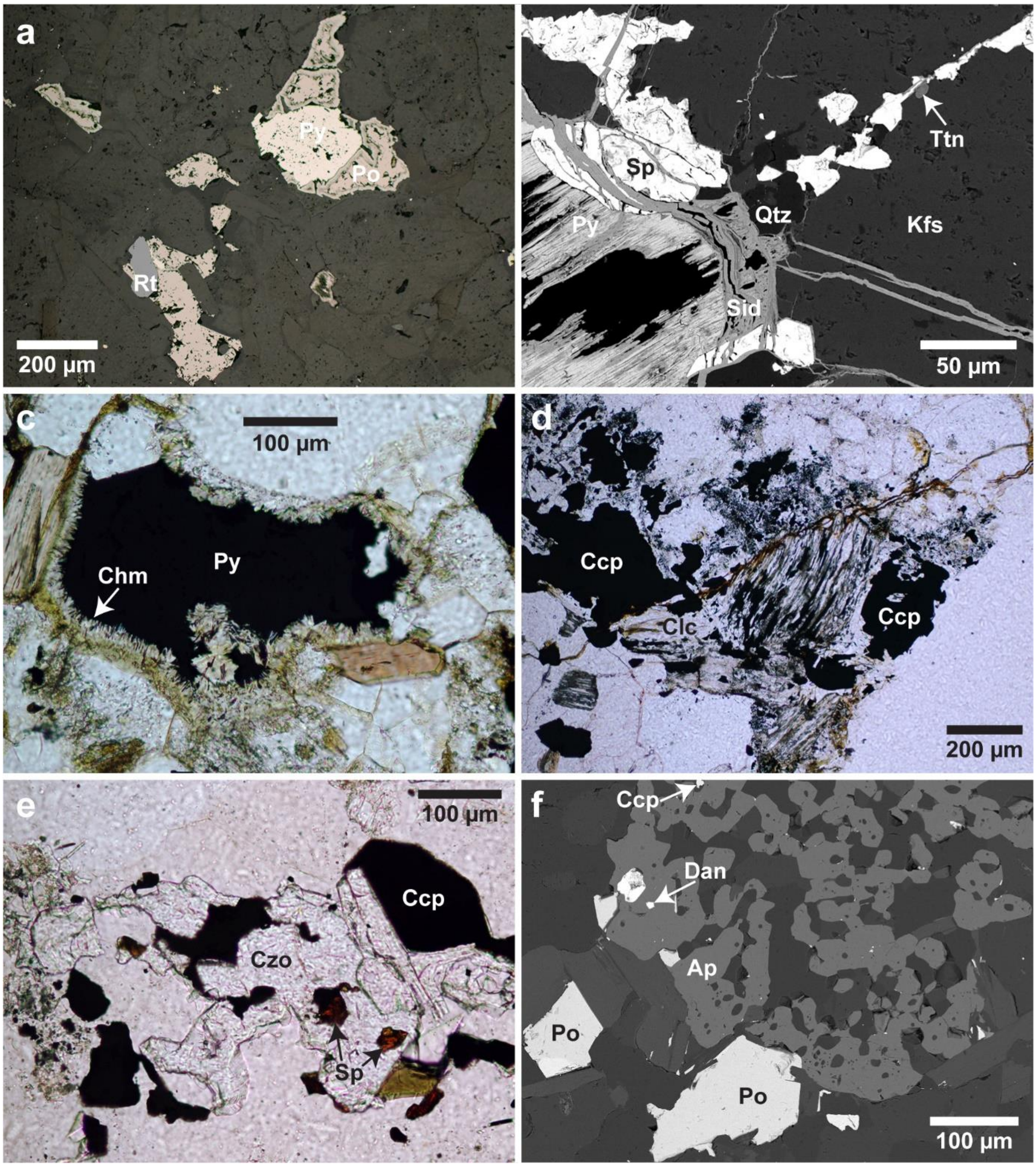

Figure 14. A. Reflected light photomicrograph of rutile intergrown or surrounded by early pyrite and later pyrrhotite (ALZ190034). Photo: Edine Bakker. **B.** SEM-BSE image of early, strongly altered pyrite, overgrown by sphalerite, which occurs together with titanite and late fractures filled with siderite (ALZ180089A-2). Photo: Alexander Lewerentz. **C.** Transmitted light photomicrographs (ppl) of pyrite surrounded by chamosite (ALZ190034), **D.** clinochlore intergrown with chalcopyrite and lesser sphalerite (EDB190035A), as well as **E.** chalcopyrite and sphalerite intergrown with clinozoisite (EDB190035A). Photos: Edine Bakker. **F.** SEM-BSE image of pyrrhotite, chalcopyrite and danaite intergrown with and included in apatite (EDB180034A). Photo: Alexander Lewerentz.

In summary, the early pyrite, pyrrhotite and molybdenite stage of the mineralisation was formed by metal-bearing fluids predominantly rich in Fe, Si, K, and Ti, whereas the later precipitation of chalcopyrite, sphalerite and galena involved fluids rich in Ca, Mg and Ti. Overlap of different alteration styles is common and the different stages are not always clearly distinguishable.

Mineral compositions

Mineral compositions were determined at the Department of Geology, Lund University, Sweden, using a Tescan Mira 3 Field Emission Scanning Electron Microscope equipped with an EDS analyser from Oxford Instruments. The instrument was operated at 15kV with a beam intensity of 17nA. Spectral intensities were standardised by built-in analyses of well-characterised reference material and quantified by optimisation to a Co metal standard. All samples were coated with ~20 nm of C prior to analysis. Analytical error is element-dependent and typically vary from 0.2 to 1.5 wt.% (2σ). The data can therefore be regarded as quantitative for major constituents, semi-quantitative for minor constituents, and qualitative for identification of trace concentrations. Due too technical difficulties some analyses yielded totals that significantly deviate from 100 wt.%, or what is expected for H- or C-bearing mineral species: although these data are non-quantitative, the relative proportions of elements still provide qualitative identification of mineral and end member species.

Andalusite and cordierite were analysed from one of the metavolcanic rocks (Appendix 2a). Andalusite contains up to 1.4 wt.% Fe_2O_3, assumed to substitute for octahedral Al (cf. Faye & Harris 1969). Cordierite has a #Mg of 0.80–0.82.

Amphiboles were analysed from two sulphide-mineralised metavolcanic rocks and one sulphide-mineralised skarn (Appendix 2b). All analysed amphiboles belong to the actinolite-tremolite series and have #Mg = 0.67–0.93 (actinolite < 0.9 < tremolite).

Carbonates were analysed from two calcsilicate rocks: one sulphide mineralised skarn and one iron oxide mineralised skarn (Appendix 2c). In the sulphide mineralised skarn calcite is the only detected carbonate mineral, one analysis with minor $FeCO_3$ and $MnCO_3$ end member components (c. 1%).

Epidote group minerals include allanite-epidote, clinozoisite and epidote (Appendix 2d). Allanite-epidote is the main REE-bearing mineral in the iron oxide mineralised skarn sampled from Skuru gruvor, with up to 24 wt.% total REE_2O_3 (mainly La and Ce). Clinozoisite is present in a sulphide-mineralised metavolcanic rock, whereas a sulphide-mineralised skarn contains both clinozoisite and a 50/50 component of the two end members. Zoisite was also detected in the skarn.

Feldspars from metavolcanic rocks were analysed (including sulphide-mineralised samples), as well as from sulphide- and iron oxide mineralised skarns (Appendix 2e). All analysed K-feldspars have a minor Na-component (4–9% Ab), and in two samples contain up to c. 2 wt.% BaO. Plagioclase is generally more albitic in metavolcanic rocks (59–71% Ab) than in skarns (51–56% Ab), likely related to the higher bulk rock Ca content of skarns. Anorthoclase was identified in an iron oxide mineralised skarn.

Garnet compositions were determined for two samples: one skarn and one metavolcanic rock, both sulphide-mineralised (Appendix 2f). Skarn garnets are highly calcic with 75–80% Grs, 11–18% Adr, 5–7% Alm, and 1–2% Sps. The only analysed metavolcanic garnet had a binary Fe-Mg composition corresponding to 91% Alm and 9%Prp.

Chlorite and mica group minerals were analysed from metavolcanic rocks, sulphide-mineralised metavolcanic rocks, as well as sulphide- and iron oxide mineralised skarns (Appendix 2g).

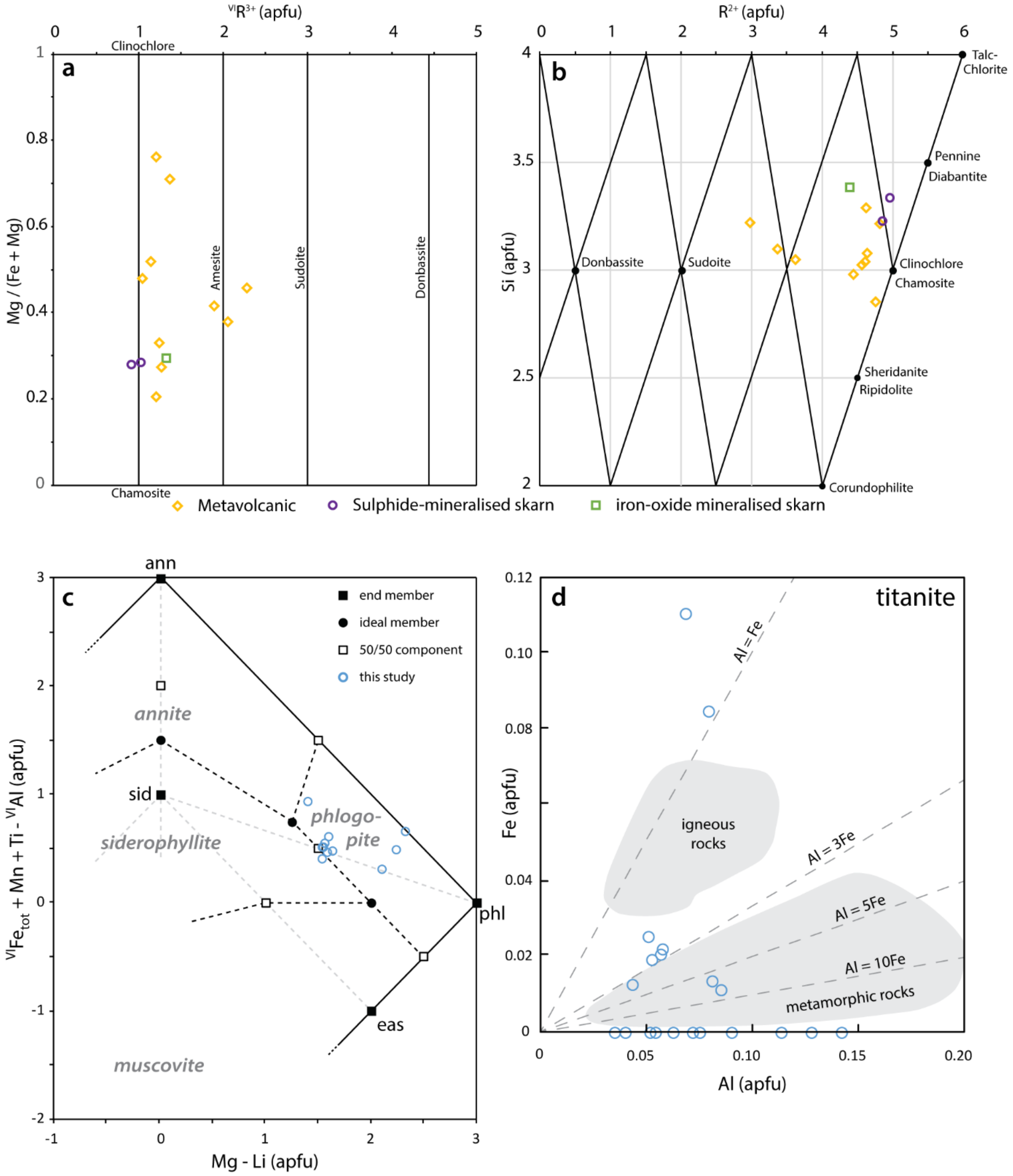

Figure 15. A. Chlorite classification based on the Fe:Mg ratio and the number of octahedrally coordinated atoms per formula unit (after Plissart et al. 2009). **B.** Chlorite classification based on the relationship between number of atoms per formula unit of tetrahedrally coordinated ions vs. Si (after Wiewióra & Weiss 1990). Most analysis are of the chamosite-clinochlore series; however, chlorite from one of the metavolcanic samples would be classified as amesite. **C.** Classification diagram for biotite (redrawn from Tischendorf et al. 2007). All analyses in this study fall within the phlogopite field, although with up to 50% of a siderophyllite component. **D.** Plot of Al vs. Fe content in titanite (after Aleinikoff et al. 2002), most grains are Fe-poor and could thereby be interpreted as of metamorphic origin. Note that analyses plotted as Fe = 0 were below the detection limit but likely have some smaller Fe component.

Chlorite from both skarns and metavolcanic rocks plot on the chamosite-clinochlore mixing line, except for one metavolcanic sample where chlorite formed in association with pyrite and shows a composition corresponding to amesite (Fig. 15a–b). Biotite analyses of unmineralised and sulphide-mineralised metavolcanic rocks all lie within the phlogopite field, but in one sample cluster around the siderophyllite-phlogopite 50/50 mixing component (Fig. 15c).

Clinopyroxenes were analysed from a sulphide-bearing skarn sample (Appendix 2h). Two distinct groups are present: one that represents a 50/50 component of the diopside-hedenbergite series, and one that represents an intermediate diopside composition.

Phosphate and sulphate compositions from metavolcanic rocks and skarns are presented in Appendix 2i). Apatite-(CaF) is present in several samples, trace amounts of Cl were detected in some. Monazite from a sulphide-mineralised metavolcanic rock contains c. 0.48 apfu La, 0.43 apfu Ce and 0.06 apfu Nd. Baryte was detected in one of the sulphide-mineralised metavolcanic rocks.

Titanite was analysed from several samples of sulphide-bearing metavolcanic rocks and skarns (Appendix 2j). Most analyses show very low Fe-contents (Fig. 15d), which can be interpreted as that the titanite is of metamorphic rather than igneous origin (Aleinikoff et al. 2002), or at least recrystallised during metamorphism (Xie et al. 2010). This interpretation fits with the textural observation that titanite is part of the syn-metamorphic skarn assemblage (see *Descriptions of mapped rocks* above). Detailed SEM studies of titanite grains further indicate the occurrence of at least two generations of titanite, as evidenced by that many grains show inherited cores and complex zonation (Leopardi 2020). Two analyses plot above the igneous spectrum (according to Aleinikoff et al. 2002); however, later studies have shown that titanite formed in peralkaline igneous and volcanic systems generally has Fe:Al > 1 (Kowallis et al. 2018).

Zircon was analysed in three samples: one skarn and two metavolcanic rocks, all sulphide-mineralised (Appendix 2k). Two of the analyses show trace amounts of Ca and Fe, which could indicate that these grains were formed or altered by hydrothermal processes (cf. Geisler et al. 2007, Schaltegger 2007).

Analysed ore-forming minerals include arsenopyrite/danaite, bismuthinite, chalcopyrite, cobaltite, galena, hematite, magnetite, native Bi, Ni-cattierite, pyrite, pyrrhotite, rutile, sphalerite and costibite/willyamite (Appendix 2l).

Metamorphism

Prograde and retrograde metamorphic mineral assemblages

The metamorphic grade in the area has previously been estimated to upper amphibolite facies on a regional scale (Skelton et al. 2018). This is largely in line with our field observations of garnet porphyroblasts in granodiorite, and that mafic rocks are extensively recrystallised with porphyroblasts of hornblende (Fig. 16a). However, the occurrences of migmatites, especially within the granodiorites whose melting point should exceed 600 °C (cf. Chen & Grapes 2007), could possibly indicate even higher temperatures).

Under the microscope, garnet porphyroblasts were observed in several metagranodiorite samples, locally up to a few mm in size (Fig. 16b). Garnet was also observed in metavolcanic rocks, although here very fine-grained. Porphyroblasts of orthopyroxene were also observed in a few of the metavolcanics (Fig. 16c–d), these samples are particularly Mg-rich. In two metavolcanic samples, cordierite occurs in a prograde paragenesis with garnet and symplectic intergrowths of biotite and andalusite (Fig. 16e–f). Garnets in the metavolcanic rocks are less than 0.01 mm large and show very low to no spessartine component, which could be interpreted as sudden stabilisation at near-peak conditions rather than continuous prograde crystallisation.

Retrograde reactions include pinitisation of cordierite, chloritization of biotite, amphiboles and epidote, as well as sericitisation of plagioclase, which demonstrate at least one retrograde fluid flow event in the area. Based on chlorite thermometry, many of these reactions took place at c. 200–300 °C, consistent with the occurrence of a combination of m-type and f-type pinitisation in cordierite (cf. Ogiermann 2002). Late-stage, foliation-overprinting veins of quartz, chlorite and carbonates indicate a CO_2-bearing, retrograde-metamorphic fluid.

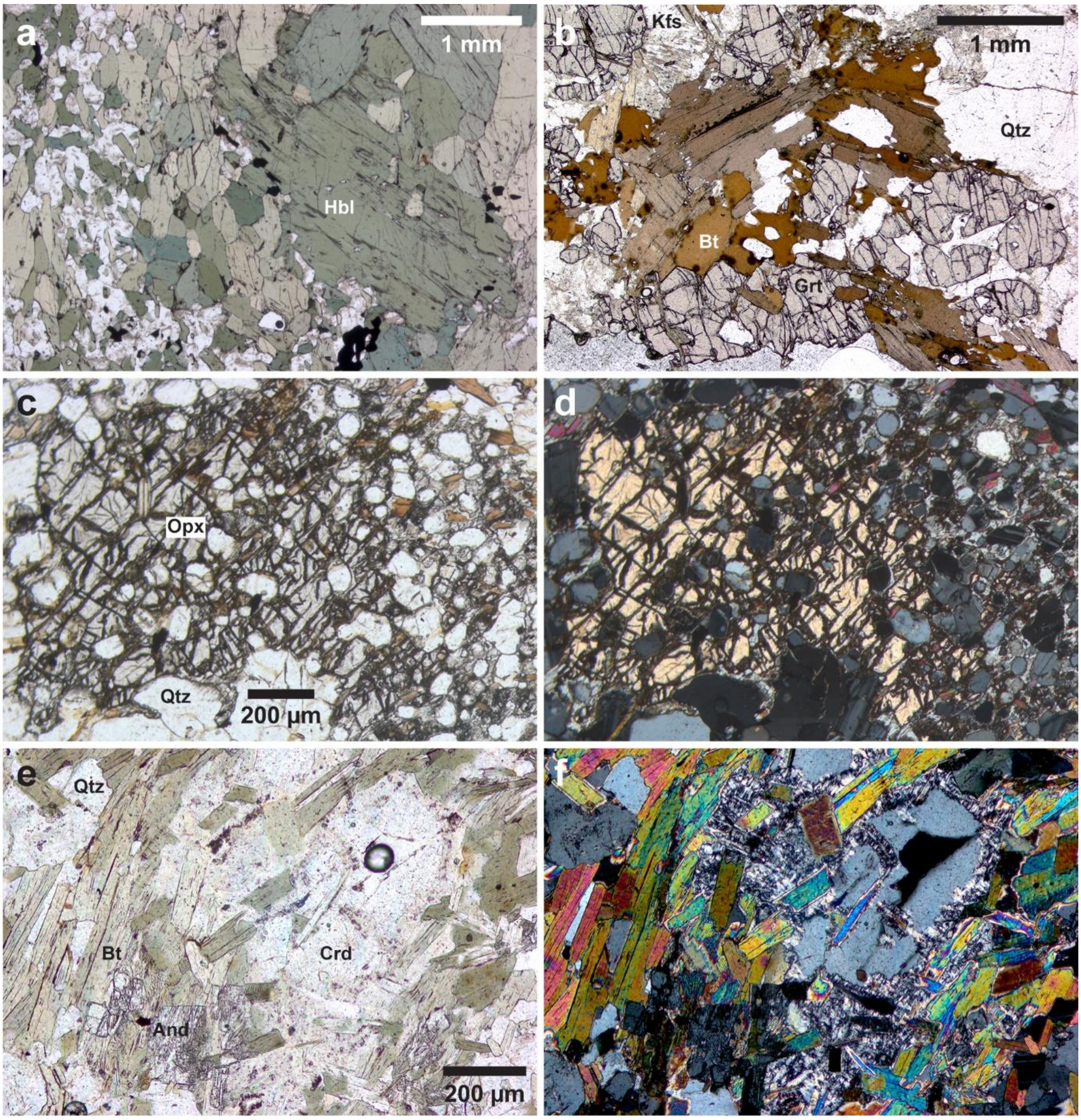

Figure 16. Photomicrographs. **A.** Amphibolite with porphyroblasts of hornblende (ppl; ALZ180033). **B.** Granodiorite with porphyroblasts of garnet, biotite probably also formed, or at least coarsened, during metamorphism (ppl; ALZ180085). **C–D.** Orthopyroxene poikiloblast with inclusions of quartz and biotite (metavolcanic rock; ppl and xpl; ALZ180067). **E–F.** Symplectic intergrowth of biotite and andalusite in a paragenesis with cordierite and garnet (ALZ180076). All photos: Alexander Lewerentz.

Skarns from Vena gruvfält show e.g. garnet and clinopyroxene, minerals that generally are good indicators of metamorphic conditions. Although these minerals most likely were formed during metamorphism, their significance for facies interpretations should be regarded with great caution; the often rather extreme bulk rock composition of skarns may stabilise minerals at P-T conditions impossible in most major crust-forming rock types. The composition of titanite within the skarn assemblages gives further indications towards a formation related to regional metamorphism.

Pressure-temperature estimations

Pseudosections are diagrams that show what mineral assemblages are stable at different P-T conditions, under the assumption of phase equilibria. These are constructed for sample-specific bulk compositions and thereby considers the compositional effect on mineral stabilities. The pseudosections below were constructed in the MnNCKFMASH (MnO-Na$_2$O-CaO-K$_2$O-FeO-MgO-Al$_2$O$_3$-SiO$_2$-H$_2$O) system using Perple_X 6.8.8 (Connolly 2009) and the ds622 internally consistent thermodynamic dataset (Holland & Powell 2011), with the assumption of a saturated unimodal H$_2$O fluid. Activity-composition solution models were used for white micas (White et al. 2014), biotite (Powell & Holland 1999), chlorite (Holland et al. 1998), garnet (White et al. 2014), ternary feldspar (Holland & Powell 2003), staurolite (Holland & Powell 1998), cordierite (White et al. 2014), and orthopyroxene (Holland & Powell 1996), all other phases were treated as pure end members.

For one of the metavolcanic samples (ALZ180076A), the metamorphic paragenesis of biotite+garnet+cordierite+andalusite (Fig. 16e) is structurally interpreted as syn-tectonic and may thereby be used as an indicator of metamorphic conditions (Fig. 17). Compositional isopleths for cordierite ($0.80 \leq X_{Mg} \leq 0.82$) further constrain the P-T range to 1.3–3.5 kbar and 517–612 °C.

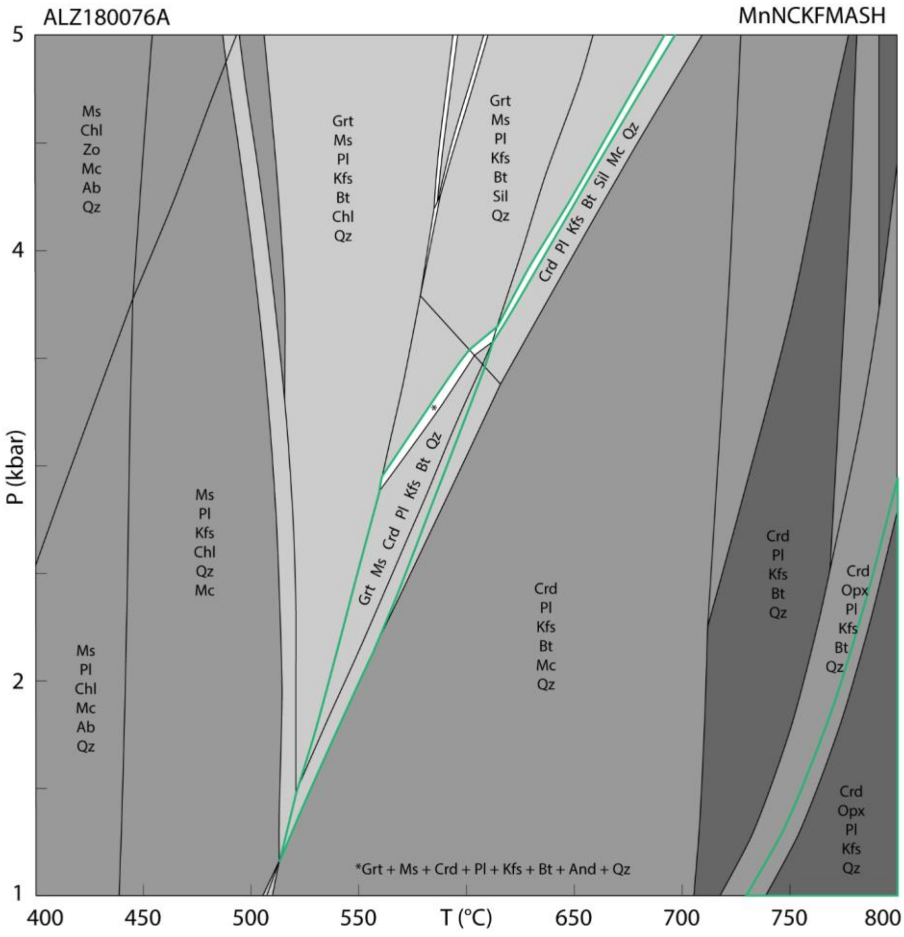

Figure 17. Pseudosection in the MnNCKFMASH system for a cordierite- and andalusite-bearing metavolcanic rock (ALZ180076A), water in excess. Green lines encompass conditions under which cordierite (X_{Mg} = 0.80–0.82) is stable, including the observed prograde assemblage of Bt+Grt+And.

The fact that sillimanite occurs in several samples demonstrates that peak-metamorphic conditions must have exceeded the andalusite stability field, which indicates that the estimate above represent prograde pre-peak metamorphic conditions and that the peak-metamorphic temperature likely was slightly higher. Due to that mineral equilibria were very difficult to interpret for the sillimanite-bearing assemblages, further P-T estimations were not attempted for the sillimanite-bearing samples. In addition, P-T estimates based merely on the occurrence of Al_2O_3 polymorphs are less precise than those based on assemblages including e.g. biotite and cordierite, which is because compositional isopleths cannot be drawn in P-T-x space as Al_2O_3 polymorphs do not change their compositions as a function of P or T. A slightly higher peak temperature would also be in line with the observation of enstatite porphyroblasts in some of the metavolcanic rocks.

Geophysical survey activities

Airborne measurements

During the 1980 airborne geophysical campaign, the geomagnetic field (5 nT precision), natural gamma radiation and electromagnetic field (single frequency VLF) were measured and sampled at an interval of c. 40 m with a nominal altitude of 30 m and line separation of 200 m. A major disadvantage with the airborne data acquired in 1980 is that the VLF-signal was recorded from only one transmitter, which makes the measurements directionally dependent. Resistive structures with an orientation towards the transmitter can be well resolved, whereas perpendicularly oriented structures will be poorly resolved. Moreover, the best results in airborne measurements are achieved if flight lines are perpendicular to the strike of the structures of interest. In the 1980 survey, flight lines were oriented in north-south direction, which is not optimal in the Vena area where the main structures are oriented in the northwest-southeast direction.

As part of a larger airborne campaign by SGU between May and June 2018, new magnetic, electromagnetic and radiometric data were acquired in the Vena area. This acquisition was flown perpendicular to the strike of the main features in the Vena area at 60 m nominal altitude and 200 m line separation with a sampling interval of c. 7 m. The current acquisition system uses a Scintrex CS-2 magnetometer with <0.3 nT precision, a Radiation Solutions RSX-5 spectrometer and an SGU-built dual-frequency VLF-instrument. Aside from significant improvements in sampling interval and measurement precision, the VLF signal from two transmitters allows the calculation of directionally independent maps of apparent resistivity and current density. These new data are thus much more suitable for geophysical interpretation and modelling in the area.

Aeromagnetics

The Vena gruvfält area is characterised by the pattern of strong magnetic anomalies in the NW–SE direction that reflect the lithological variation and deformation (Fig. 18). Variation in magnetic intensity is linked to the magnetisation in the rock and distinct positive anomalies are often related to iron-rich mineralisations. The dominant magnetic anomaly coincides with volcanic hosted iron-oxide mineralisations. All historical magnetite ore mines, from the Skuru gruvor area in the north to the Lövfallafältet area southeast of Vena gruvfält, follow this anomaly. A slightly weaker positive anomaly is located c. 500 m to the southwest of the main magnetic anomaly but runs parallel with it. This anomaly coincides with the sulphide-bearing volcanic rocks within Vena gruvfält, which owes its magnetic response to pyrrhotite (Fig. 18).

Airborne measurements of magnetic, VLF and spectrometry data, as well as ground-based magnetic, VLF and gravity data, were processed using Geosoft Oasis Montaj. Spectrometry measurements on the ground were processed with Georadis RS Analyst and petrophysical data were analysed with Microsoft Excel. All data are stored in the respective SGU databases for petrophysical and geophysical data.

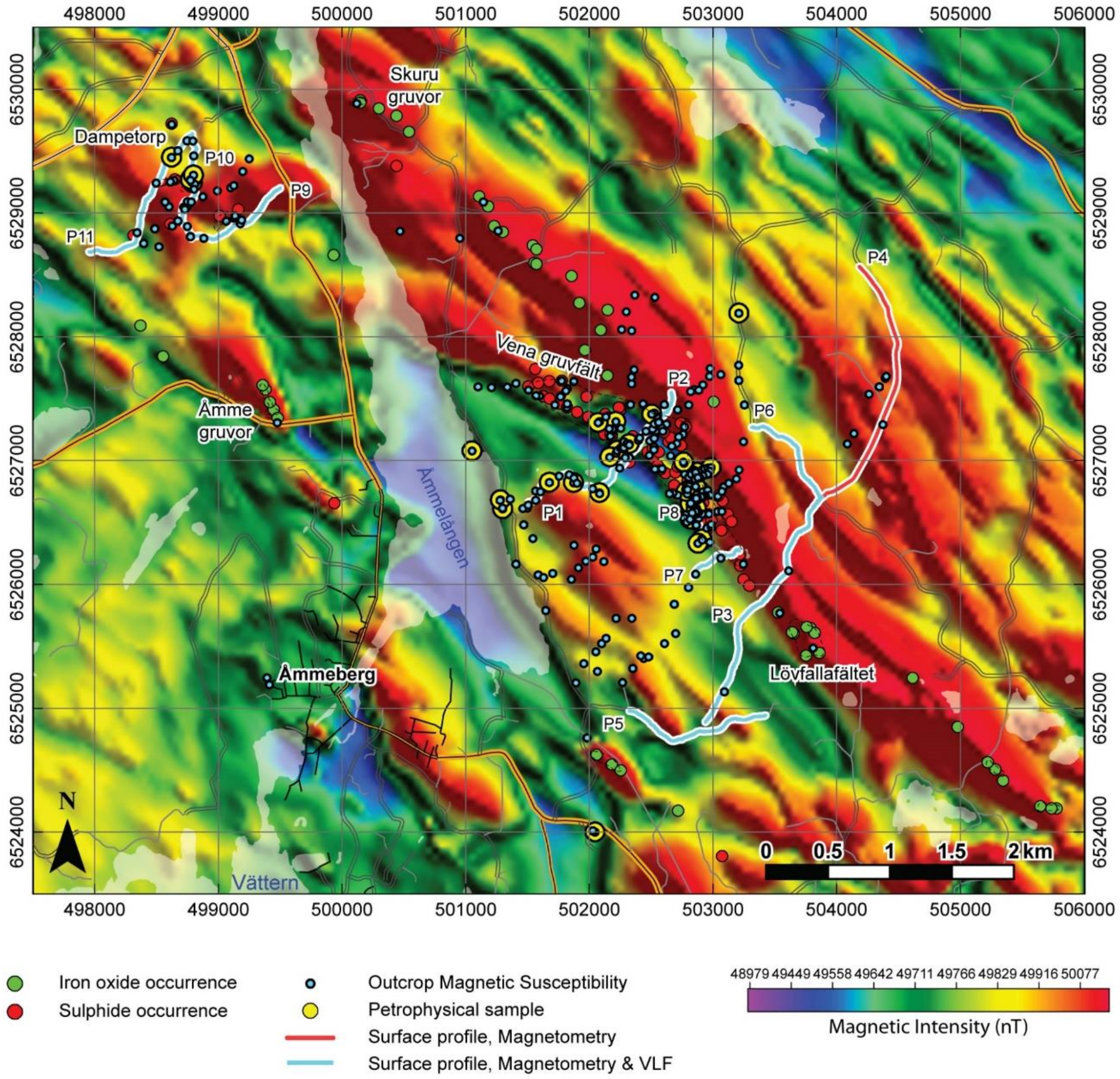

Figure 18. Total magnetic intensity based on aeromagnetic measurements in 2018, generated by reduction of the total magnetic field intensity to the geomagnetic pole. Positive anomalies (red colours) typically indicate the presence of ferro- and ferrimagnetic minerals among which magnetite and pyrrhotite are known in the mineralised areas. Airborne and surface magnetic measurements along profile 1 and 2 (black line) are shown in Figure 21.

Airborne VLF

The VLF method measures the electromagnetic field in the VLF frequency range (15–30 kHz), and maps perturbations caused by interaction with electrically conductive material at the surface or shallow depths. Well-preserved felsic to intermediate plutonic rocks are typically highly resistive (low electrical conductivity), whereas mineralised zones and water-conducting faults and fracture zones have high electrical conductivity and give rise to negative resistivity anomalies (high electrical conductivity). The method is sensitive to contamination by infrastructure and sources of noise must be eliminated before interpretation. The VLF data were processed to generate maps of apparent resistivity and current density, where the latter is presented in Figure 19. Strong anomalies in current density are seen to coincide with the strong magnetic anomalies in the Vena gruvfält area. This likely reflects a locally enhanced electrical conductivity caused by the sulphide mineralisation in the Vena mining district and the iron-oxide mineralisation along the dominant magnetic anomaly directly to the north and northeast of Vena.

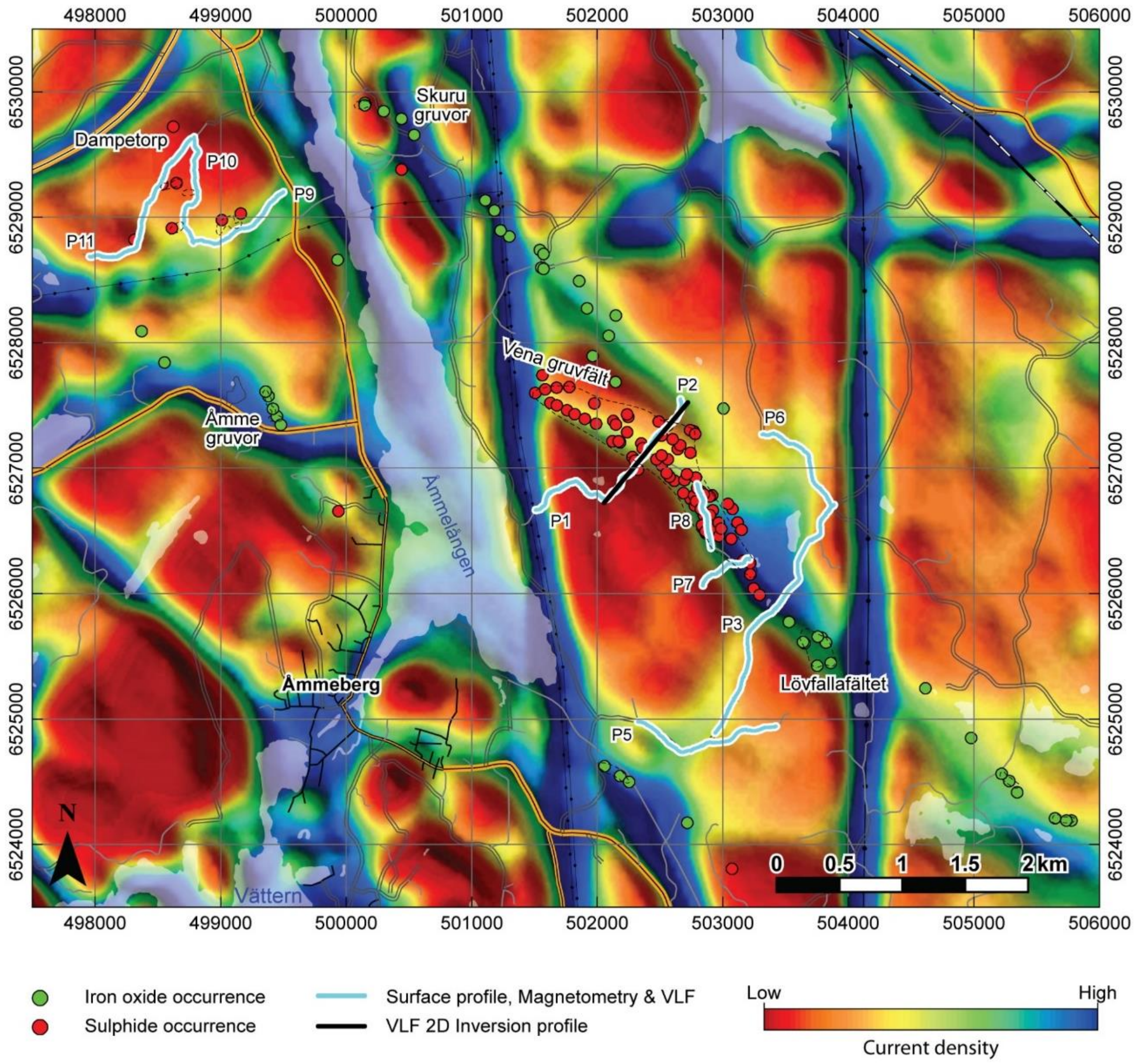

Figure 19. Current density calculated from airborne VLF measurements acquired in 2018. Positive current density anomalies (blue colours) represent areas of high electrical conductivity, possibly caused by mineralised zones or water-conducting faults and fracture systems but may also result from contamination by infrastructure such as powerlines and railroads. The positive anomalies connecting the Skuru, Vena and Lövfalla mining areas coincide with the magnetic anomalies and likely reflect the geographical distribution of the known mineralisation. Results from 2D inversion of surface-based VLF-measurements along profile 1 and 2 (black line) is shown in Figure 21.

Gravity

Gravity data acquired prior to this project have relatively sparse sampling in the area, averaging c. 1–2 km between measurements locations. In May and September 2019, SGU collected a total of 320 new gravity measurements within Vena gruvfält and the surrounding area to complement existing data. In addition to achieving a denser coverage of measurement locations in the area, with an even distribution and an average separation of c. 1 km, profiles were acquired in and across the Vena ore field with a point separation of c. 200 m.

The instrument used for the gravity measurements was a Scintrex CG-5 and elevation determination was done using GNSS-equipment from Topcon. The map in Figure 20 shows the residual gravity anomaly, calculated as the difference between the terrain corrected Bouguer anomaly and a 3 km upward continuation of the same.

In general, mafic bedrock formations or major mineralised zones have relatively high densities and give rise to positive gravity anomalies, whereas felsic bedrock in contrast have lower densities and generate negative gravity anomalies. The gravity point separation is not dense enough to resolve near-surface formations but the major positive gravity anomaly, extended in the northwest-southeast and parallel with the magnetic anomaly on its southwestern side, gives evidence for a larger density surplus at depth below lake Åmmelången. It is worth noting that nearly all sulphide mineralisations from Dampetorp in the north, through the Vena area and down to Zinkgruvan, all fall along the northeastern and eastern side of this anomaly.

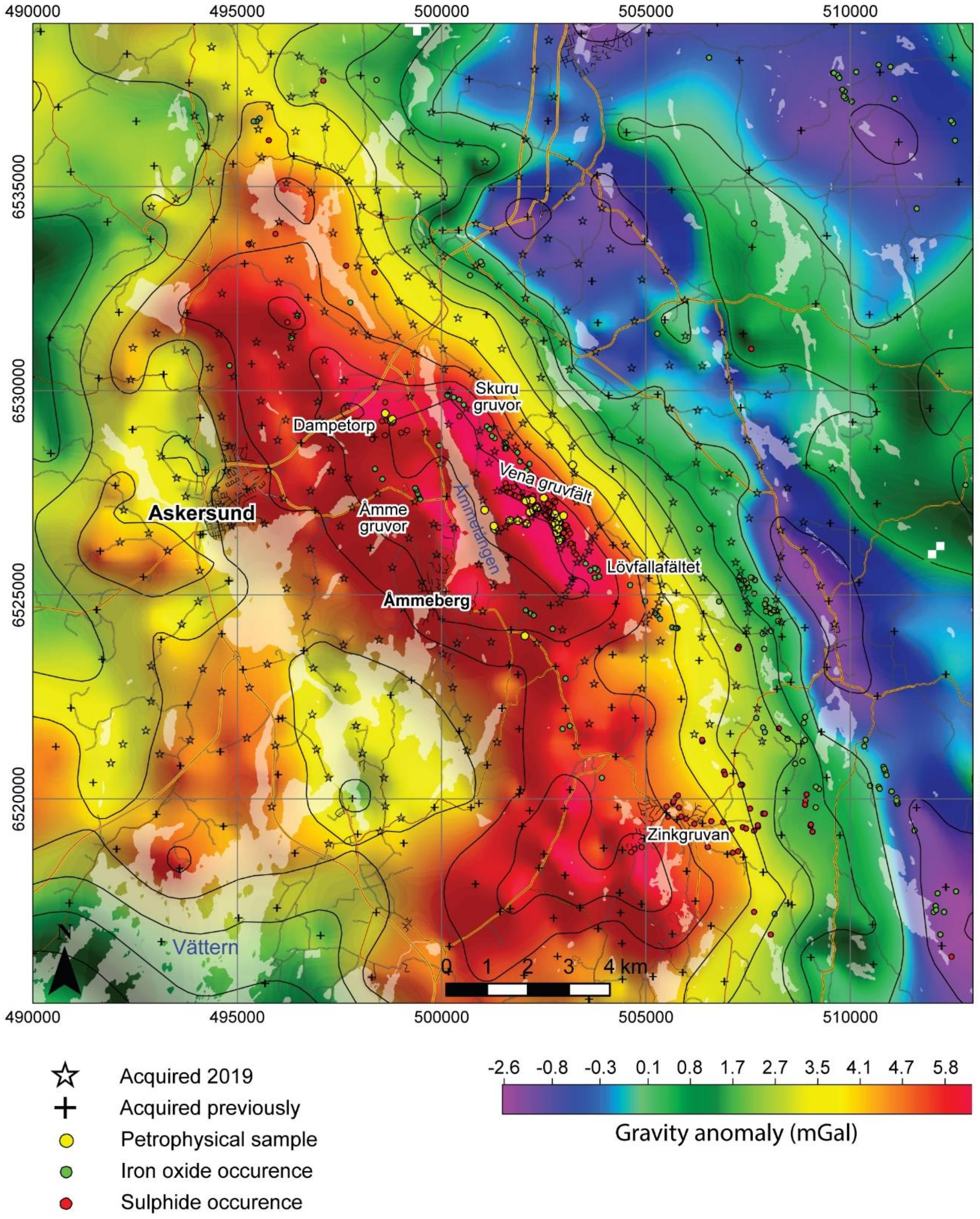

Figure 20. Residual gravity anomaly map based on gravity data acquired in 2019 and previous work, calculated as the difference between the Bouguer anomaly and a 3 km upward continuation of the same. Contour lines represent isolines in the residual gravity anomaly drawn at 0.5 mGal interval. In general, mafic bedrock formations or major mineralised zones give rise to positive gravity anomalies, whereas felsic rock generates negative gravity anomalies. Most of the known sulphide mineralisations in the area (red markers) appear as a chain following the northern and eastern side of the dominant gravity anomaly in the area, which possibly indicates a regional correlation between the mineralisations.

Surface profiling

During May 2019, high resolution measurements of the geomagnetic field and the electromagnetic field in the VLF-range were done on the ground along eight profiles within Vena gruvfält and three in the Dampetorp area (locations shown in fig. 18 and 19). The equipment used was the GEM Systems GSMV-19 combined magnetometer and triple-frequency VLF-sensor with GPS-positioning.

The results from 2D inversion of data along profiles 1 and 2, which overlap and have been merged during processing, are shown in Figure 21. The profile crosses the central part of Vena gruvfält, within proximity to several of the historical mines. The northeastern part of the profile

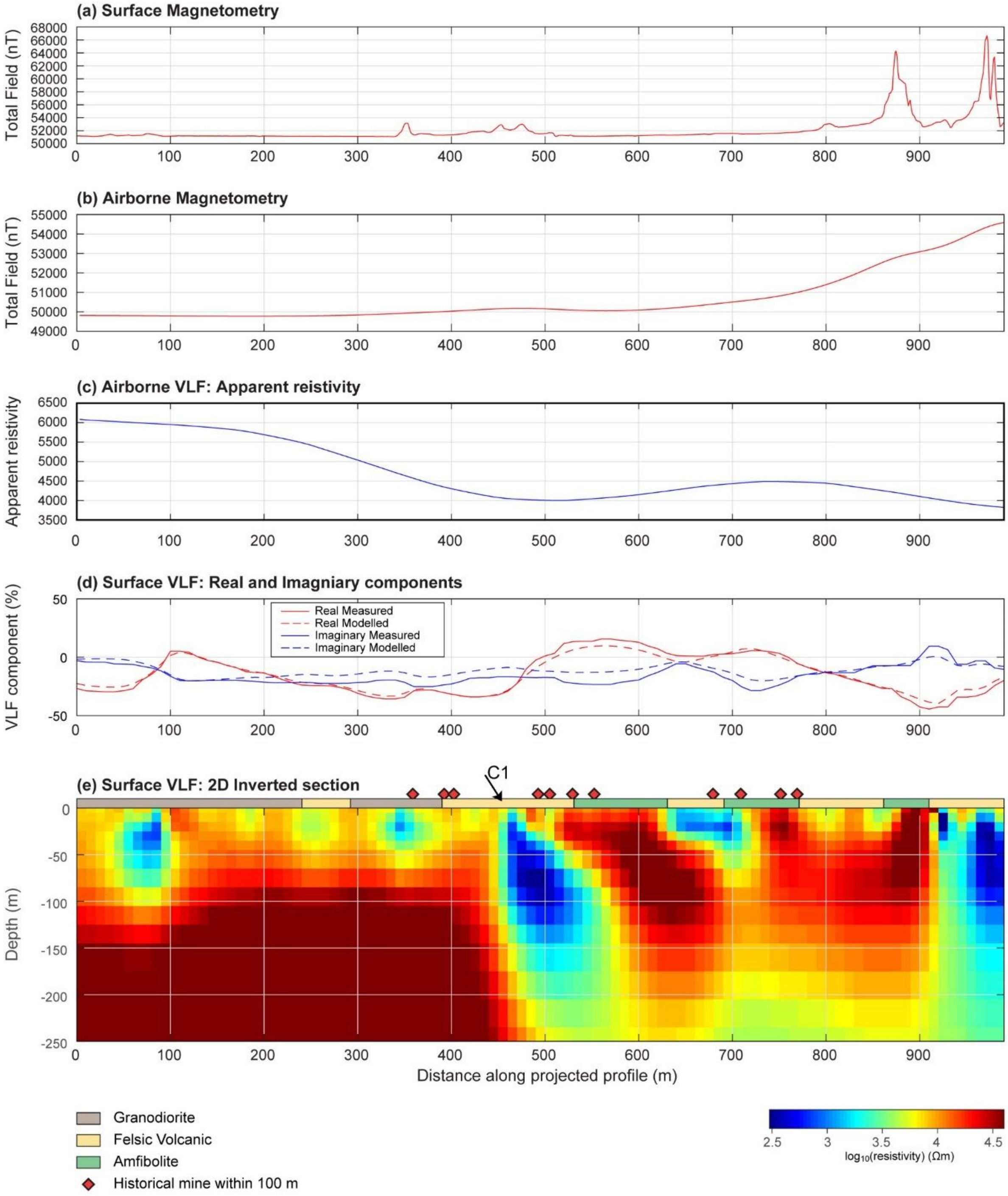

◀ **Figure 21.** Geophysical results along profile 1 and 2 which crosses Vena gruvfält. **A.** and **B.** show the geomagnetic field intensity from surface and airborne measurements, respectively. **C.** Apparent resistivity calculated from airborne VLF-data. **D.** Real and imaginary components from the surface VLF measurements, modelled response from 2D inversion is shown for comparison. **E.** Electrical resistivity at depth from 2D inverse modelling of the surface VLF-data, where negative resistivity anomalies (blue colours) indicate good electrical conductivity in the subsurface. The coloured strip at the top of the section represent the bedrock geology at the surface along the profile (based on the bedrock geology map in Fig. 2). Historical sulphide mines (red diamonds) within 100 m distance from the profiles have been projected to the section and marked at its surface. Most of these are situated in a synformal fold structure. A good conductor (C1) in the western side of the synform coincides with a positive magnetic anomaly and may indicate sulphide mineralisation extending to a depth of at least 100 m.

suggests that Vena gruvfält is situated in a synformal fold structure. Conductive response in this structure is correlated with sulphide hosting volcanic rocks on the surface, while the apparent resistive layer in the synform correlates with mapped amphibolite. The rock hosting the magnetite mineralisation and cause the main magnetic anomaly that is at the end of the profile.

A strong northeast-dipping conductor (C1 in Fig. 21) is situated at the southwestern limb of this synform and extends to at least 100 m depth. This correlates with the positive magnetic anomaly, which indicates that the conductivity is related to the iron-rich sulphide mineralisation. Southwest of this conductor, in the first c. 400 m of the profile, the bedrock primarily comprise granodiorite that typically is resistive.

Petrophysics

During the field campaigns of 2018 and 2019, magnetic susceptibility was measured at a total of 279 outcrops and 40 bedrock samples were collected for petrophysical analysis of primarily density and magnetic properties. A handheld GPS was used for positioning of the samples and measurements. Petrophysical measurements and analysis were conducted at SGU and results are visualised in Figures 22 and 23 and presented in detail in Appendix 5. Petrophysical data assist in the differentiation of rock types, as well as allow for correlation between geophysical measurements and geological parameters.

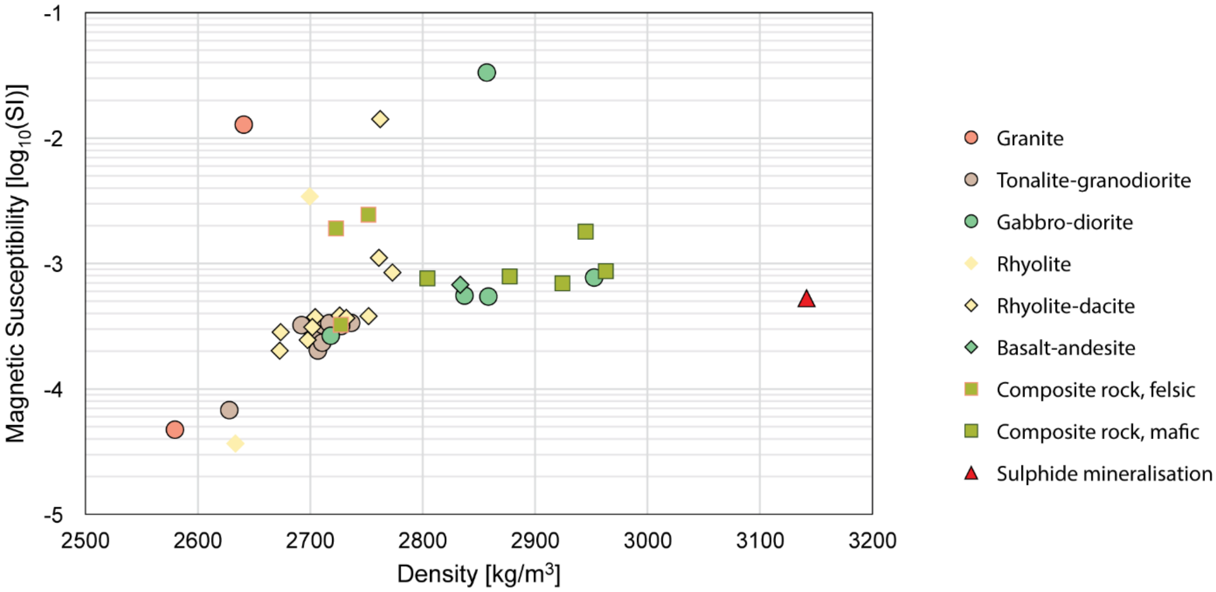

Figure 22. Distribution of density versus magnetic susceptibility of measured samples from the Vena and Dampetorp areas.

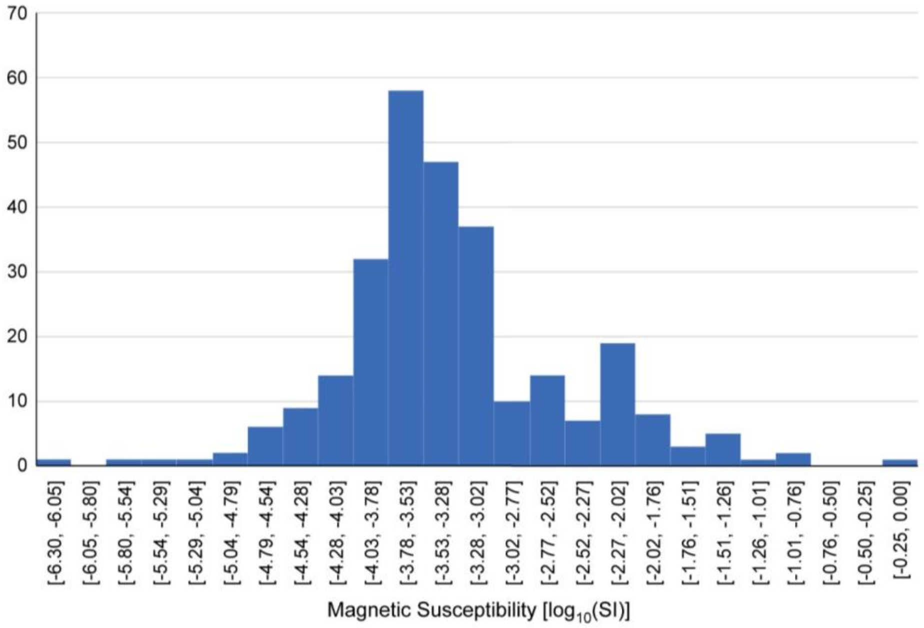

Figure 23. Distribution of magnetic susceptibility from 279 outcrop measurements in the Vena and Dampetorp area.

Spectrometry

Gamma radiation measurements give information about the concentrations of uranium, thorium and potassium in the uppermost few decimetres below the ground surface. Ground measurements are made directly on exposed rock surfaces, whereas airborne spectrometry measurements are to a greater extent influenced by vegetation and quaternary deposits. The relative abundance of uranium, thorium and potassium from airborne measurements is presented in the ternary map in Figure 24 and the spatial distribution of each of the three isotopes is shown in Figures 25–27. In general, the concentrations of these isotopes appear low in the area but the boundary is seen between the younger Askersund granite in the west, with slightly higher potassium concentration, and the older intrusive and volcanic rocks in the east.

A small positive potassium anomaly is seen in the airborne data over Vena gruvfält. It coincides with an open area of large mining waste piles, several hundred metres in diameter. Gamma radiation measurements on outcrops at this location do not show elevated potassium concentrations. Therefore, the airborne data anomaly likely records the contrast in exposure between the open waste piles and the surrounding vegetation- and till-covered bedrock.

Ground spectrometry measurements were made on outcrops at a total of 12 locations in the Vena and Dampetorp areas (see Appendix 7**)**, the results of which generally show low concentrations. Intermediate intrusive rocks have potassium concentrations of c. 3–4%, uranium concentrations of c. 3–6 ppm and thorium concentrations of c. 14–20 ppm. In the Vena area, volcanic rocks have potassium concentrations of c. 2–4%, uranium concentrations of c. 3.5–4.5 ppm and thorium concentrations of c. 10–14 ppm. Volcanic rocks outcropping in Dampetorp have slightly higher potassium concentrations of c. 5.5–6.5% and lower uranium concentrations of c. 2 ppm. It is noteworthy that migmatisation is much stronger in the Dampetorp area (see *Descriptions of mapped rocks* above). The composite mafic-felsic rock has potassium concentrations of c. 1.5–3%, uranium concentrations of c. 3.5–8 ppm and thorium concentrations of c. 10–18 ppm. The span in concentrations for the composite mafic-felsic rock may be due the difference between the mafic and felsic parts which occur in varying amount and degree of mixing. These results are generally in line with the K, U and Th concentrations measured by whole-rock chemical analysis (see *Lithogeochemistry* below).

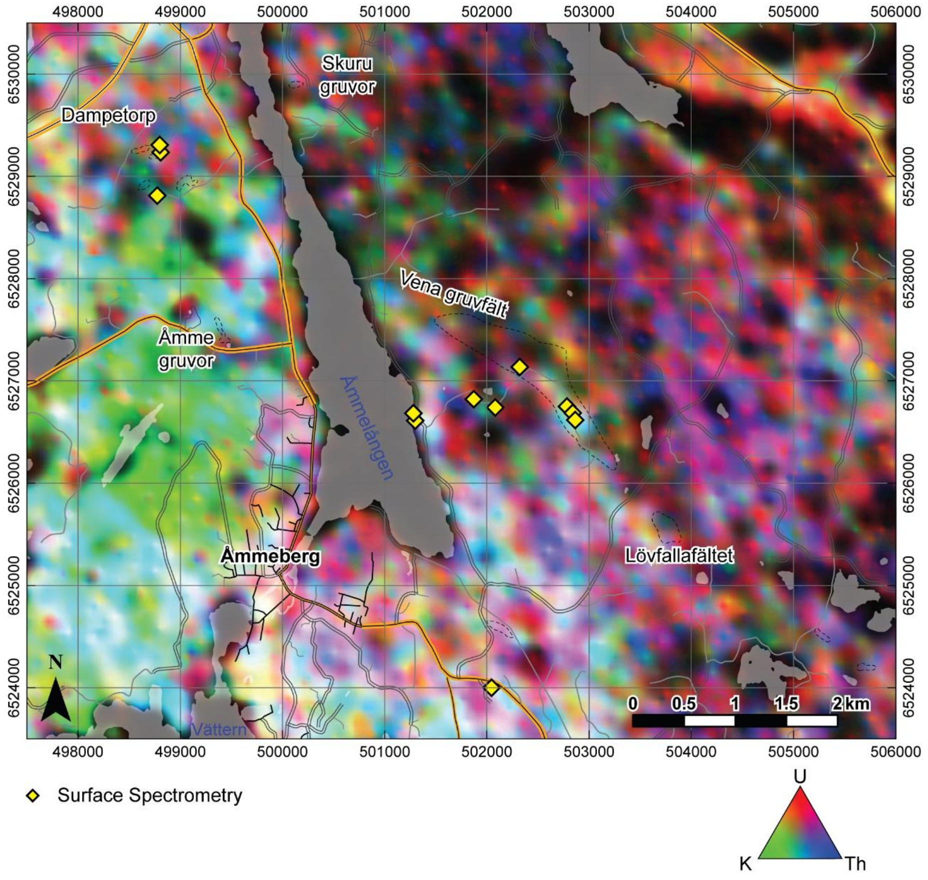

Figure 24. Results from the airborne spectrometry measurements by SGU in 2018. Ternary map showing the relative abundance of uranium, thorium and potassium.

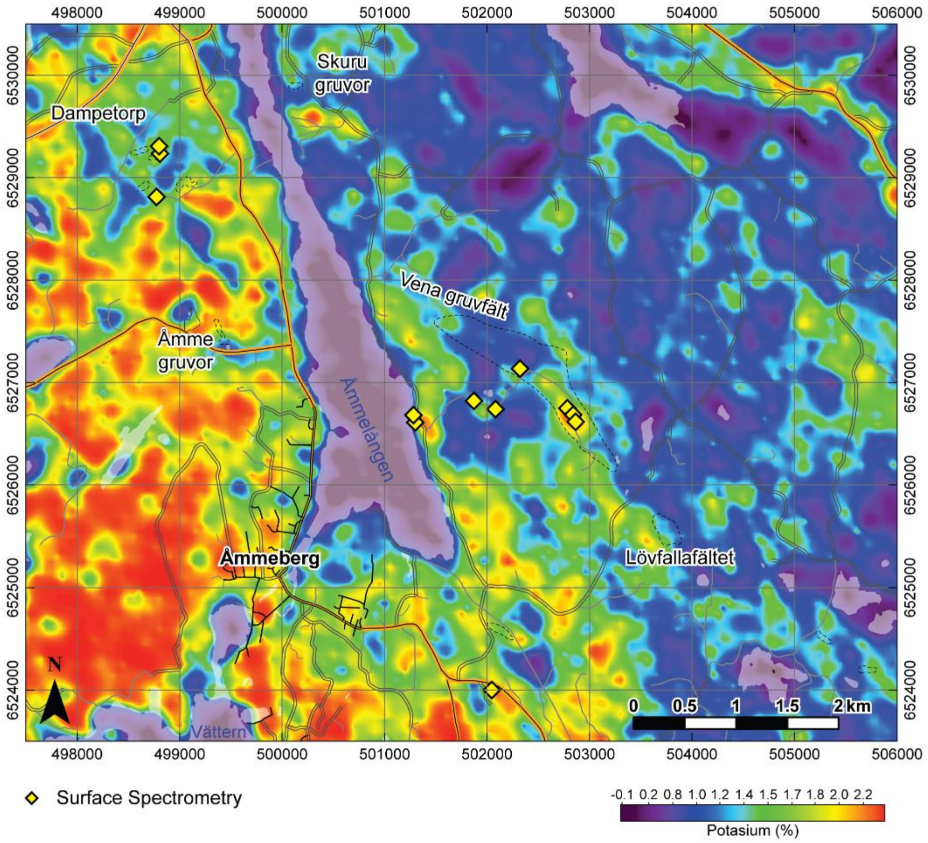

Figure 25. Potassium concentration based on results from airborne spectrometry measurements by SGU in 2018.

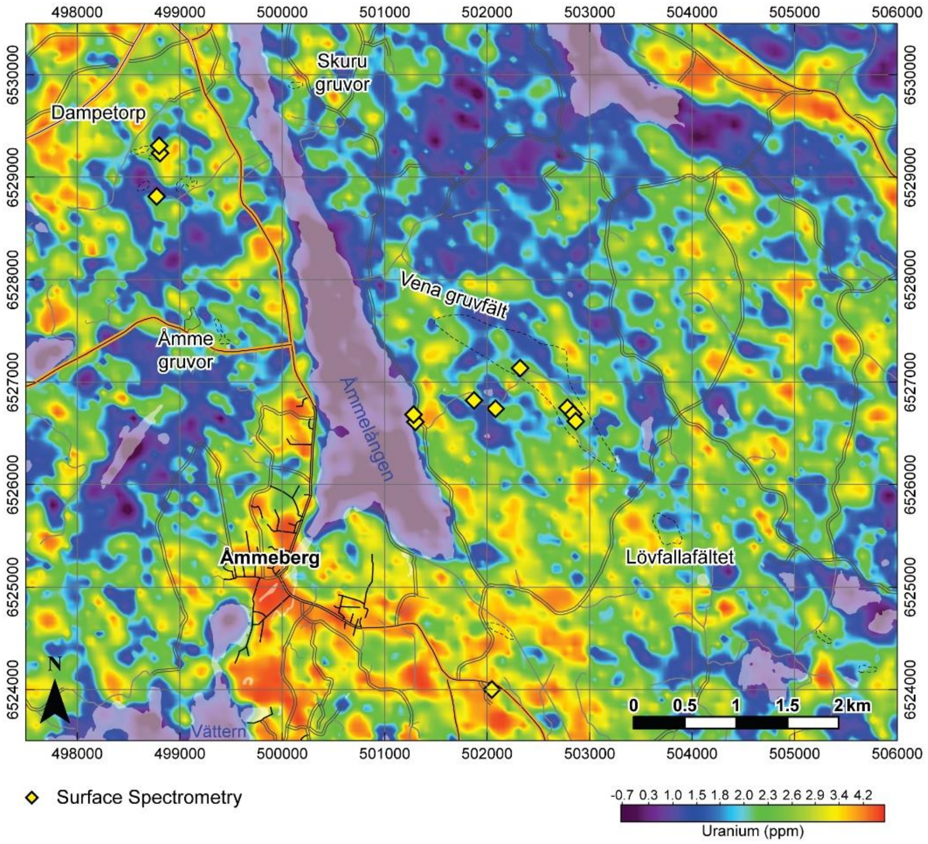

Figure 26. Uranium concentration based on results from airborne spectrometry measurements by SGU in 2018.

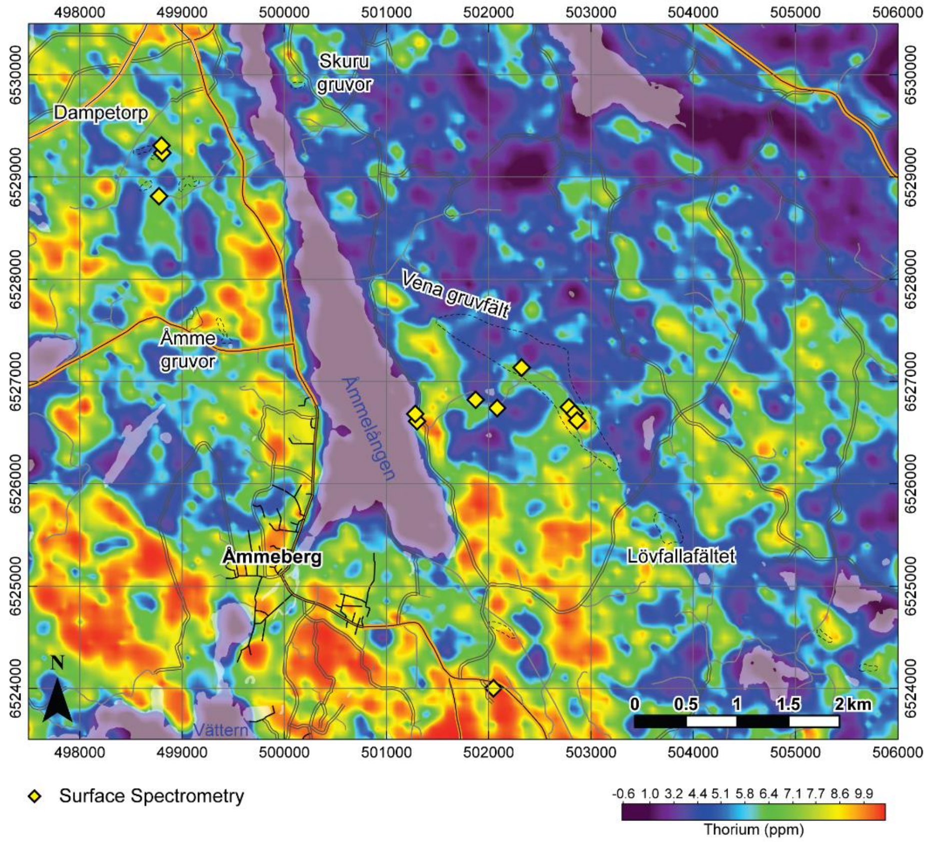

Figure 27. Thorium concentration based on results from airborne spectrometry measurements by SGU in 2018.

Geophysical models in 3D

Aeromagnetic data and surface gravity data were inverted independently, and constrained by petrophysical results, using the VOXI 3D inversion extension in Geosoft Oasis Montaj to produce smooth models of the subsurface distribution of density and magnetic susceptibility, respectively. Figure 28 shows an integrated 3D perspective view where iso-surfaces that encompass areas of high density (blue) and magnetic susceptibility (red) are visualised together with the results from 2D resistivity inversion along profile 1 and 2 (described in Fig. 21). This integrated subsurface model possibly indicates a link between a density surplus at depth (probably a mafic intrusion) and the near-surface synformal structure, which has strongly magnetic, iron-oxide rich mineralisations in its northeastern limb and electrically conductive sulphide mineralisation in its southwestern limb.

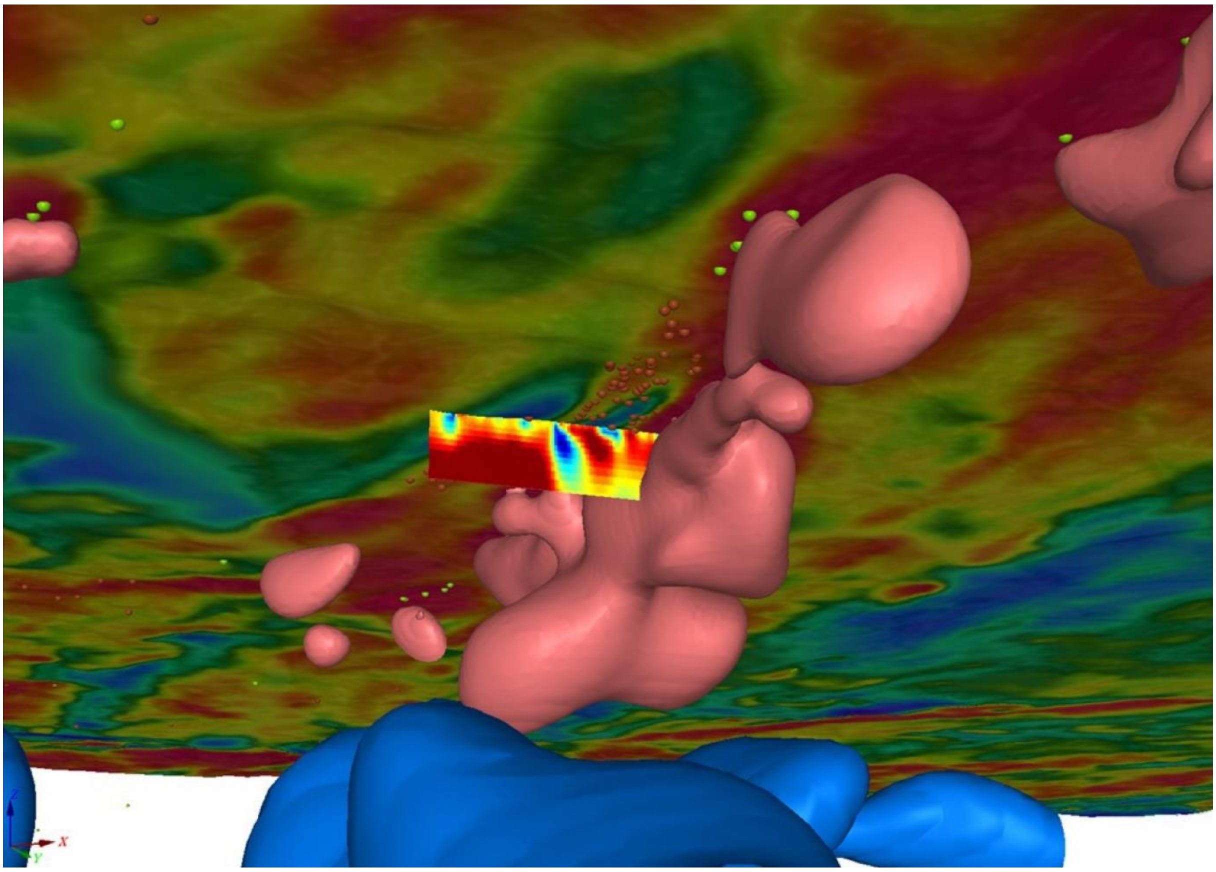

Figure 28. Integrated model of geophysical data. View from a location at approximately 2 km depth below the surface, looking towards northwest Blue surfaces encompass volumes with higher density than surrounding rock, red surfaces encompass volume of higher magnetic susceptibility, based on 3D inversion of surface gravity and aeromagnetic data, respectively. The vertical section shows the variation in electrical conductivity down to a depth of c. 250 m, from 2D inversion of VLF-data along profiles 1 and 2 (see Fig. 21). The topographic surface, seen from below, is draped with the aeromagnetic map (see Fig. 18) and the red and green dots show the location of known sulphide and iron-oxide mines, respectively.

Combined geological-geophysical 3D model

A lithological model was constructed for Vena gruvfält using the 3D modelling software Leapfrog (Fig. 29), which is available via SGU's online 3D viewer. This 3D model is based on our own geological, structural and geophysical surface observations and measurements and interpretations of these, our own and previously documented observations from drill cores (Henriques 1957, 1979, Åberg 1987, Simeonov 1990, Wasström 1991a, 1991b, 1991c), inverse modelling of aerogeophysical data (see above), as well as previous and historic maps and other documentation (Henriques 1964, Åberg 1988).

The Cu-Co-bearing sulphide mineralisation may continue towards depths of at least 500 m (Fig. 30); however, it should be noted that the continuousness of the mineralisation is exaggerated in the model for visual purposes, in reality the mineralisation likely alternately pinches out and reappears along both strike and dip. It should also be noted that the borehole density is low and that all but four bore holes only have an apparent depth of c. 100 m, therefore both vertical and horizontal error is large and this 3D model should be viewed with the prerequisite that it only represents one of many possible iterations of the rock volume. The iron-oxide mineralisation was within the model extents neither mapped in drill core nor on the surface, it is therefore solely drawn from the magnetic susceptibility model using a surface that encompass volumes with magnetic susceptibility > 0.25 SI, which likely implies that the size of the mineralised body is substantially exaggerated.

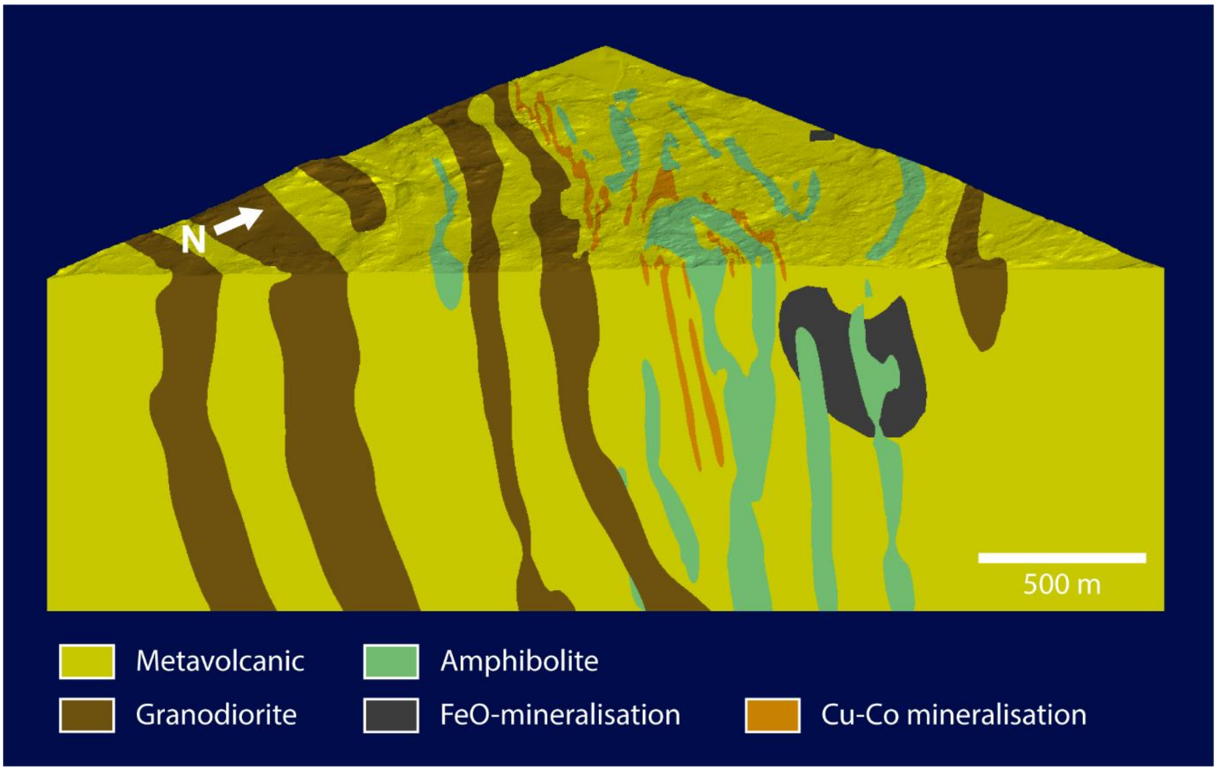

Figure 29. A 3D interpretation of the possible extent of rocks and mineralisations at Vena gruvfält. N.B.1: Bore hole density is low and spatial uncertainty therefore generally large. N.B.2: The horizontal and vertical continuousness of the sulphide mineralisation is deliberately exaggerated for visualisation purposes. N.B.3: The iron oxide mineralisation is based merely on geophysical data, the size of the mineralised body is therefore undoubtedly exaggerated.

Lithogeochemistry

Whole-rock lithogeochemical analysis was performed for in total 98 samples (Fig. 2), the results of which are presented in different diagrams below. All analyses are available from SGU's lithogeochemistry database, and also accessible through SGU's map viewer Bergartskemi (in Swedish). The prefix "mineralised" is used for samples that contain macro-scale occurrences of sulphides or oxides.

Whole-rock compositional data may be used for classification of (sub-)volcanic rocks. One of the most common chemical classifications is the TAS (total alkali versus silica) diagram, according to which the metavolcanic rocks from Vena gruvfält and surrounding areas plots somewhere between a normal volcanic and a trachy volcanic series. (Fig. 30a).

Widespread K-alteration is known from the area (Jansson et al. 2017), which may explain the high alkali content of the metavolcanic rocks at Vena gruvfält. To evaluate the effect of K-alteration, the alteration diagram of Hughes et al. (1973) was used (Fig. 30b). This strongly indicates that a vast majority of the Vena volcanic rocks indeed are K-altered, some of them rather extensively.

The presence of cordierite-, anthophyllite- and enstatite-bearing metamorphic assemblages in the metavolcanic rocks (Fig. 16c–f) is interpreted as localised Mg-alteration prior to regional metamorphism (cf. Trägårdh 1991). Because Fe is a major constituent in the mineralisations, the degree of Mg-alteration of mineralised samples cannot be evaluated with an approach analogous to that of Hughes (1973) for alkali alteration. However, about half of the barren metavolcanic samples show indications of significant Mg alteration (Fig. 30c).

Due to the alteration history of the metavolcanic rocks, it is preferable to use alternative classifications that utilise immobile elements, i.e. components that remain unaffected by hydrothermal alteration. Following this approach, the Vena volcanic rocks plots towards a normal basalt-rhyolite volcanic series (Fig. 30d).

Amphibolites are mostly gabbroic to monzogabbroic in composition, whereas mineralised varieties show larger spread towards monzo- and syenodiorites (Fig. 30e). The latter might indicate silicification and alkali alteration due to hydrothermal processes related to the mineralisations. Early orogenic granodiorites all fall within the expected field for granodiorites (Fig. 30e). The only analysed synorogenic granitoid is compositionally classified as alkali granite. The dolerite dyke has the composition of a monzogabbro.

A rock's chemical composition may also aid to decipher the tectonic setting in which it was formed. With respect to chemical composition only, the amphibolites at Vena gruvfält seem to have formed along an active tectonic margin: viz. mid-ocean ridge, continental arc, or oceanic arc (Fig. 31a). The undeformed dolerite dyke plots within the field for within-plate basalts, which suggests that the dyke formed in a different tectonic setting. The volcanic rocks almost exclusively have trace-element compositions typical for formation at an active continental margin (Fig. 31b–d), which may indicate near-coeval formation of the amphibolites but also fits the general tectonic model for the Bergslagen province (cf. Stephens et al. 2009). For all these diagrams, mineralised samples should be treated with caution as the plotted trace elements may have been mobilised by the mineralising fluids.

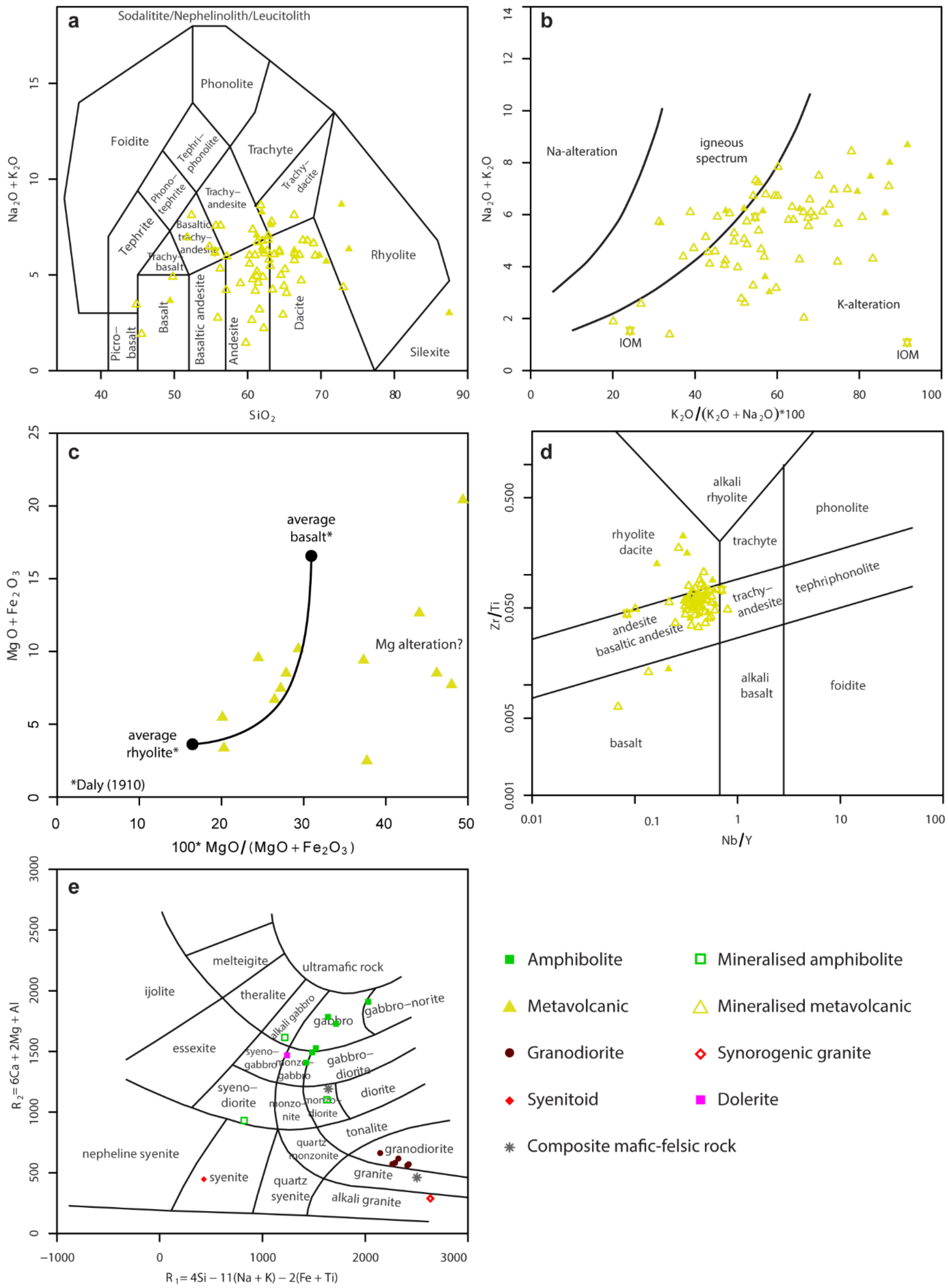

Figure 30. A. Classification of metavolcanic rocks based on their alkali and silica contents (TAS; Middlemost 1994). **B.** Diagram used to evaluate the degree of alkali alteration in metavolcanic rocks (Hughes 1973), most samples fall outside the igneous spectrum and are likely K-altered. IOM = iron-oxide mineralisation. **C.** Evaluation of Mg alteration analogous to that in B., but only plotting barren metavolcanic rocks due to that Fe_2O_3 is a major constituent in the mineralisations. Average volcanic sequence from Daly (1910). **D.** Classification based on immobile elements indicates that the sampled volcanic rocks fall within a normal basalt-rhyolite volcanic series (Pearce 1996). **E.** Classification diagram for plutonic rocks (De la Roche et al. 1980).

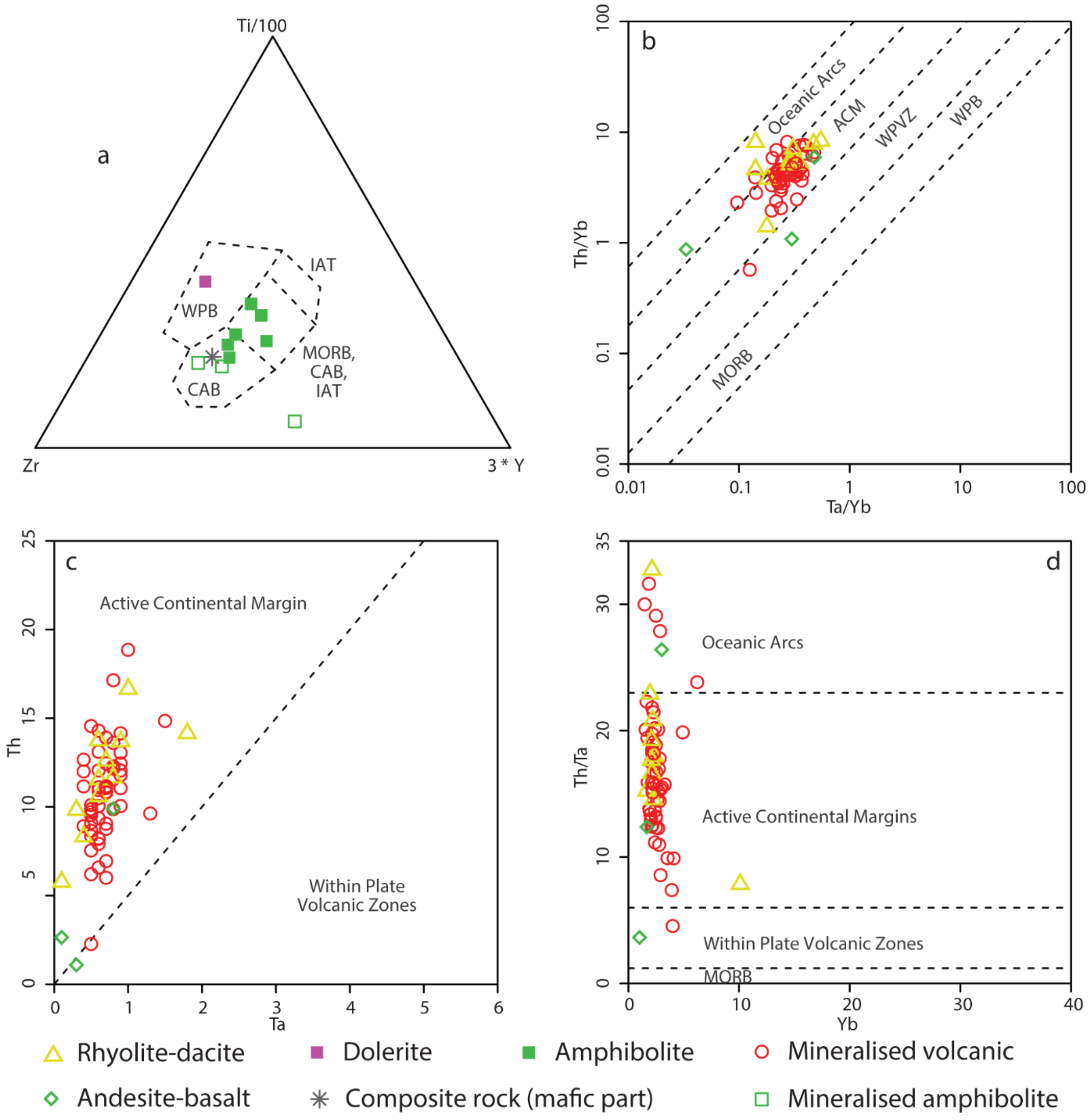

Figure 31. A. Classification of tectonic setting for basic intrusive rocks. WPB = within plate basalt, IAT = island arc tholeiite, MORB = mid-ocean ridge basalt, CAB = continental arc basalt (Pearce & Cann 1973). **B–D.** Classification of tectonic setting for volcanic rocks (Schandl & Gorton 2002). ACM = active continental margin, WPVZ = within plate volcanic zone.

The volcanic rocks are in general enriched in large-ion lithophile elements (LILE, e.g. Ba, Rb, Th, K) relative to high field strength elements (HFSE, e.g. Zr, Hf, Y). Notable are the negative anomalies for Nb, Sr, P, and Ti (Fig. 32), of which the Nb anomaly indicates formation at an active continental margin (Brown et al. 1984), whereas the others may be attributed to magmatic fractionation of plagioclase, apatite and a Ti-bearing mineral. The volcanic rocks are generally enriched in light REE (LREE; La to Sm) versus heavy REE (HREE; Gd to Lu) and have relatively flat REE trends, which together may indicate a subduction-related formation (Kelemen et al. 2003). Negative Eu anomalies are expected for rock formed from magmas that have previously fractionated plagioclase. One of the sulphide mineralised samples show significant enrichment of REE in comparison with the other mineralised and unmineralised volcanic rocks, whereas one of the iron-oxide mineralised samples shows enrichment only of LREE and another even overall depletion of REE.

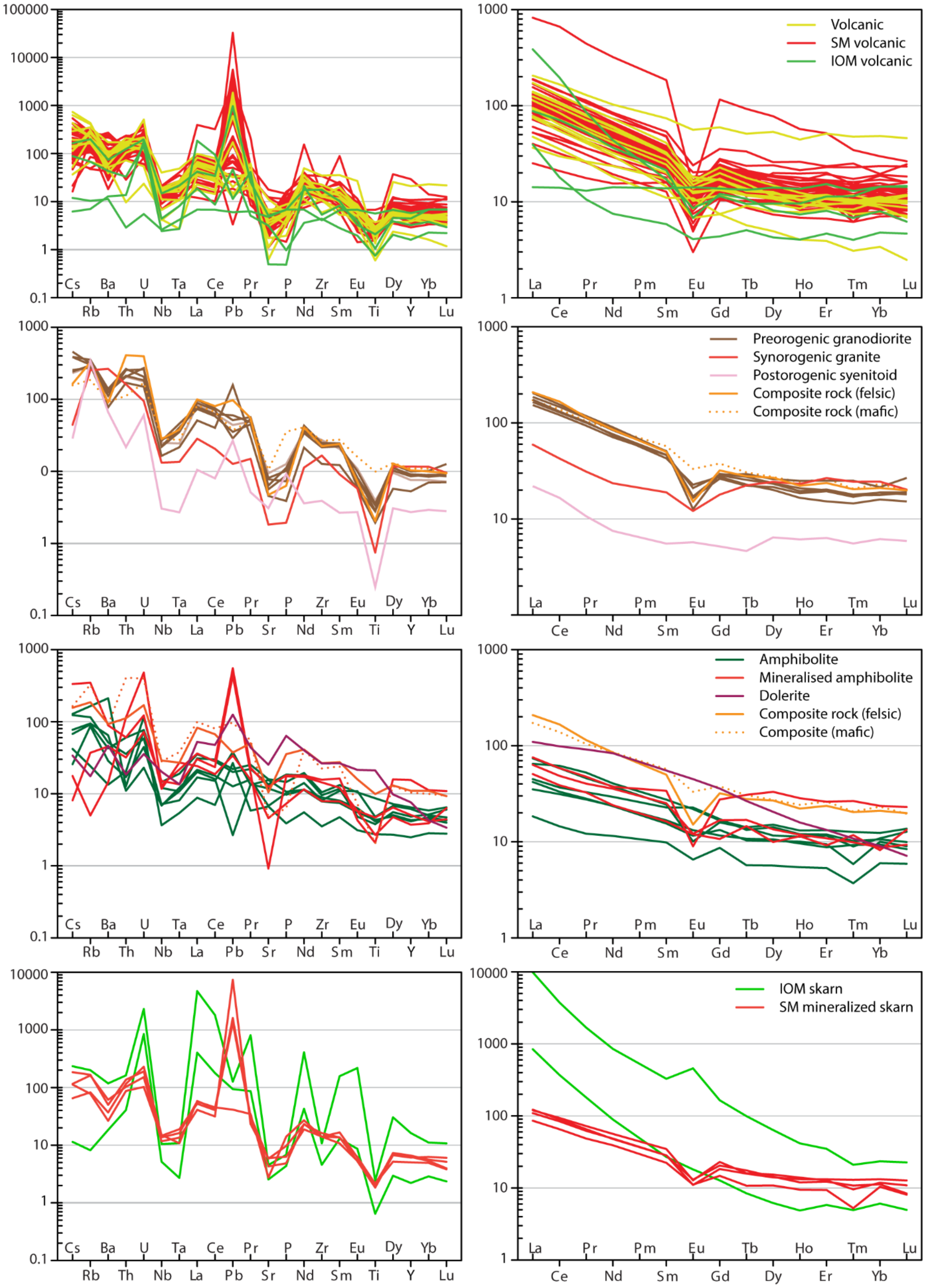

Figure 32. Diagrams of trace elements normalised to primitive mantle (McDonough & Sun 1995) and REE normalised to chondrites (Boynton 1984) for the different rock types sampled in the Vena gruvfält area. SM = sulphide-mineralised, and IOM = iron-oxide mineralised.

Early orogenic granodiorites show trace-element trends similar to those of the volcanic rocks; however, so do the synorogenic alkali granite and the late- to post-orogenic composite mafic-felsic rock. On the other hand, REE-patterns for the felsic intrusive rocks show three distinct groups:

1. Negative slope in the LREE and flat HREE with pronounced negative Eu anomaly for early orogenic granodiorites and late- to post-orogenic composite mafic-felsic rock.
2. Negatively sloping LREE and flat HREE with Eu anomaly but where most LREE plot below the HREE plateau.
3. Negatively sloping LREE and flat HREE for the late- to post-orogenic syenitoid that lacks Eu anomaly, however, the shape is curved rather than kinked as for group (1).

Early orogenic granodiorites and the late- to post-orogenic composite mafic-felsic rock conspicuously plot together within a very narrow span for both trace elements and REE, it is unknown whether this is pure coincidence, or reflects melting of similar source material or assimilation of the granodiorites by the composite mafic-felsic rock magmas. Depletion of LREE in the syn-orogenic alkali granite may indicate partial melting of a monazite±allanite-bearing and/or epidote-bearing source rock that trap light and middle REE and prevent their partitioning in the liquid.

Amphibolites show enrichment of LILE versus HFSE, and negative anomalies for Th, Ta and Nb, indicative of basalts formed in subduction zones (Pearce & Parkinson 1993). They show a slightly negatively sloping trend for LREE and flat trend for HREE, with absent or very minor negative Eu anomaly. The lack of Eu anomaly is expected for rocks formed from magmas that have not fractionated plagioclase. Mineralised amphibolites, on the other hand, show negative anomalies for Sr and Eu. Both elements substitute for Ca in plagioclase and should not suffer depletion in basaltic rocks compared to primordial mantle unless the magma is Ca-poor (e.g. O'Hara & Nui 2009), although that seems unlikely given that the unmineralised amphibolites lack these anomalies. Possible explanations include albitisation or destruction of plagioclase by the mineralising fluids, which mobilises Sr and Eu, transport them to another site and causes depletion of the original rock (cf. Burgath et al. 2002).

The mineralisations at Vena gruvfält are enriched in e.g. Ag, Co, Cu, Mo, Pb, REE, and Zn in comparison to their barren host rocks (Fig. 33). In mineralised samples, Co show fairly good correlation with Mo, some correlation with Cu and Ag, and lacks correlation with Zn and Pb.

Conspicuously, the only sulphide-mineralised sample that shows significantly elevated REE content is also the richest in Co. Copper on the other hand show good correlation with Ag and some correlation with Zn. Zinc and Pb are also well-correlated.

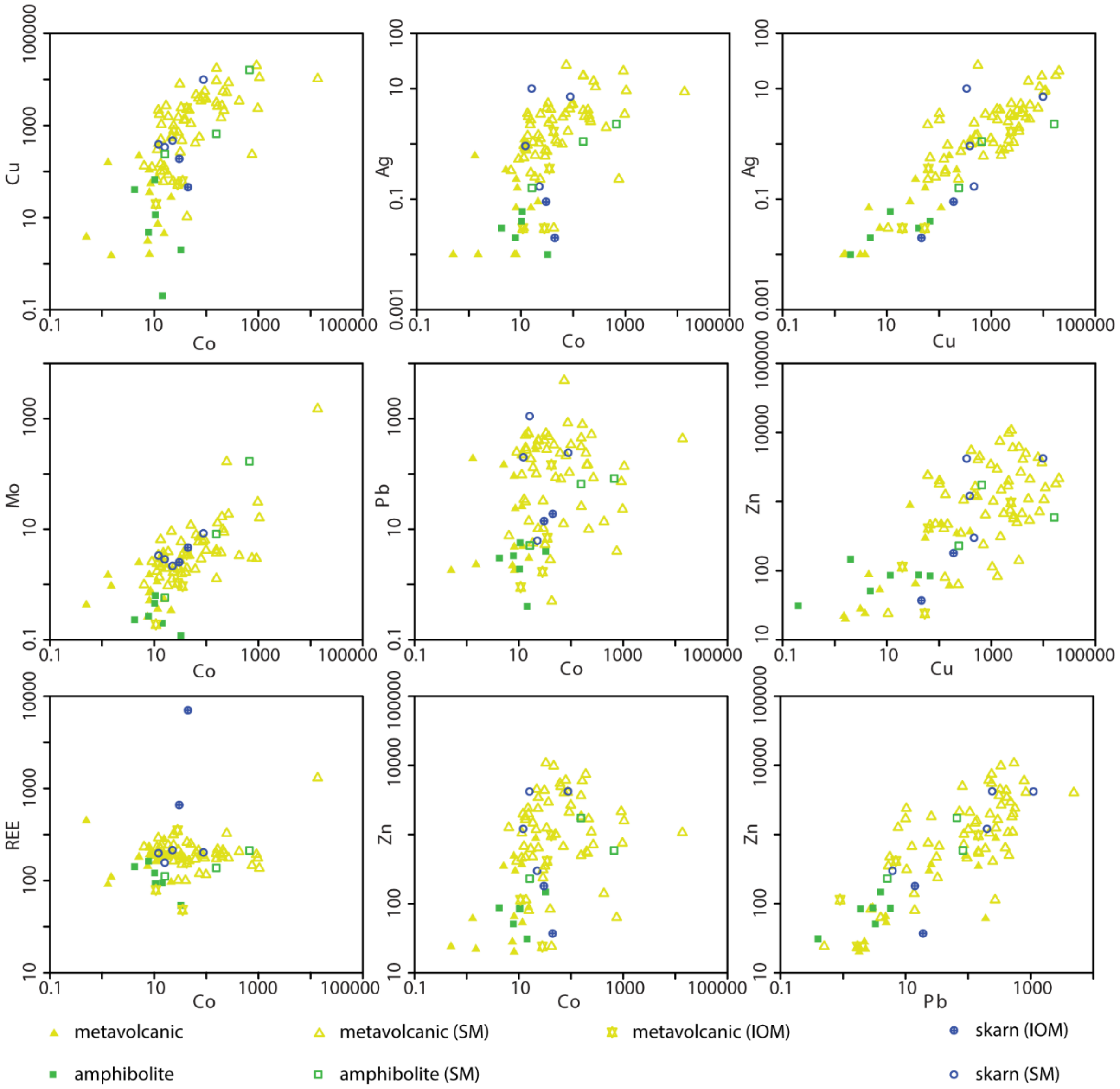

Figure 33. Bivariate plots for a selection of metals within the mineralisations. SM = sulphide-mineralised, and IOM = iron-oxide mineralised.

Genesis and evolution of the rocks and mineralisations at *Vena gruvfält*

Genesis of the mineralisations

Textural, structural, chemical, and thermobarometric observations and data suggest that the sulphide mineralisations formed shortly after the amphibolites and the metavolcanics (ca 1.89 Ga; unpublished SGU data). This included precipitation of pyrite, pyrrhotite, chalcopyrite, sphalerite, cobaltite, carrolite, galena, arsenopyrite, skutterudite, molybdenite, and minor REE minerals from a hydrothermal solution (Leopardi 2020; this study). The distribution of elements and assemblages was controlled by the evolution of the hydrothermal fluid as it interacted with the surrounding rocks and both dissolved and precipitated metals. Sulphide thermometry indicate that the Cu-Co minerals precipitated at higher temperatures than other sulphide minerals (Leopardi 2020), which implies that the Cu-Co-mineralised zones would be more proximal to the centre of the hydrothermal system(s) than the Pb-Zn-mineralised zones. However, this assumes that the hydrothermal system remained stationary during the formation of the mineralisations. A moving hydrothermal system would also explain this type of zonation.

The Skuru gruvor iron-oxide skarns share many features with the Bastnäs type mineralisations (e.g. Sahlström et al. 2019), such as minor sulphide occurrences within the otherwise magnetite-dominated assemblage (Fig. 13) and occurrence of REE-bearing minerals that are especially enriched in LREE (allanite; Fig. 13, 33). Elevated REE contents were not detected in any of the other sampled iron-oxide mineralisations, such as the mines at Lövfallafältet, but otherwise these are very similar to Skuru gruvor and show a magnetite-rich skarn assemblage with minor sulphides. The Skuru gruvor iron-oxide mineralisation shows different characteristics from those at Nyhyttegruvan and Åmme gruvor south and west of Vena gruvfält, which in contrast show significant Mn-enrichment and apatite-(F) as the main REE-hosting mineral (Ivarsson 2019).

After formation, the sulphide mineralisations were affected by relatively high-T, low-P Svecokarelian metamorphism around 1.87 Ga (Fig. 17). Emplacement of granodiorites just before or at the early stages of metamorphism (e.g. Stephens & Jansson 2020), as well as prograde and retrograde metamorphic fluid pulses, constitute possible events for remobilisation of metals and redistribution by dissolution and reprecipitation of minerals within the mineralisations. Textural and structural observations indicate that mechanical, hydrothermal and melt-assisted remobilisation of the sulphides took place during metamorphism (Leopardi 2020). Through these processes, arsenopyrite, pyrite, galena, and Bi-Sb-minerals were remobilised and partially redistributed within the deposit during prograde metamorphism. However, it remains unknown whether the spatial extent of remobilisation exceeded thin section-scale, in which most observations were made. Retrograde metamorphism only induced minor remobilisation of the sulphide assemblages, as indicated by minor pyrite precipitation within pyrite-chlorite-calcite veins.

Late- to post-orogenic granites and pegmatites are also possible sources of heat and fluids for remobilisation of the sulphide assemblages. Localised occurrences of chalcopyrite, pyrrhotite, and cobaltite, especially within late pegmatites, are interpreted as assimilation of sulphides from the mineralisations by the late- to post-orogenic magmas. The amount of sulphides locally observed exceeds what is expected for pegmatitic systems and rules out a primary igneous origin of the sulphides. Historically, the pegmatites were hypothesised as the source of the mineralisations (Tegengren et al. 1924), a hypothesis that was later disregarded by Åberg (1988). Our observations, likewise those of Leopardi (2020), are that this seems to have very limited effect on the mineralisations and only caused negligible remobilisation of metals.

Further evidence of a complex genetic evolution of the mineralisations comes from the lithogeochemical data (Fig. 33). Cobalt does not show perfect correlation with any other metal, which in line with the textural and structural observations indicates a complex history of multiple episodes of formation of Co-bearing minerals. That said, Co is to some extent correlated with Cu, which may indicate that metamorphic remobilisation of Co from the primary Cu-Co assemblages lead to further concentration of Co in secondary Co-bearing assemblages.

Gravimetric data indicate the presence of a major mafic intrusion at depth. Dampetorp, Vena gruvfält and Zinkgruvan are all positioned along the northeastern edge of this gravimetric anomaly (Fig. 20). This intrusion may have contributed to the mineralisations in the area, either as a primary source of metals or as a heat and/or fluid source for (re-)mobilisation and concentration of metals. However, as no outcrops yet have been observed on the surface, the field relations of the intrusion remain unknown likewise its age relative to the mineralisations.

As for many deposits in Bergslagen, the sulphide mineralisations at Vena gruvfält are closely associated with iron-oxide skarn mineralisations (Jansson & Allen 2013). Their stratigraphic relationship at Vena gruvfält is poorly constrained; however, according to Kumpulainen et al. (1996), the general stratigraphic younging direction is to the southwest, which would imply that the iron-oxide skarns underlies the sulphide mineralisations. The tight folding of the area adds complexity (Fig. 10A), and it is unknown how this affects the stratigraphic direction.

The Bastnäs iron oxide mineralisations are estimated to have formed at temperatures exceeding 450 °C (Sahlström et al. 2019). It is likely that the iron oxide mineralisations at Vena gruvfält formed at similar temperatures, whereas sulphide thermometry indicates sulphide precipitation below 350 °C (Leopardi 2020). The simplest explanation for the discrepancy in formation temperature is that the two mineralisation types are genetically unrelated; however, their close spatial relationship argues against this. Two alternative scenarios are proposed as explanations for shared genesis: (1) stepwise precipitation from an evolving hydrothermal system, and (2) simultaneous precipitation at different distance from the centre of the hydrothermal system.

Stepwise precipitation would occur in a hydrothermal cell that starts off as a hot magmatic system, with fluids that deposit iron oxides and REE minerals, but due to cooling evolves into a system that deposits base metal sulphides in a sequence of mineral assemblages as a function of their stability fields. In this scenario, the REE in the locally REE-enriched sulphide mineralisation samples might speculatively be sourced through remobilisation from iron-oxide mineralisations. In the second scenario, iron-oxide mineralisations represent the proximal parts of the hydrothermal system, whereas the sulphide mineralisations represents more distal parts of the deposit. The lack of major sulphide occurrences in the iron-oxide mineralisations, as is expected from a stepwise precipitation, argues against the first scenario, unless the system moved position during cooling. Additional work is needed to conclusively constrain the relationship between the iron-oxide and sulphide mineralisations at Vena gruvfält and entangle their possibly shared origin.

The role of K- and Mg-alterations

Metals are often transported in hydrothermal solutions that may chemically alter the rocks it encounters. The analysed volcanic rocks are to varying extent K- and Mg-altered (Fig. 30b–c), i.e. enriched in K and Mg compared to the igneous spectrum. Comparison of the K_2O:Na_2O ratio and S as a proxy for the grade of the mineralisation shows that the highest grades are found in moderately K-altered metavolcanic rocks and that the optimum $K_2O/(Na_2O+K_2O)$ lies around 55–60% (Fig. 34a).

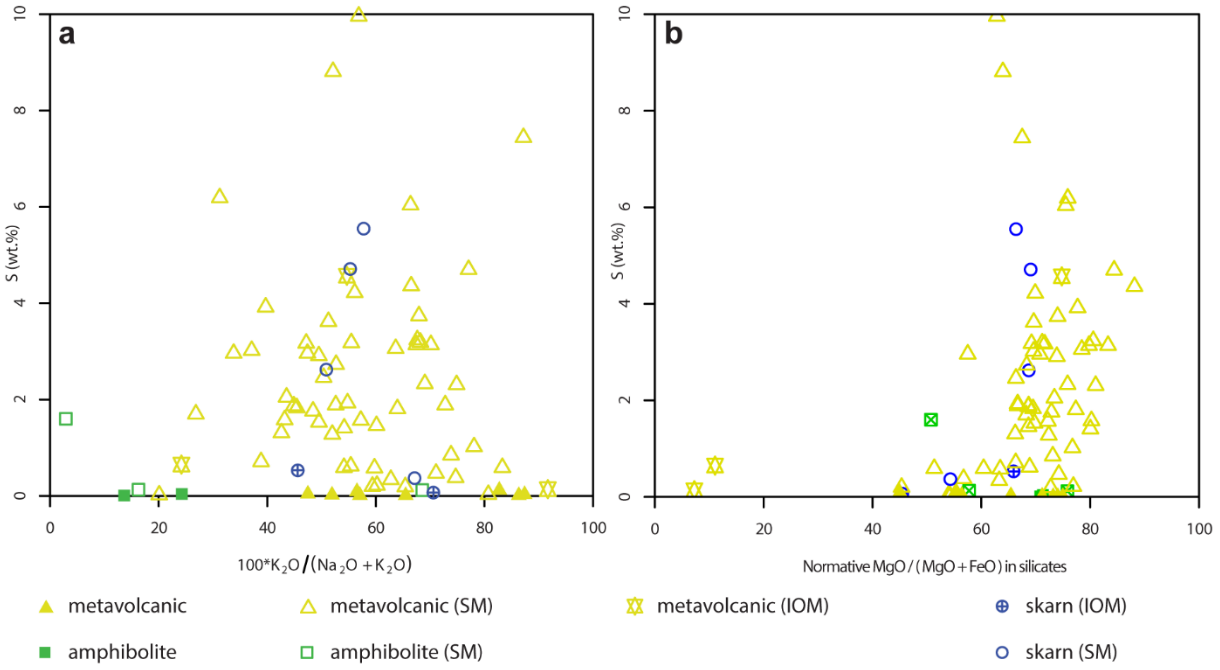

Figure 34. A. Plot of K:Na ratio versus total S content. **B.** Plot of the estimated pre-mineralisation Mg:Fe ratio as represented by the normative MgO/(MgO+FeO) in silicates.

The analogous comparison is not possible for Mg-altered rocks, at least not straight forward, because Fe is part of the mineralisation and likely was added by formation of pyrrhotite and other Fe-bearing sulphides. Using the CIPW norm, it is possible to calculate the normative

MgO/(MgO+FeO) for the silicate minerals only. Under the likely flawed assumption that silicates were largely left untouched, or at least had not their Mg:Fe ratios altered by the mineralising fluids, this ratio should reflect the composition of the rocks prior to mineralisation. The relationships between normative silicate MgO/(MgO+FeO) and total S content shows that the most Mg-altered rocks have the highest grades (Fig. 34b). An alternative interpretation is that silicates were affected by the fluids responsible for the Mg-alteration, and that this process was coeval with deposition of the sulphide mineralisation.

The reason for the mineralisation's affinity to moderately K-altered rocks, over the more extensively K-altered samples, as well as to the Mg-altered rocks, remains unknown. Cordierite-bearing, Mg-altered metavolcanic rocks are often found in close vicinity to the mineralised zones, and as shown in Figure 30b most samples are K-altered, which includes those collected from and near mineralisations. A possible scenario is that the varyingly K- and Mg-altered rocks make up zones in individual or a combined metasomatic column(s), where fluid conditions were optimal for sulphide deposition within the zones of moderate K-alteration and that of extensive Mg-alteration, where the mineralisations formed. Consequently, at least some portion of the metals in the mineralisations may have been sourced from the K-altered zones outside the optimum conditions for redeposition and from the less Mg-altered zones. Although this is all highly speculative, future detailed studies could confirm and resolve the spatial and chemical dependencies of such a metasomatic system.

Temperature-time evolution of Vena gruvfält

The temperature-time evolution of Vena gruvfält is summarised in (Fig. 35). Sulphide thermometry indicate exsolution of the main primary ore minerals between c. 200–400 °C (Leopardi 2020). A prograde, pre-peak metamorphic P-T estimation from the assemblage Crd+And+Bt+Grt yields temperatures of 517–612 °C (Fig. 17). The peak-metamorphic temperature remains unknown but somewhere around 650 °C would be an educated guess. Prograde metamorphism gave ample opportunities for melt- and fluid-assisted sulphide remobilisation as evidenced by observed textures (Leopardi 2020).

The retrograde metamorphic evolution is constrained using the chlorite thermometer provided by Xie et al. (1997); formation temperatures are calculated to 490–622 °C for chlorite as a retrograde metamorphic breakdown product of pyrite, 343–371 °C as the product of retrograde metamorphic reactions that involve chalcopyrite, 226–278 °C as the product of retrograde metamorphic breakdown of amphiboles, and 145–180 °C as the late breakdown product of pyrrhotite (Appendix 2g). This thermometer is not designed for calculations on chlorite formed from sulphides, the absolute temperatures should therefore be interpreted with extreme caution; however, they do indicate up to four different generations of chlorite, which formed from up to four different processes and events. The thermometer is known to give fairly robust estimates on greenschist-facies metamorphic chlorite formation, which should include the retrograde breakdown of amphiboles to chlorite.

Sulphides were remobilised during retrograde metamorphism, as indicated by the presence of sulphides in late, undeformed veins (Leopardi 2020). Pyrrhotite breakdown marks the late, possibly post-orogenic, alteration of sulphides, after which supergene alteration is responsible for the remaining observed minor alteration products, such as delafossite, covellite and other hydroxides and sulphates.

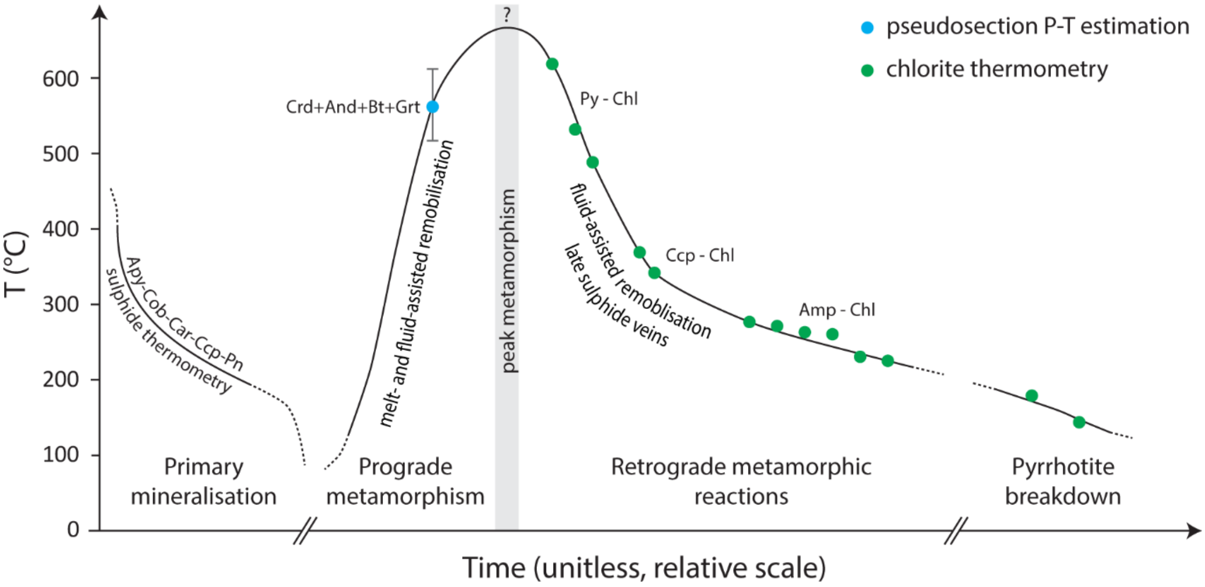

Figure 35. A speculative temperature-time path for Vena gruvfält, based on sulphide thermometry for the main mineralisation event (Leopardi 2020), prograde metamorphic P-T estimation (Fig. 17), and chlorite thermometry for various retrograde metamorphic reactions (Appendix 2g).

TUNABERG

Alexander Lewerentz, Edine Bakker & Peter Hedin

Introduction

The surveyed area is located ca 10–15 km south of Nyköping, Södermanland County, and largely coincide with the historical Tunaberg parish. A large number of historical mines are found in the area, of which the oldest are mentioned by Eric of Pomerania in his letter of privilege of the year 1420 but likely were mined even before that (Erdmann 1848; Hoppe 1887). The main commodities were initially Fe and Cu, but later also Co, Zn, Pb, and Mn were produced from mines in the area.

In the area around Koppartorp village (Fig. 36), mining was initiated in the 1750s, initially focused on copper production but shortly also cobalt was produced (Erdmann 1848). During the years 1810–1916, before that no records are available, a total of 670 metric tonnes of mixed copper-cobalt ore and 4,450 metric tonnes of copper ore was mined, which contained c. 0.1–2% Co and 1–2% Cu (Tegengren et al. 1924; Kommerskollegium 1917). A total of 818 metric tonnes of zinc ore was mined between 1914 and 1916 from the neighbouring Börjelstorp and Skara mines, with an average of 35% Zn (Kommerskollegium 1915; 1916; 1917). Tunaberg's over 500 years long history of mining was ended by the shutdown of the Stora Uttervik manganese mine in 1956 (Hök 1956).

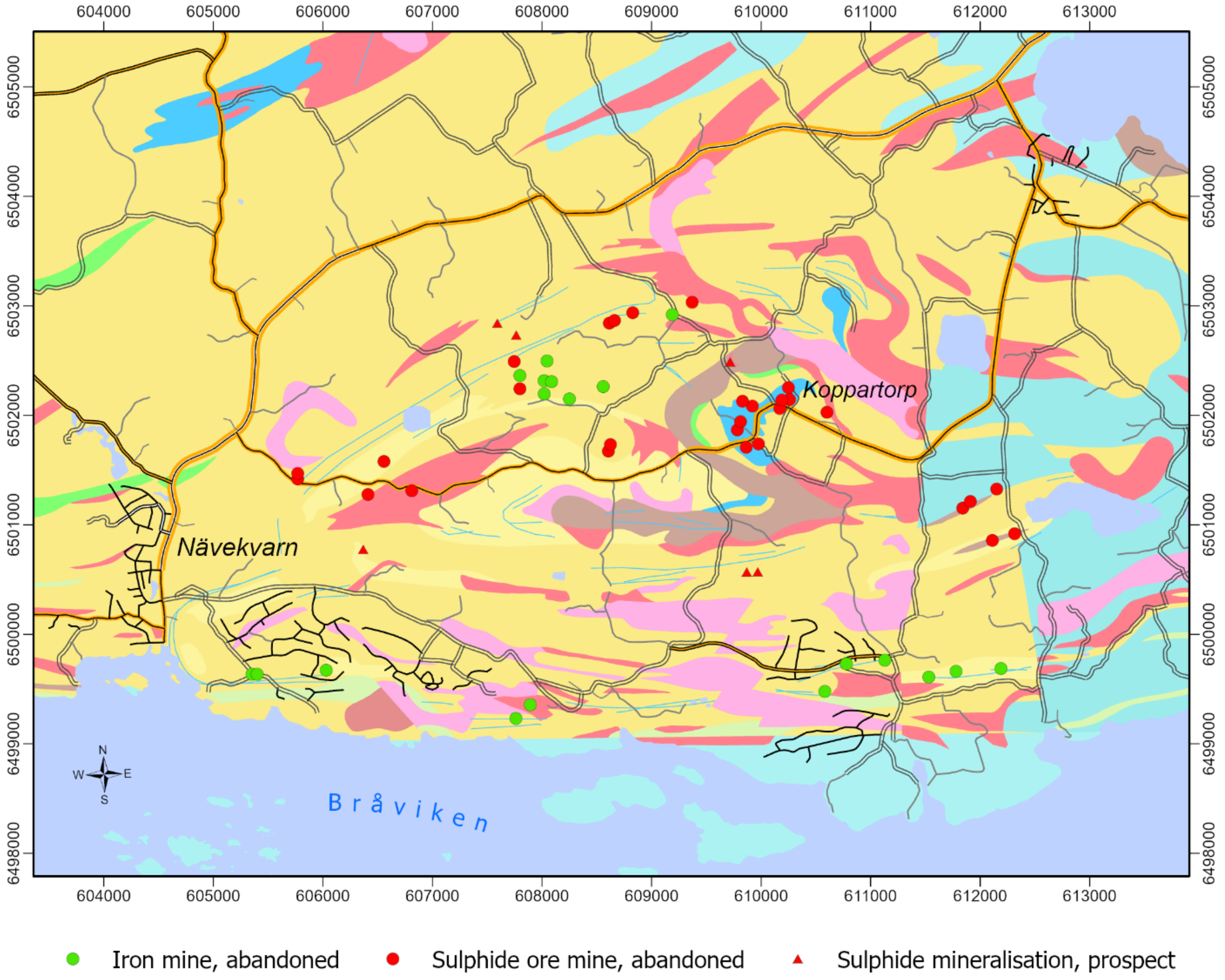

Figure 36. Geological map of the Tunaberg area, with known iron-oxide and sulphide mineralisations marked. Rock types according to Figure 17. Coordinates in SWEREF99TM.

The Tunaberg area has a long history of geological and mineralogical studies. For example, the origin of a pyroxene-rich skarn rock found in the area have been extensively discussed over the years, earlier interpreted as eulysite and thereby the metamorphic product of ultrabasic intrusive rocks (e.g. Suckow 1831, Erdmann 1848, Walmstedt 1849, Erdmann 1867, Lundström 1974). Mormorsgruvan, one of the many historical mines in the area, is also the type locality for the pyroxene mineral species hedenbergite, which originally was described and characterized by Hedenberg (1807) whom it later was named after by Berzelius (1819).

Geological maps with detailed descriptions of the geology are available by Erdmann (1867) and Lundström (1974). Mapping of rock quality in the area was undertaken by Antal Lundin et al. (2006), based on which minor changes were made in the SGU bedrock database (Claeson et al., 2013). The regional geology of the Bergslagen Ore Province is described by Stephens et al. (2009).

The ores and mineralisations are described by Klaproth (1797), Erdmann (1848), Johansson (1909), and Tegengren et al. (1924), and was also thoroughly studied by Dobbe (1991a, 1991b, 1993, 1994a, 1994b). Following the work by Dobbe et al. (1994) and Dobbe & Zakrzewski (1998), Tunaberg is the type locality for the minerals kieftite and oenite.

SGU acquired geophysical data over the area in an airborne campaign in 1970 and gravity data have been collected on the ground in the area for regional coverage since the 1940's. These datasets were used in the geophysical map compilations in Stephens et al. (2009). Petrophysical samples were collected and analysed in conjunction with the previously mentioned rock quality investigations.

Geological mapping and sampling

Geological mapping and sampling were undertaken by Alexander Lewerentz and Edine Bakker in June 2019 (Fig. 37). The mapping was focused along c. ten profiles, as much as possible orientated perpendicular to strike of the structures in the area. In addition, most of the known mineralisations were investigated and sampled. Drill cores were logged and sampled at SGU's facility in Malå. In total 143 observations from outcrops, abandoned mines, and drill cores have been added to SGU's outcrop database. Our observations are generally in good agreement with previous map material, i.e. Lundström (1974) and SGU's bedrock database.

Samples were collected from outcrop, waste piles and drill core for preparation of thin sections and polished ore sections, as well as lithogeochemical analyses for compositional characterisation of the rocks and mineralisations. In total 44 thin sections and ore sections were described, and 56 samples analysed and added to SGU's lithogeochemistry database. Locations for below mentioned, depictured and discussed outcrops and samples are presented in Table 3.

Structural observations and measurements conform with previous interpretations of the complex deformational history of the Tunaberg area by Lundström (1973), according to which the mines near Koppartorp lies within a refolded, antiformal structure (Fig. 38). Further improvement of this model requires additional detailed investigations outside the scope of the limited and mineralisation-focused fieldwork presented in this report, such as further structural observations and measurements but also additional, modern, high-resolution geophysical data.

Table 3. Coordinates in SWEREF99TM for selected outcrops and samples.

Outcrop/sample ID	SWEREF99TM N	SWEREF99TM E
ALZ191001	6498534	610569
ALZ191006	6499597	611949
ALZ191007	6499559	611943
ALZ191015	6499221	610630
ALZ191018	6498988	610628
ALZ191040	6500121	605277
ALZ191049	6501205	611922
ALZ191060	6499657	605576
ALZ191074	6501473	608726
EDB190054	6501691	609908
EDB190054	6501691	609908
EDB190067	6501855	609816
EDB190069	6501957	609816
EDB190070	6502065	609849

*Sample IDs are identical to their respective Outcrop IDs, with the addition of a letter: e.g. EDB190069A.

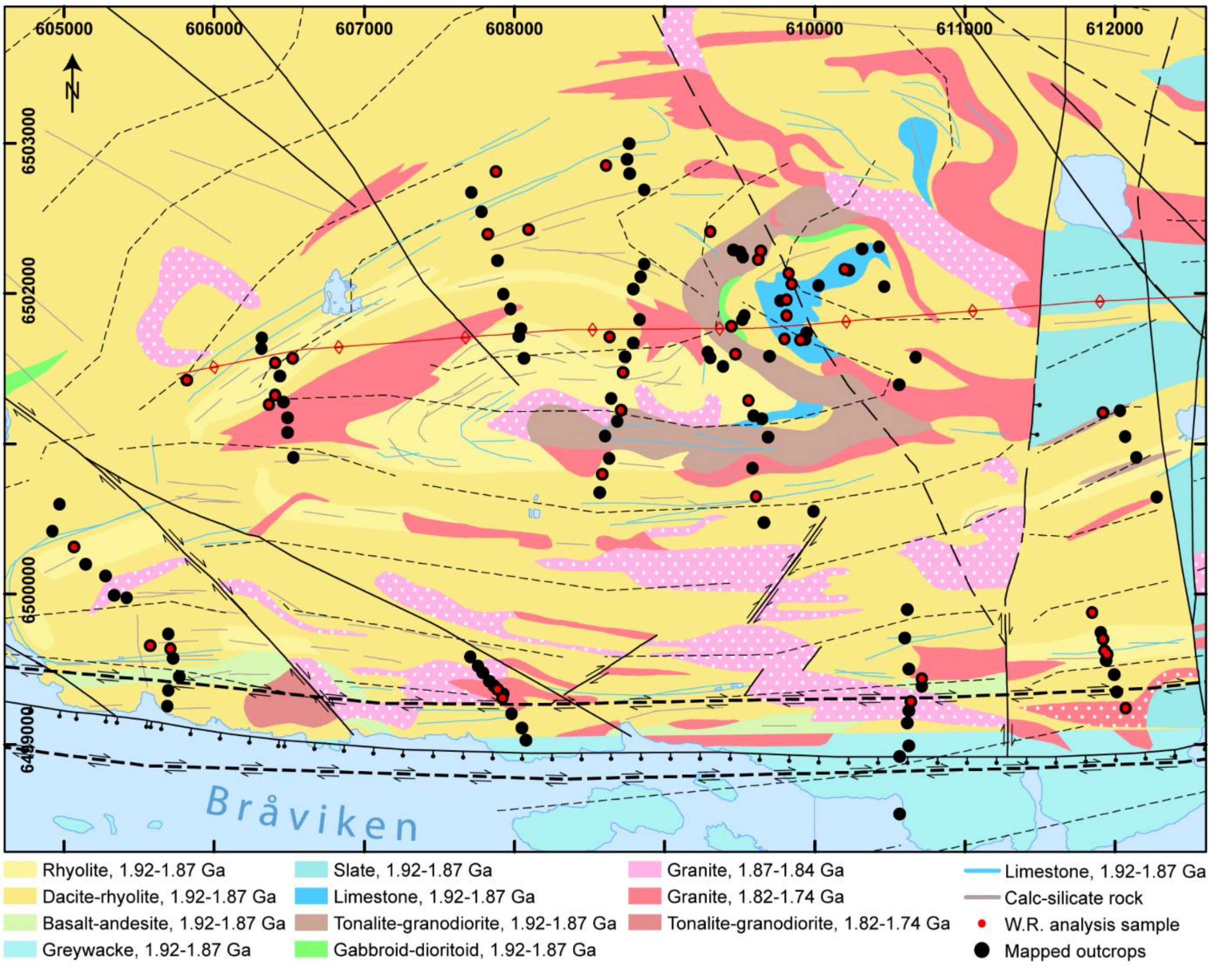

Figure 37. Geological map of the Tunaberg area, based on SGU's bedrock database. Studied outcrops and sample locations are marked. Coordinates in SWEREF99TM.

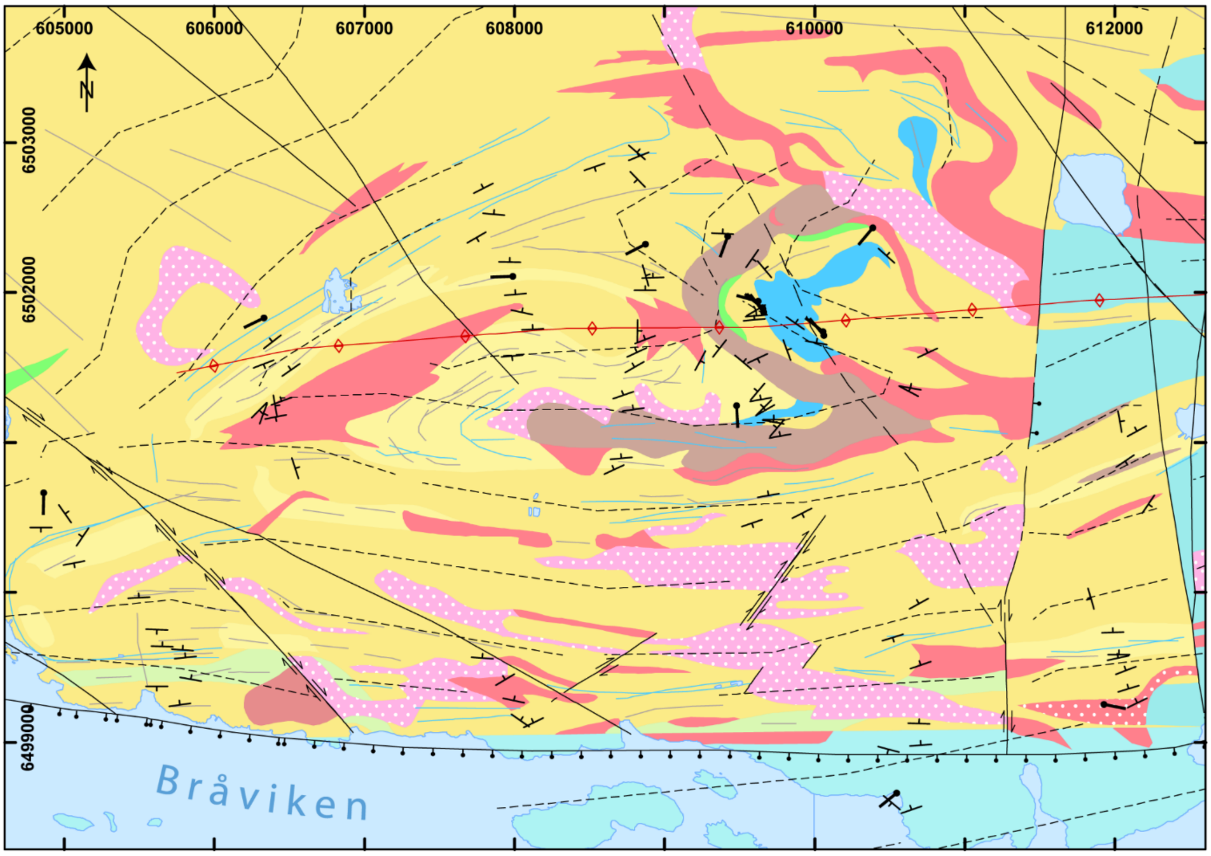

Figure 38. Geological map of the Tunaberg area. Structural measurements of foliation and fold axes are marked using standard symbology. Rock types according to Figure 37. Coordinates in SWEREF99TM.

Descriptions of mapped rocks

The oldest rocks in the area are metamorphosed supracrustal rocks of either volcanic or sedimentary origin. Subordinate marble, skarn, or mixed varieties thereof occur as layers or horizons within the supracrustal rocks. Pre- to early-orogenic intrusive rocks of basic and granitoid composition occur very scarcely. Coarse-grained, locally pegmatitic, granitic rocks likely represent syn-orogenic melts. These rocks are post-dated by late- to post-orogenic, porphyritic, massive, granite, together with likewise undeformed pegmatites. Detailed descriptions of these rock types follow below.

Supracrustal rocks occupy a vast majority of the studied area, these are either of volcanic or sedimentary origin. According to the interpretation offered by Lundström (1974) they are mainly metasedimentary rocks, an interpretation largely based in the Al_2O_3- and SiO_2-rich compositions that locally allowed for the formation of cordierite, andalusite and sillimanite during metamorphism. However, later studies have shown that Mg-alteration and other pre-metamorphic hydrothermal processes may cause residual enrichment of Al_2O_3 and SiO_2 in volcanic rocks (e.g. Trägårdh 1991), occurrence of Al-rich metamorphic minerals is therefore not unequivocal evidence for either genesis. As a result of localised mapping efforts during a rock quality survey of the area (Antal Lundin et al. 2006), most of the area's supracrustal rocks were reinterpreted as of volcanic origin, which also was implemented to SGU's bedrock database (Fig. 37). They also conclude that based on their efforts, rocks of sedimentary origin cannot be entirely ruled out. Due to the strong deformation and extensive migmatisation that have imprinted a diatexitic structure on most supracrustal rocks in the area, conclusive interpretation of volcanic versus sedimentary origin is in most cases nearly impossible. It is therefore our opinion that a more realistic approach would be to visualise these rocks in the map as migmatites or diatexites, rather than their highly uncertain primary genetic origin.

In the southernmost parts of the study area, supracrustal rocks of possibly sedimentary origin crops out along the shores of Bråviken (Fig. 37). These are rocks whose interbedded quartz-rich and mica-rich layers may be interpreted as a sedimentary sandstone-mudstone sequence. The quartz-rich layers give a well-sorted appearance, which further substantiates the evidence towards a sedimentary origin. On the other hand, these could also be redeposited volcanic material entirely without any other epiclastic input. Due to the strong deformation and migmatisation it is also hard to conclusively determine that these layers indeed are of primary sedimentary origin, and not formed by secondary processes such as metamorphism. The layering is parallel to foliation, which in turn is folded (Fig. 39a). Locally observed porphyroblasts of garnet are up to a few millimetres in size (Fig. 39b).

Farther north in the central parts of the studied area, also Lundström (1974) interprets the origin of supracrustal rocks as volcanic. These rocks are texturally and compositionally different from the previously described supracrustal rocks, but again the pronounced migmatisation renders genetic interpretations inconclusive. Extensive to complete recrystallisation likewise obscures any primary volcanic textures or structures. The primary grain size is unknown as most rocks likely were significantly coarsened during metamorphism, it is therefore generally not possible to distinguish between extrusive volcanic rocks and sub-volcanic shallow intrusions. Locally observed are cm-sized, folded patches of sillimanite-muscovite intergrowths (Fig. 39c–d). Larger sillimanite needles, c. 1 mm long and 0.1 mm across, seem to follow the folding rather than to have suffered deformation from it, which indicates syn-tectonic growth. Up to cm-sized, sub- to euhedral, inclusion-rich porphyroblasts of amphibole are seemingly unaffected by folding, which indicates the occurrence of an additional, post-tectonic phase of metamorphic recrystallisation (Fig. 39e–f).

In one of the rocks interpreted as volcanic, SEM-EDS analysis of plagioclase show pure albite, indicative of metamorphic crystallization or re-equilibration (Appendix 4). The detection of hyalophane in the same sample, with graphite as inclusions and along grain boundaries, indicates Ba- and C-rich, reducing conditions during its crystallisation, which texturally seems coeval with growth of galena and pyrrhotite.

Marble occurs as horizons or layers within the volcanic and sedimentary sequence (Fig. 40a). The grain size varies from fine-grained to coarse-grained, which probably reflects the degree of deformation-induced recrystallisation. Both calcite and dolomite are in field observed as carbonate minerals. Locally, a layering is accentuated by the occurrence of pyroxene, amphibole and other non-carbonate minerals. Additional minerals identified in thin section include garnet, olivine (commonly serpentinised), and titanite (Fig. 40b). SEM-EDS analysis confirms calcite as the main carbonate mineral, usually with minor contents of Mg, Mn and Fe. In one of the mineralised marble samples, tremolite is partially replaced by diopside along <10 μm wide rims in contact with calcite (Fig. 40c), which likely records the onset of the prograde reaction Trm + Cal = Di + Fo + CO_2 + H_2O that takes place at $T > 500$ °C ($X_{CO2} > 0.05$; cf. Masch & Heuss-Aßbichler 1991, Ferry 1996).

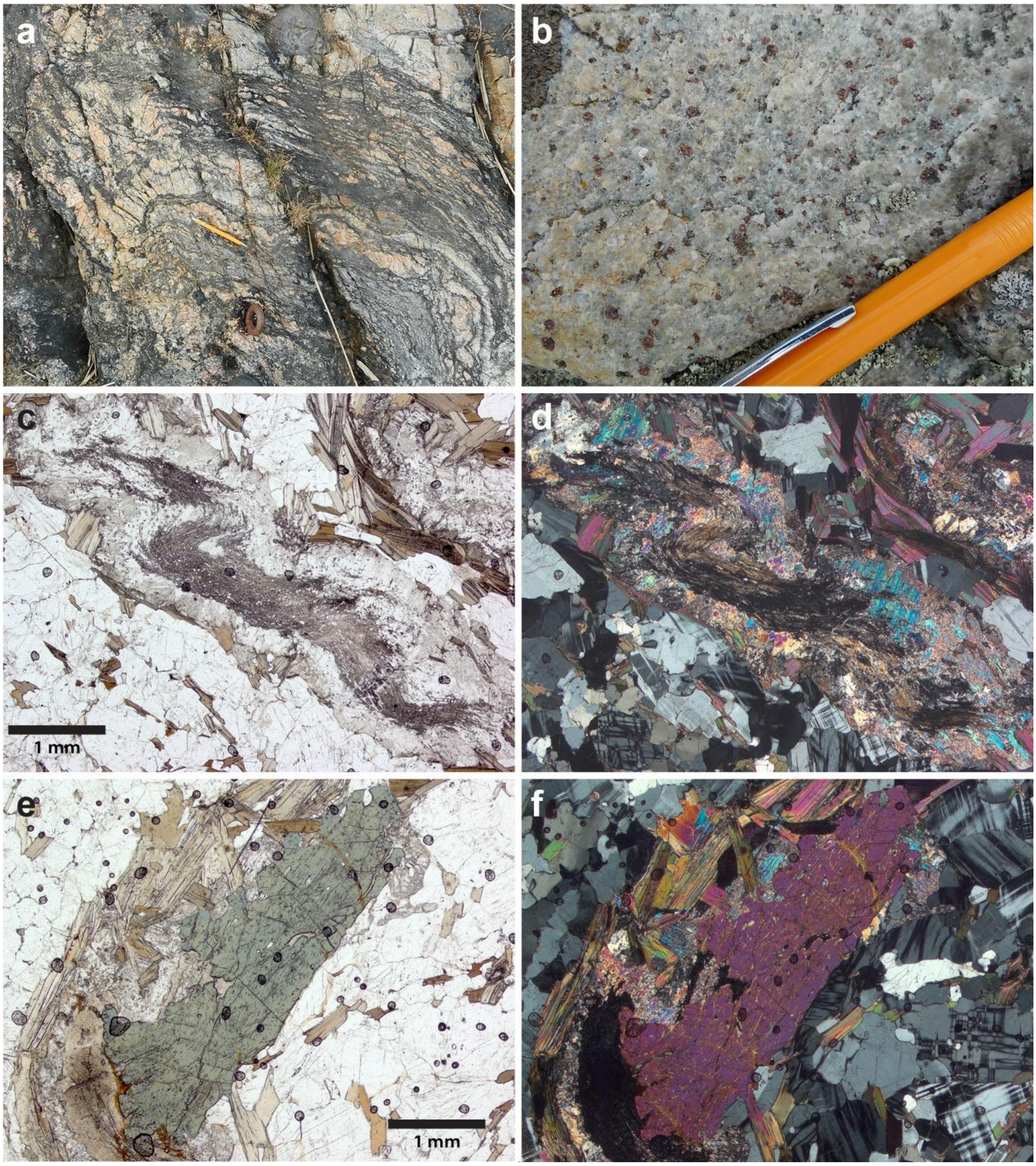

Figure 39. A. Migmatised supracrustal rock, possibly of sedimentary origin, and **B.** quartz-rich supracrustal rock with mm-sized porphyroblasts of garnet (ALZ191001). Pen for scale. **C–D.** Photomicrographs in ppl and xpl of a supracrustal rock (ALZ191074A), possibly metavolcanic, which consists of quartz, K-feldspar, plagioclase and biotite, as well as folded intergrowths of fibrolitic sillimanite and muscovite. Larger solitary sillimanite needles give the impression of syn-tectonic growth. **E–F.** Sub- to euhedral porphyroblasts of amphibole, up to a few mm in size, are unaffected by folding (ALZ191074A). Photos: Alexander Lewerentz.

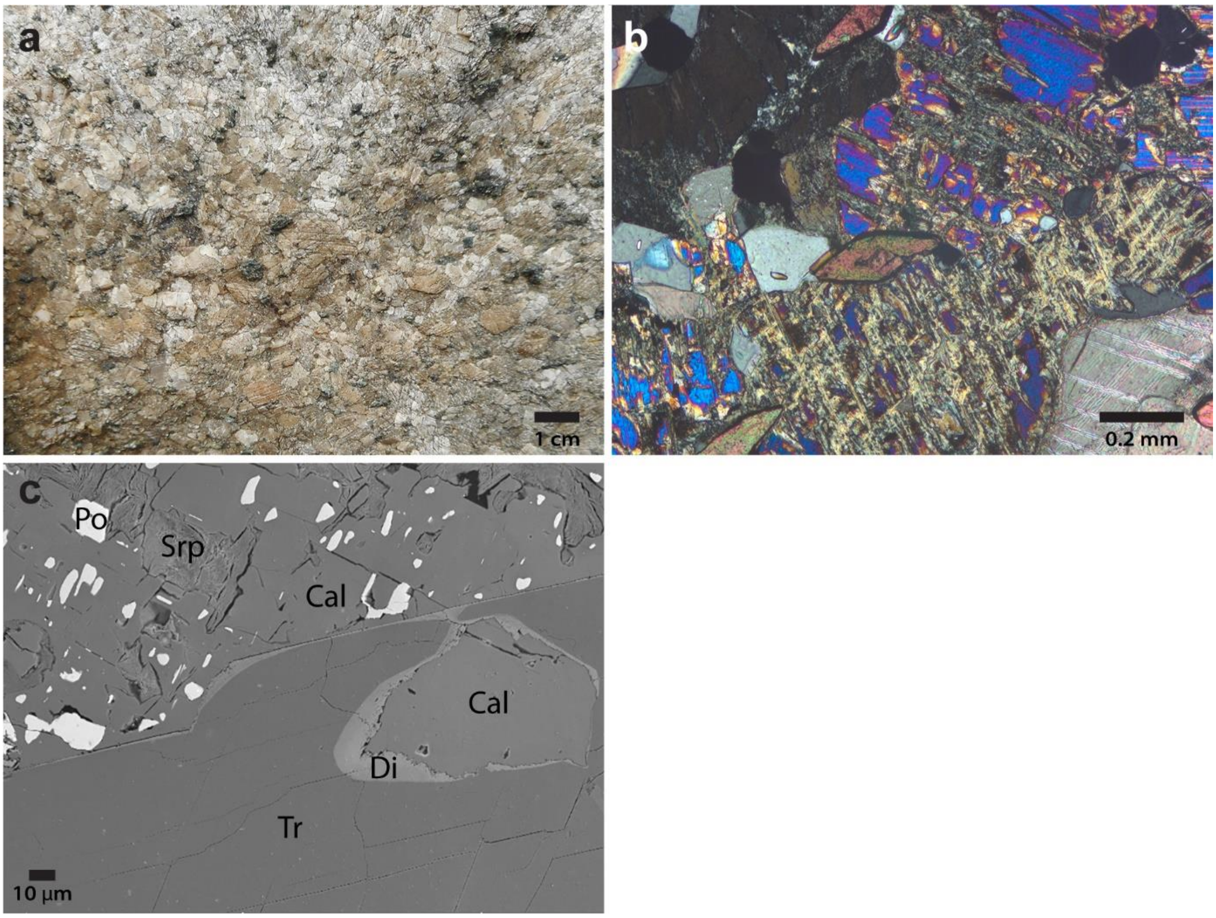

Figure 40. A. Coarse-grained marble with up to cm-sized crystals of calcite and isolated crystals of pyroxene (ALZ191006). **B.** Photomicrograph in xpl of a calcite marble with olivine (partially serpentinised), titanite as well as minor quartz and garnet. Sample ALZ190006A from drill core TUN003 (Boliden 1948), interval 62.44–64.73 m. **C.** SEM-BSE image of a mineralised marble (EDB190054), tremolite is altered to diopside along a c. 10 µm wide rim in contact with calcite. Pyrrhotite is disseminated within the calcite, serpentine is likely of retrograde metamorphic origin. Photos: Alexander Lewerentz.

Skarn occurs as layers within the metavolcanic and metasedimentary sequence, these likely represent carbonate-bearing or marble horizons that were later altered into skarn (Fig. 41a). The thickness of these layers or horizons seldom exceeds 1 m. They are generally inequigranular or porphyroblastic, with mainly garnet, pyroxene and amphibole as porphyroblasts. Garnet seem to occur in most skarns (Fig. 41b), whereas hedenbergite and grunerite seemingly only occur separately (Fig. 41c–f). Minor amounts of residual (?) carbonate is generally but not always present. Other minerals identified in thin section include biotite, quartz, apatite, diopside, antigorite, hisingerite, and feldspars (Appendices 3 & 4). Some of the skarns are magnetite-bearing and thus show very high magnetic susceptibility (up to c. 0.72 SI), whereas others are sulphide-bearing with mainly sphalerite and chalcopyrite.

Early-orogenic granitoids occur sparsely in the studied area and is only mapped within a fold structure west of Koppartorp (Fig. 36). These are inequigranular, fine- to medium-grained rocks that show foliated or migmatitic structures. Their composition is in field interpreted as granodioritic.

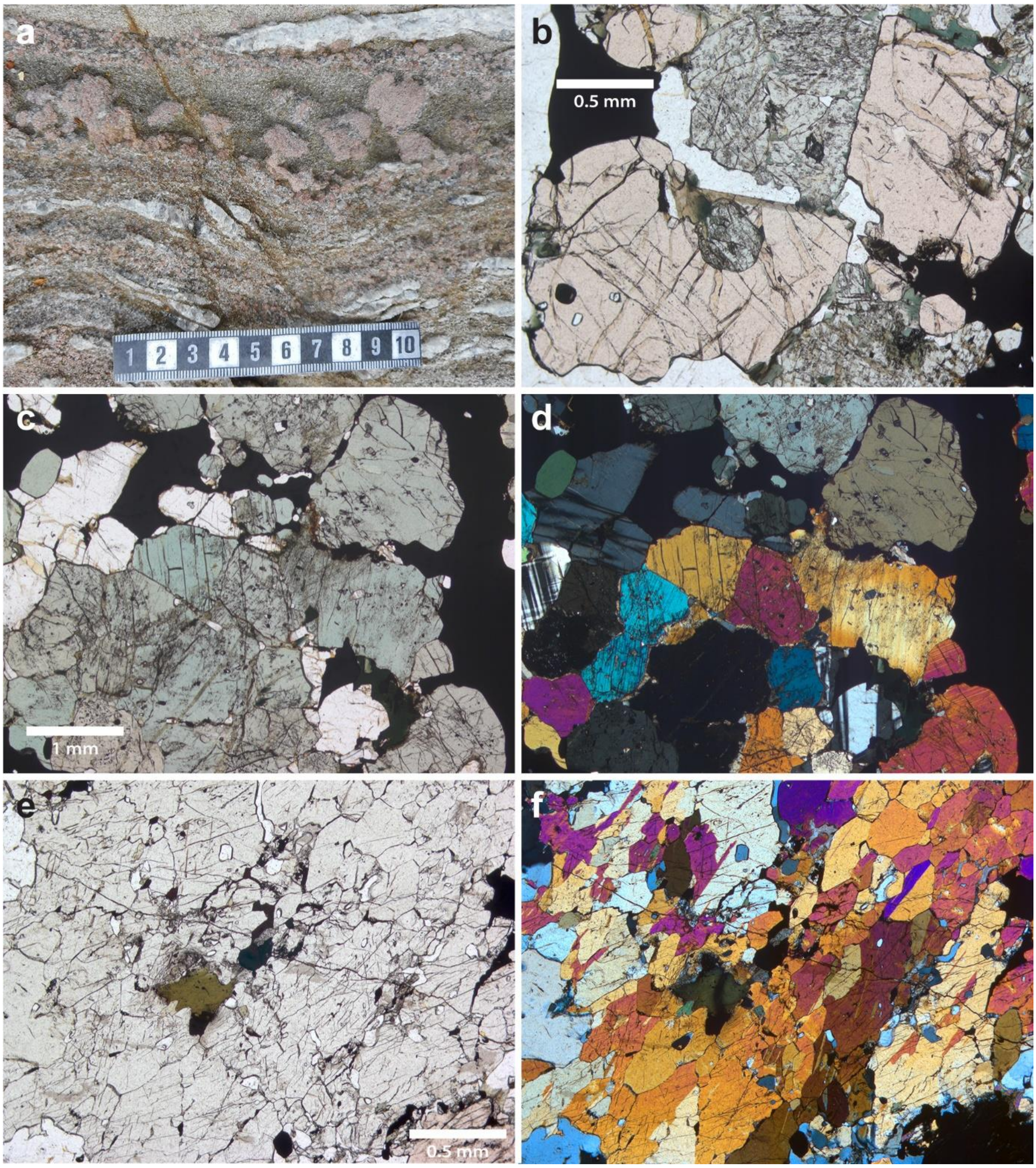

Figure 41. A. Field photograph of a skarn with up to cm-sized crystals of garnet. Boudinaged and folded quartz veins are parallel to the bedding/foliation (ALZ191040). **B.** Photomicrograph in ppl of skarn that to great part consists of garnet and clinopyroxene (ALZ190009A, drill core T6D1, BHP 1997, interval 138.70–140.45 m). **C.** Photomicrograph in ppl, and **D.** xpl, of skarn that is mainly comprised by hedenbergite (ALZ190008A, drill core T6D1, interval 60.00–60.75 m). **E.** Photomicrograph in ppl, and **F.** xpl, of skarn with abundant grunerite-cummingtonite (ALZ190011A, drill core T6D1, interval 162.35–163.55 m). Photos: Alexander Lewerentz.

Amphibolites locally occur as subordinate dykes or sills within the supracrustal rocks. They are fine-grained, generally equigranular, and show foliation or gneissose structures. At some outcrops the foliation is discordant to the orientation of the amphibolite (Fig. 42a), which favours the interpretation of dykes. At other outcrops foliation and amphibolite orientation are parallel, in which cases it is impossible to conclude whether the amphibolite originally was a sill or a dyke that was parallelized with the foliation by later tectonic shear.

Synorogenic granites occur within the supracrustal rocks and vary in scale from cm-sized veins to larger lenticular bodies that are tens to hundreds of metres across (Fig. 37). They are inequigranular, fine- to coarse-grained rocks that are mainly composed of quartz and K-feldspar (Fig. 42b). Small-scale veins are mostly parallel to the foliation or gneissosity of the surrounding rock, in larger bodies elongate K-feldspar crystals define a planar structure that is parallel to foliation or gneissosity. Both observations indicate active shear during emplacement, which is interpreted as evidence for formation from syn-orogenic, possibly localised melts.

Late- to post-orogenic granites occur throughout the area. They are massive, porphyritic rocks with phenocrysts of K-feldspar in a finely medium-grained matrix of mainly quartz and plagioclase (Fig. 42c). Minor recrystallisation indicates emplacement in the late stages of or shortly after the orogeny ended.

Pegmatite occurs as dykes that crosscut all tectonic structures (Fig. 42d). They are coarse-grained, show a massive texture, and are mainly comprised of K-feldspar, quartz, plagioclase with minor biotite and muscovite. The complete lack of deformation and recrystallisation strongly indicate post-orogenic formation.

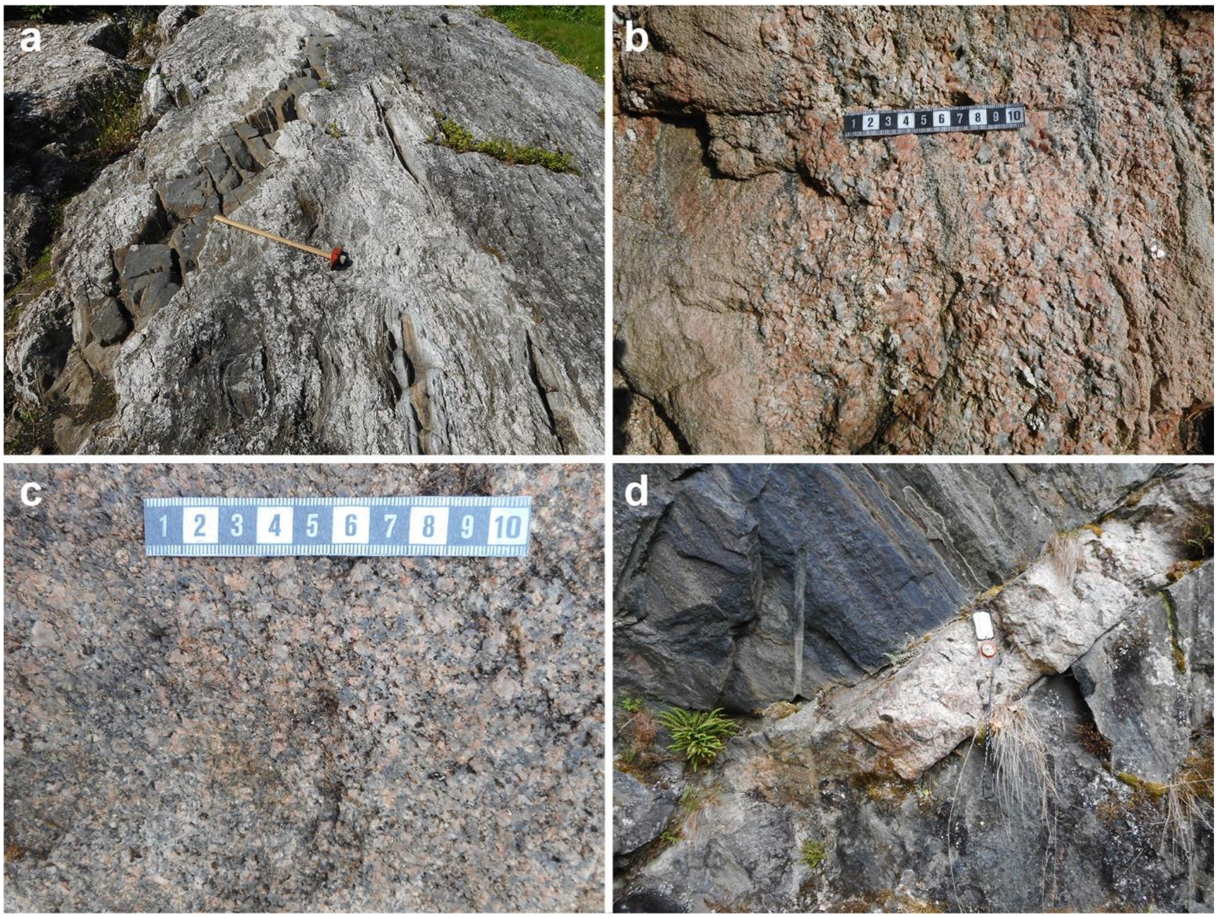

Figure 42A. Deformed, boudinaged, amphibolite sill or dyke, whose orientation is discordant to the gneissosity of the surrounding migmatised supracrustal rock (ALZ191018). Length of hammer is c. 0.5 m. **B.** Synorogenic granite with gneissosity parallel to the tectonic foliation (ALZ191007). **C.** Late- to post-orogenic, massive granite with phenocrysts of K-feldspar in a finely medium-grained matrix (ALZ191015). **D**. Undeformed, a few decimetres thick pegmatite dyke that cuts the foliation of the surrounding, magnetite-rich skarn. Compass as scale (ALZ191060). All photos: Alexander Lewerentz.

Description of investigated mineralisations

Several styles of mineralisations are present in the Tunaberg area, including iron and manganese ores, zinc ores, as well as copper and cobalt ores.

The copper-cobalt ores are hosted in a skarn-altered calcite marble. The sulphide mineralisation has partly overgrown an earlier skarnification process, with sulphide minerals forming veins, filling up fractures and occurring along grain boundaries (Fig. 43a). Some portion of the sulphide minerals are coeval with the skarn formation, as indicated by skarn and sulphide mineral intergrowths (Fig. 43b). The main ore mineral assemblage consists of pyrrhotite-cubanite-chalcopyrite, in which the main cobalt-bearing minerals are cobaltite and skutterudite. Cubanite-chalcopyrite intergrowths commonly have inclusions of Co-pentlandite and exsolutions of galena. The ore assemblage is complex, with sphalerite, magnetite, graphite, and mackinawite, and many more unidentified metal-bearing minerals occurring as inclusions and exsolutions (Fig. 43c–d). Pyrrhotite, magnetite, sphalerite, and chalcopyrite all occur as individual inclusions in other ore minerals, but also as intergrowths and overgrowth of each other, which indicates several phases of mineralisation or later remobilisation. Generally, some precipitation of pyrrhotite and magnetite seems to occur before the main copper-cobalt mineralising event. Pyrrhotite locally occurs as a nucleus in magnetite, in some cases strongly altered with birds-eye textures. However, veins of intergrown magnetite and chalcopyrite, as well as intergrowths of later pyrrhotite with cubanite and chalcopyrite are also common (Fig. 43d–e).

The occurrence of graphite, relatively little pyrite, in contrast with abundant pyrrhotite, and cubanite point to high temperature and reducing conditions during ore formation. Apatite occurs intergrown with chalcopyrite and fluorite. A more detailed description of the ore mineralogy and further details about the chemistry and temperature of the skarn and ore forming fluids are given in Dobbe (1994b).

The lead-zinc ores in the Tunaberg area are commonly dominated by massive bands of sphalerite with inclusions of pyrrhotite and magnetite and cemented by galena (Fig. 44 a–c). Minor inclusions of chalcopyrite, and breithauptite, as well as several unidentified ore minerals have also been observed. Sphalerite can also contain inclusions or aggregates of silicate minerals such as quartz, biotite and K-feldspar, which in turn can include graphite and pyrite. Disseminated sulphide minerals occur both as inclusions in quartz, garnet, pyroxene, and amphibole and as larger subhedral crystals together and with inclusions of these skarn minerals, which points to precipitation of ore minerals during skarn formation. However, pyrrhotite and sphalerite also occur along grain boundaries, as fracture filling and in quartz veins, which suggests that ore formation continued after skarn formation or that there was a later remobilisation of ore minerals. This is also evident by the complex paragenetic sequence: pyrrhotite and chalcopyrite occurs as inclusions in sphalerite that is surrounded by pyrrhotite overgrown by a rim of sphalerite. Given the migmatitic, granulite-facies metamorphic conditions, sulphide melting is likely to have occurred during metamorphism, which possibly enabled melt-assisted sulphide redistribution, at least on a local scale.

Sulphide minerals, most notably pyrrhotite, shows localised strong alteration textures. The degree of alteration varies largely even within individual samples, which suggests several generations of sulphide mineralisation or, alternatively, a channelised fluid infiltration that left part of the rock untouched. An example of the latter is retrograde metamorphic fluid flow.

▶ **Figure 43.** Photomicrographs of **A.** ore minerals (mostly chalcopyrite-cubanite) that form a vein network that follows grain boundaries and fills up fractures in skarn-altered calcite marble (EDB190070B), **B.** graphite, and cubanite-chalcopyrite intergrown with a calcsilicate mineral in calcite marble (EDB190054A), **C.** complex ore mineral assemblage of cubanite-chalcopyrite with inclusions of sphalerite, covellite, pyrrhotite, and several unidentified minerals (EDB190054A), **D.** intergrowth of cubanite and pyrrhotite with inclusions of Co-pentlandite and mackinawite (Mcw) along the interface (EDB190069A), **E.** vein with intergrown chalcopyrite and magnetite (EDB190067A), and **F.** altered early pyrrhotite overgrown by chalcopyrite, cobaltite (Cob) occurs intergrown with skutterudite (Skut) (EDB190070B). Photos: Edine Bakker. SEM-BSE-images of **G.** cobaltite and altered pyrrhotite surrounded by chalcopyrite, hosted by a calcite-diopside-antigorite skarn assemblage, and **H.** skutterudite and cobaltite, note the small skutterudite inclusion within the cobaltite, surrounded by mainly diopside (EDB190070B). Photos: Alexander Lewerentz.

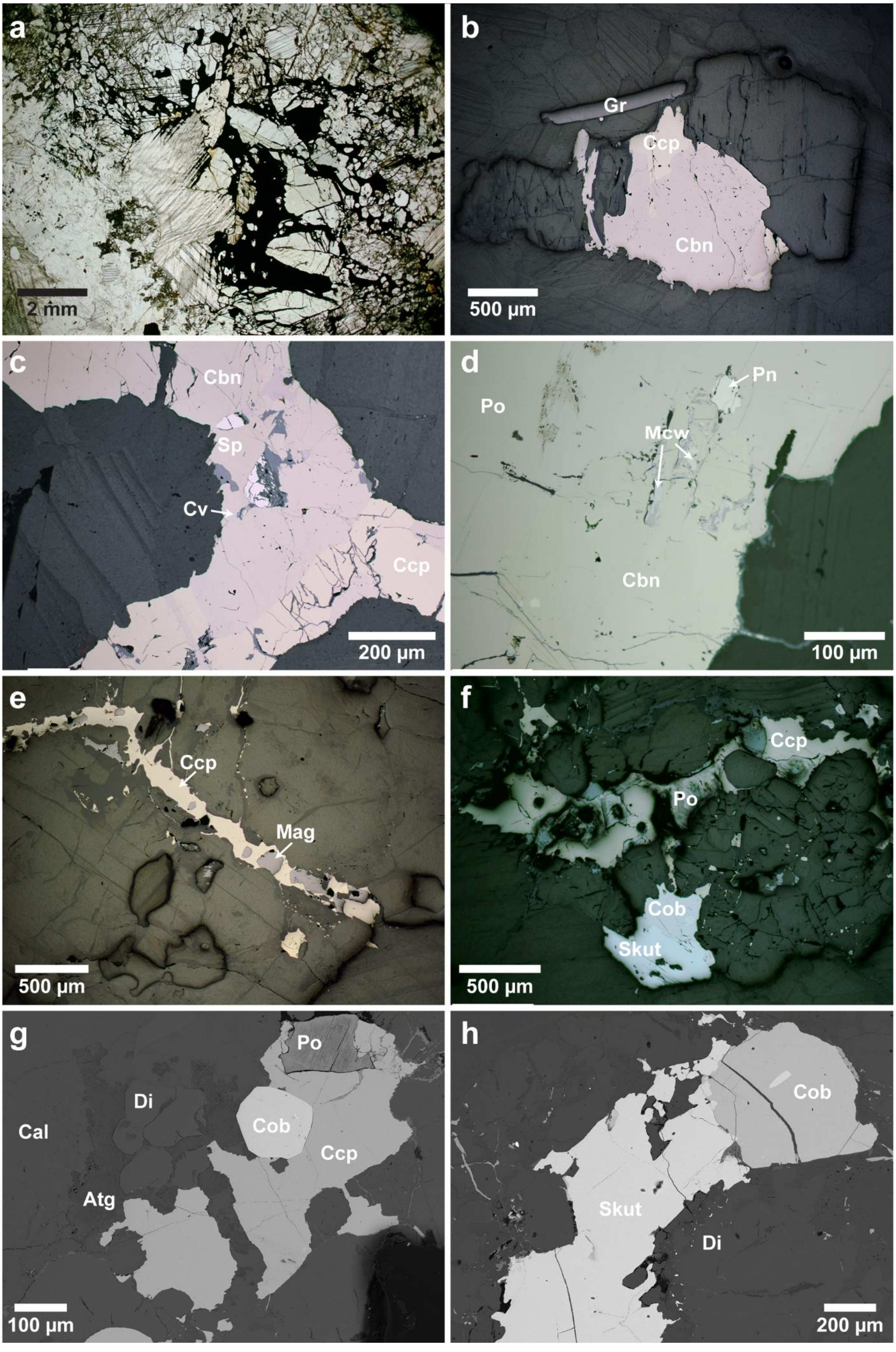
a
2 mm
b
Gr
Ccp
Cbn
500 µm
c
Cbn
Sp
Cv
Ccp
200 µm
d
Po
Pn
Mcw
Cbn
100 µm
e
Ccp
Mag
500 µm
f
Ccp
Po
Cob
Skut
500 µm
g
Po
Di
Cal
Cob
Ccp
Atg
100 µm
h
Cob
Skut
Di
200 µm

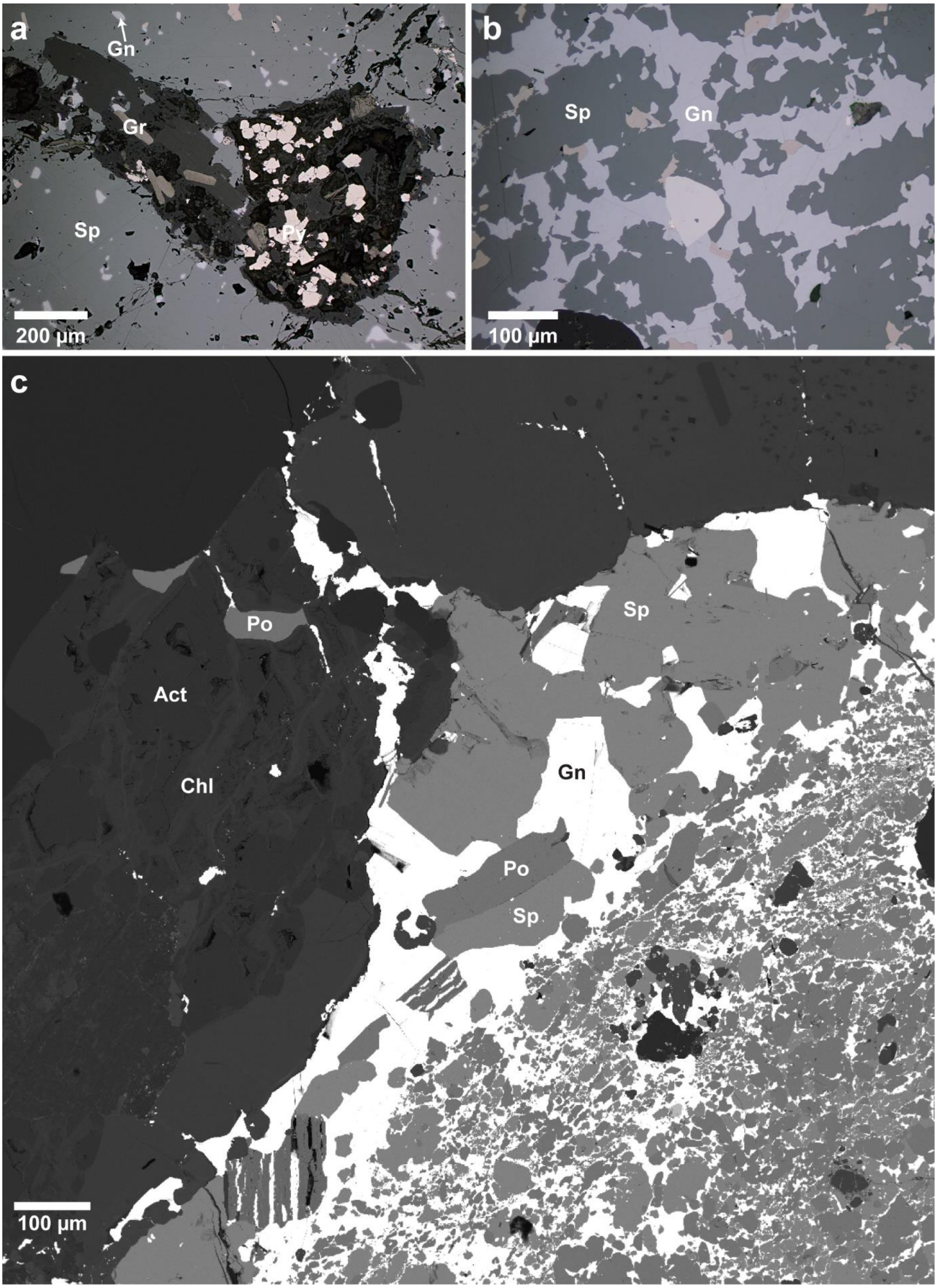

Figure 44. A. Reflected light photomicrograph of massive sphalerite with inclusions of galena and a large inclusion of silicate minerals, pyrite and graphite, and **B.** massive galena and sphalerite with inclusion of unidentified ore minerals (ALZ190049A). Photos: Edine Bakker. **C.** SEM-BSE image of massive sphalerite and galena intergrown with pyrrhotite (ALZ190005A, drill core TUN003 (Boliden 1948), interval 62.04–62.44 m). Photo: Alexander Lewerentz.

Hyalophane is an alteration mineral, which texturally seems coeval with growth of galena and pyrrhotite. Zoisite occurs as inclusions in and intergrown with sphalerite and pyrrhotite.

One sample of an iron skarn mineralisation was examined in thin section. Magnetite overgrows poikiloblasts of metamorphic biotite and hornblende and small grains of magnetite grow on the edges of sphalerite, which suggests that this type of mineralisation formed later than the above described mineralisations.

Geophysical survey

Aeromagnetics

In the 1970 airborne geophysical survey, measurements of the total field magnetic intensity and natural gamma radiation were made with a sampling interval of c. 40 m at 30 m nominal altitude and with 200 m separation. The precision of the magnetometer was c. 5 nT and VLF was not measured at the time. Figure 45 shows the residual magnetic anomaly map, i.e. the difference between the geomagnetic field and a 1 km upward continuation of the same, where the influence of deeper sources is reduced to accentuate the response from geological formations closer to the surface.

The sulphide mineralisation at Koppartorp in the centre of the focus area, lie within a magnetic low area connected to a regional deformation zone that strikes through the study area (Fig. 45). The old airborne data give little information that can be linked to the near-surface geological formations and structures with which the Koppartorp mineralisation is associated.

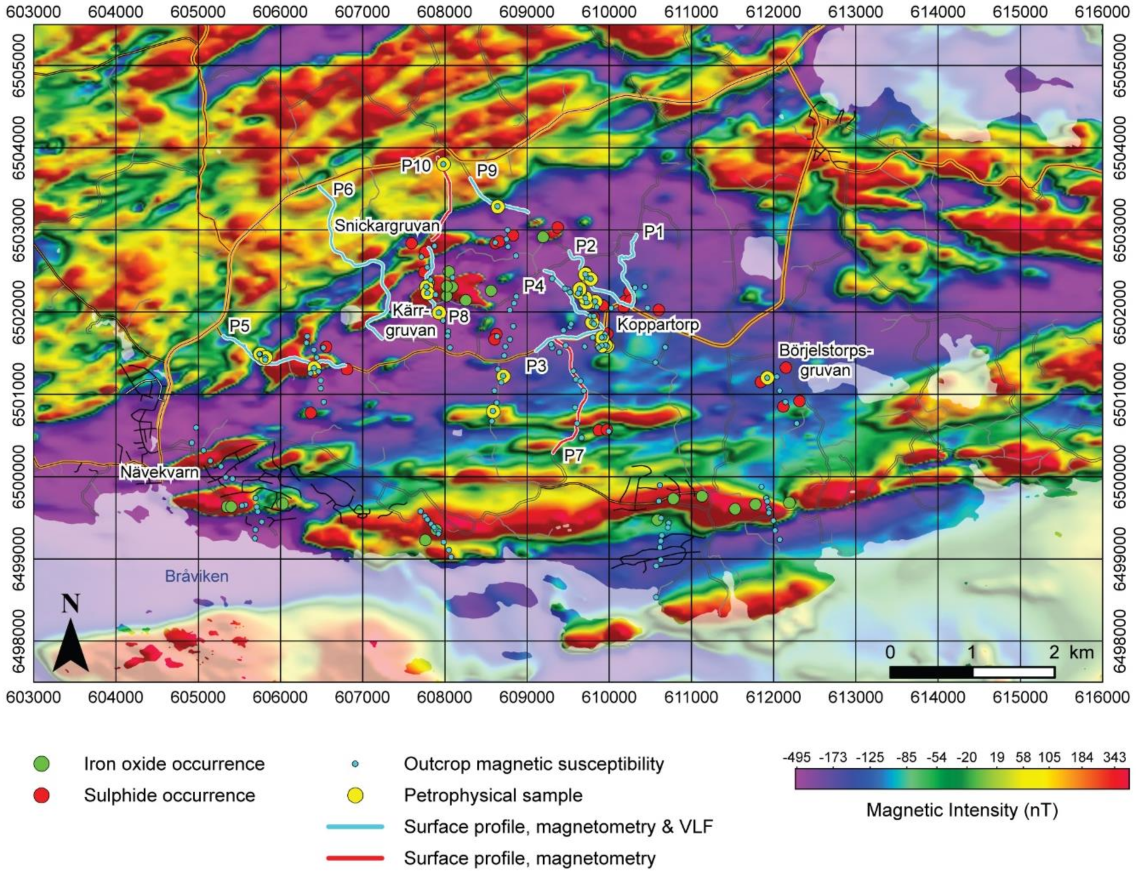

Figure 45. Residual magnetic field anomaly based on aeromagnetic measurements from 1970, calculated as the difference between the total magnetic field intensity after reduction to pole and the 1 km upward continuation of the same. Positive anomalies (red colours) typically indicate the presence of ferro- and ferrimagnetic minerals among which magnetite and pyrrhotite are known from the mineralised areas.

This low magnetic area is surrounded by bands of positive magnetic anomalies in the north, west and south where both magnetite and sulphide mineralisation are hosted in carbonate or calc-silicate rocks within the felsic metavolcanic rocks, e.g. those at Kärrgruvan, Snickargruvan and Mormorsgruvan. A distinct transition is seen to the northwest, separating the Tunaberg area from the adjacent area where the magnetic response is generally higher with a banded anomaly pattern oriented southwest–northeast. Tunaberg can thus be seen to have had a complicated tectonic history as part of the major deformation system that runs through the region.

Gravity

In May 2019, SGU acquired 273 new gravity measurements in Tunaberg and its immediate surroundings to complement the existing sparse dataset. In addition to achieving a denser and more uniform spatial distribution, with an average measurement separation of c. 1 km compared to the previous 1.5–3 km, profiles with a point separation of as low as c. 100 m were acquired in the vicinity of Koppartorp.

Measurements were made with a Scintrex CG-5 gravimeter and GNSS-equipment from Topcon was used for elevation determination. Geosoft Oasis Montaj was used for data reduction and processing and the final terrain-corrected bouguer anomaly is stored in the SGU database for gravity data. The map in Figure 46 shows the residual gravity anomaly map after removal of a regional trend to reduce the influence of regional and deep sources, i.e. the difference between the Bouguer anomaly and a 3 km upward continuation of the same.

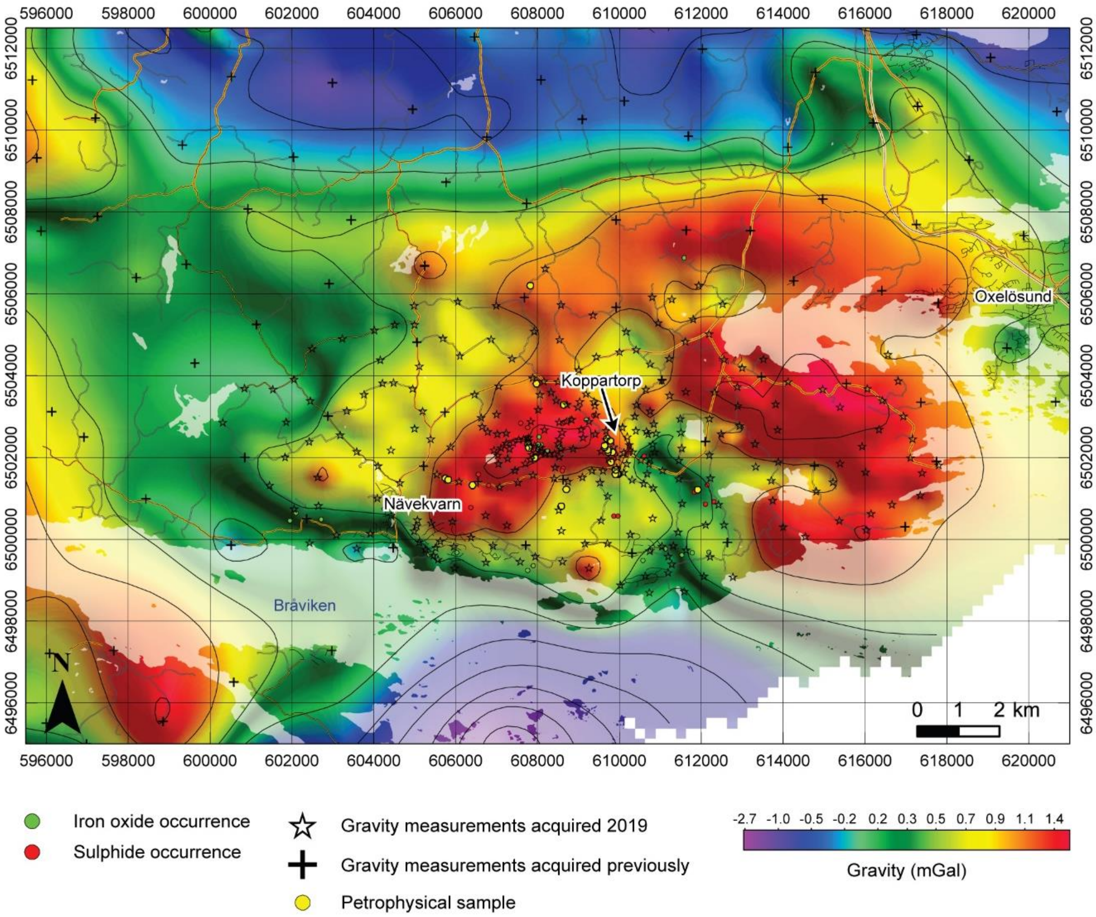

Figure 46. Residual gravity anomaly map based on gravity data acquired in 2019 and previous work, calculated as the difference between the Bouguer anomaly and a 3 km upward continuation of the same. Contour lines represent isolines in the residual gravity anomaly drawn at 0.5 mGal interval. In general, mafic bedrock formations or major mineralised zones give rise to positive gravity anomalies, whereas felsic bedrock generates negative gravity anomalies.

The gravity data shows a regional scale fold pattern similar to that seen in the magnetic data, albeit with lower resolution. A local positive gravity anomaly in the Kärrgruvan area indicates a slight mass surplus associated with the local iron-oxide mineralisation. Mass surplus is also suggested northeast and east of the area. In the central part of the study area, east of Koppartorp, a gravity low extends southwards to gravity lows in Bråviken. Data is very sparse northwest of the Tunaberg area, but the gravity appears less variable and successively decreases towards north.

3D inversion of the magnetic and gravity data, which have relatively low resolution and low amplitude anomalies, does not provide much insight on the geometry of subsurface geological structures and formations in this tectonically deformed area.

Surface profiling

During June 2019, high resolution surface measurements of the geomagnetic field intensity and electromagnetic field in the VLF-range were done along ten profiles (Fig. 45). The equipment used was the GEM Systems GSMV-19 combined magnetometer and triple-frequency VLF-sensor with GPS-positioning.

The Koppartorp area is full of infrastructure that acts as sources of noise, especially for the VLF equipment. Additionally, due to the lack of airborne VLF data, the surface VLF data cannot be tied to structures or formations in the regional tectonic setting. The geophysical surface profile data have therefore, at this point, not been further modelled or interpreted.

Petrophysics

During the 2019 field campaign, magnetic susceptibility was measured on a total of 194 bedrock outcrops and 48 bedrock samples were collected for petrophysical analysis of primarily density and magnetic properties. Sample and measurement positions were recorded using a handheld GPS. Petrophysical measurements and analysis were conducted at SGU and results are presented in Figures 47 and 48, with full details listed in Appendix 6.

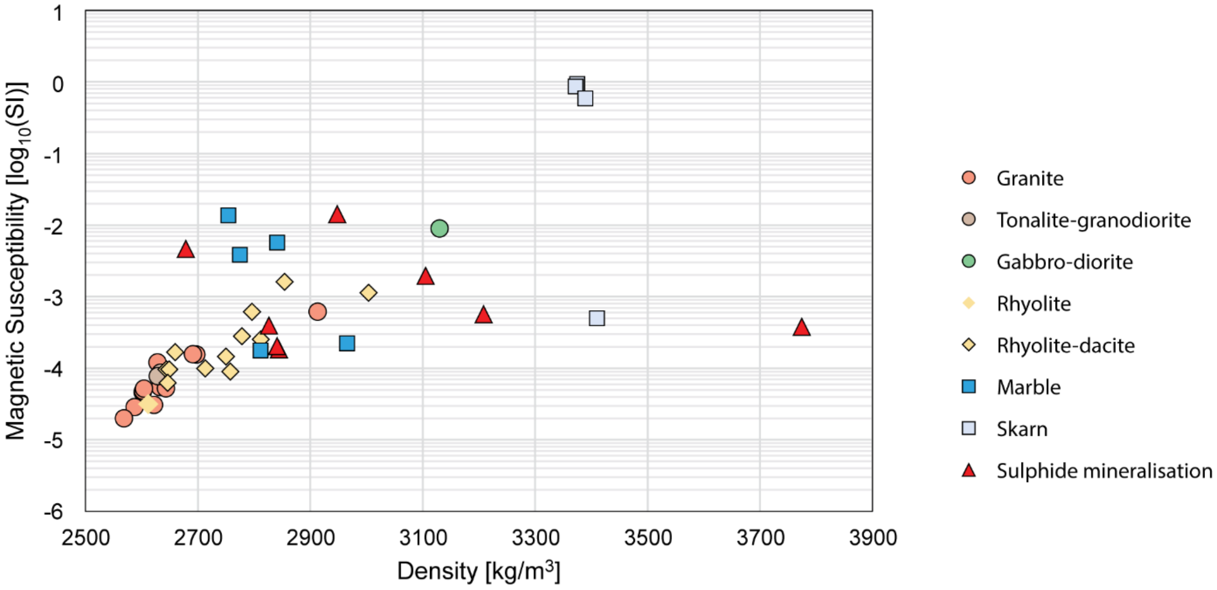

Figure 47. Distribution of density versus magnetic susceptibility measured on samples from the Tunaberg area. The three samples with the highest magnetic susceptibility are magnetite-rich skarn from waste piles at Kärrgruvan.

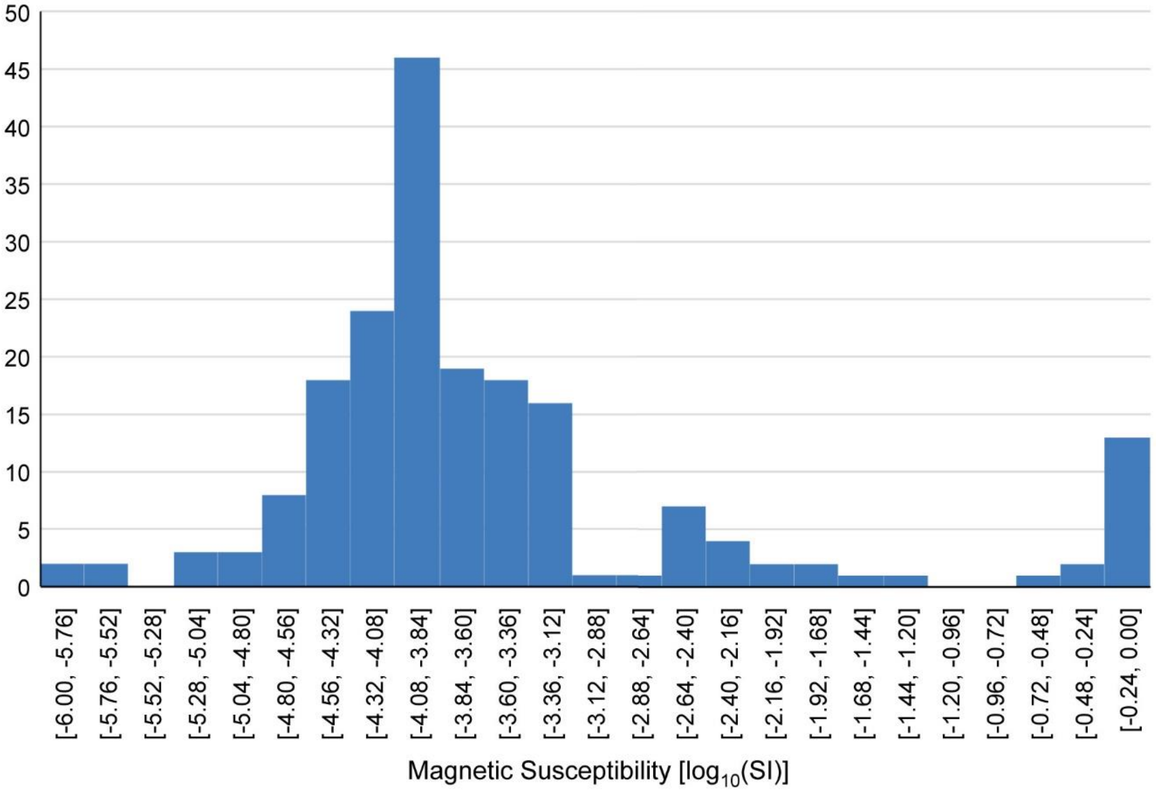

Figure 48. Distribution of magnetic susceptibility from 194 outcrop measurements in the Tunaberg area.

Lithogeochemistry

The chemical composition was determined for 56 samples from outcrops, drill cores and waste piles. All analyses are available in SGU's lithogeochemistry database, and also accessible through SGU's map viewer Bergartskemi (in Swedish). These are plotted below in different diagrams and in applicable cases compared to 24 previous analyses from the area (Lundström 1974).

Supracrustal and metavolcanic rocks are classified as andesites, dacites or rhyolites based on their alkali versus silica content (Fig. 49a). The supracrustal rocks of possible sedimentary origin, as well as some of the mineralised volcanic rocks, are to some extent more alkalic than the rocks interpreted of volcanic origin, with some samples plotting within the trachyte series. Assessment of Na- and K-alteration shows that almost all volcanic and supracrustal rocks lie outside the igneous spectrum and are mildly to extensively K-altered, especially so the supracrustal rocks (Fig. 49b). Trace-element based classification, ideally unaffected by hydrothermal alteration processes, shows that almost all samples, volcanic and supracrustal, mineralised and barren, fall within a normal andesite-rhyolite volcanic series (Fig. 49c).

Amphibolite samples have the chemical composition equivalent of gabbro, which is expected from metabasalts (Fig. 49d). Early-orogenic granitoids in this study are classified as granites (Fig. 49d), whereas those of Lundström (1974) fall within the diorite and tonalite field. It is, however, not unexpected to see some variations within the area, especially since this study purposely targeted sites previously not analysed. Late- to post-orogenic granitoids are all chemically classified as granites (Fig. 49d), including samples from both this study and Lundström (1974).

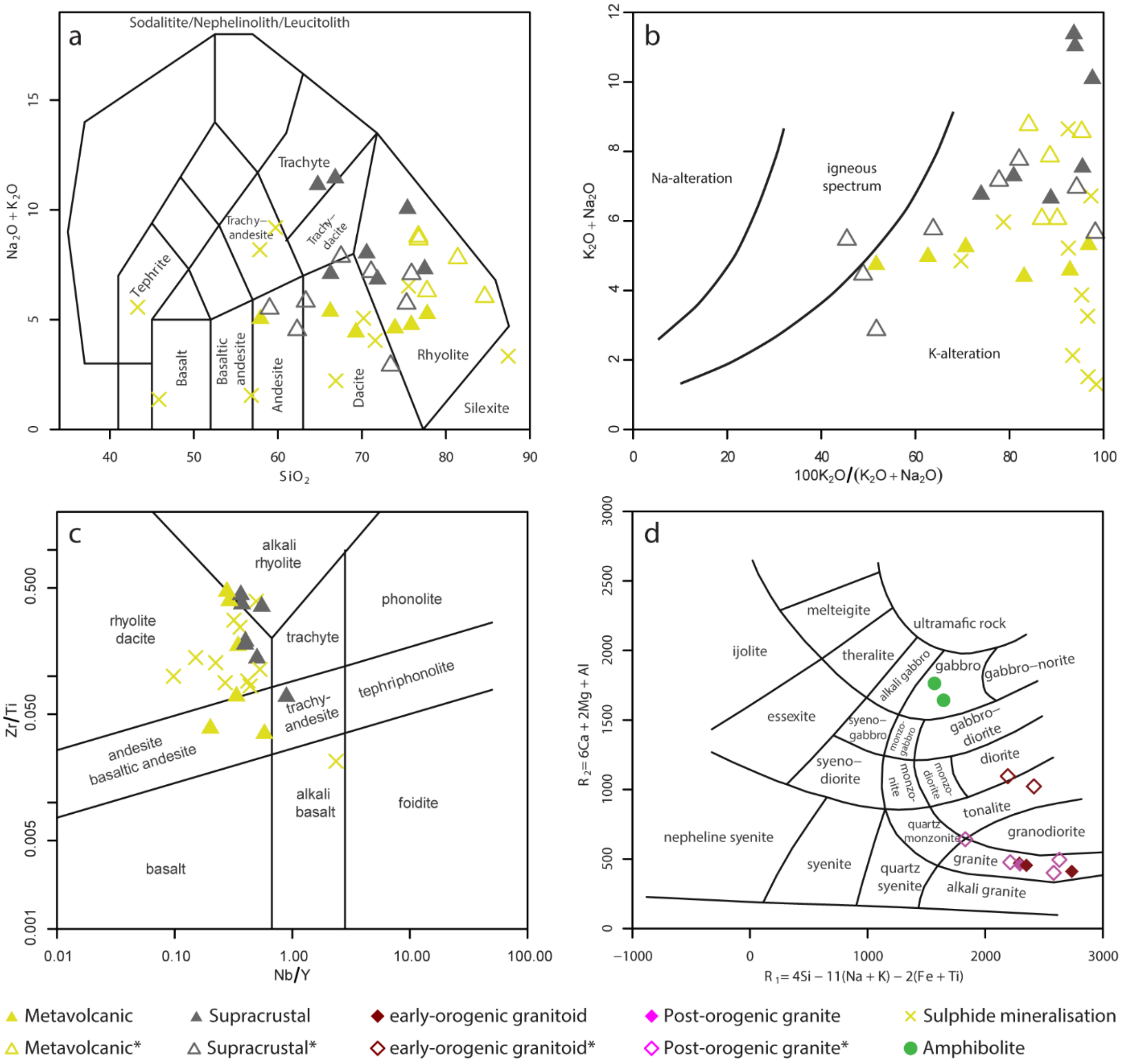

Figure 49. Classification of metavolcanic rocks with respect to alkali and silica content (TAS; after Middlemost 1994). **B.** Evaluation of the degree of hydrothermal alteration shows that most metavolcanic and supracrustal rocks are altered by extensive K-alteration (after Hughes 1973). **C.** Classification based on immobile elements, generally considered unaffected by secondary alteration, shows that most volcanic and supracrustal rocks fall within an andesite-rhyolite series. (Pearce 1996). **D.** Classification diagram for intrusive rocks (after De la Roche et.al. 1980). *Unfilled symbols are data from Lundström (1974).

Geotectonic classification for volcanic rocks as defined by Schandl & Gorton (2002) utilises four different trace element relationships for assessment of the tectonic setting for volcanism. These indicate with very few exceptions that the Tunaberg metavolcanic and supracrustal rocks were formed at an active continental margin (Fig. 50). The positions of mineralised samples in these diagrams should be treated with cation, one or several of the used trace-element components may have been partially affected by the mineralising fluids and other metamorphic overprinting.

Trace-element distributions are plotted in Figure 51. Volcanic and supracrustal rocks as groups have very similar compositions, which may indicate that the supracrustal rocks are of volcanic origin or mainly composed of reworked volcanic material. Both trace element and REE distributions follow the regional pattern for volcanic rocks in Bergslagen (cf. Stephens et al. 2009), with negative anomalies for Nb, Sr, P, and Ti. The Nb anomaly indicates formation at an active continental margin (Brown et al. 1984), whereas the others likely reflect magmatic fractionation of plagioclase, apatite and some Ti-bearing mineral. Fractionation of plagioclase would also explain the negative Eu anomaly.

Amphibolites, early-orogenic granitoids and the late- to post-orogenic granite show similar trace-element distributions. The amphibolites contrast from the other rocks by the presence of a negative anomaly for Th and the lack of an anomaly for P. They also have a much flatter REE trend and lack an anomaly for Eu. One of the early-orogenic granitoids shows a very different REE distribution compared to the others: the Eu anomaly is positive rather than negative and the rock has suffered a factor 10 depletion of all other REE. This may be explained by alteration by a fluid that mobilised all REE^{3+} but left the plagioclase-bound Eu^{2+} untouched.

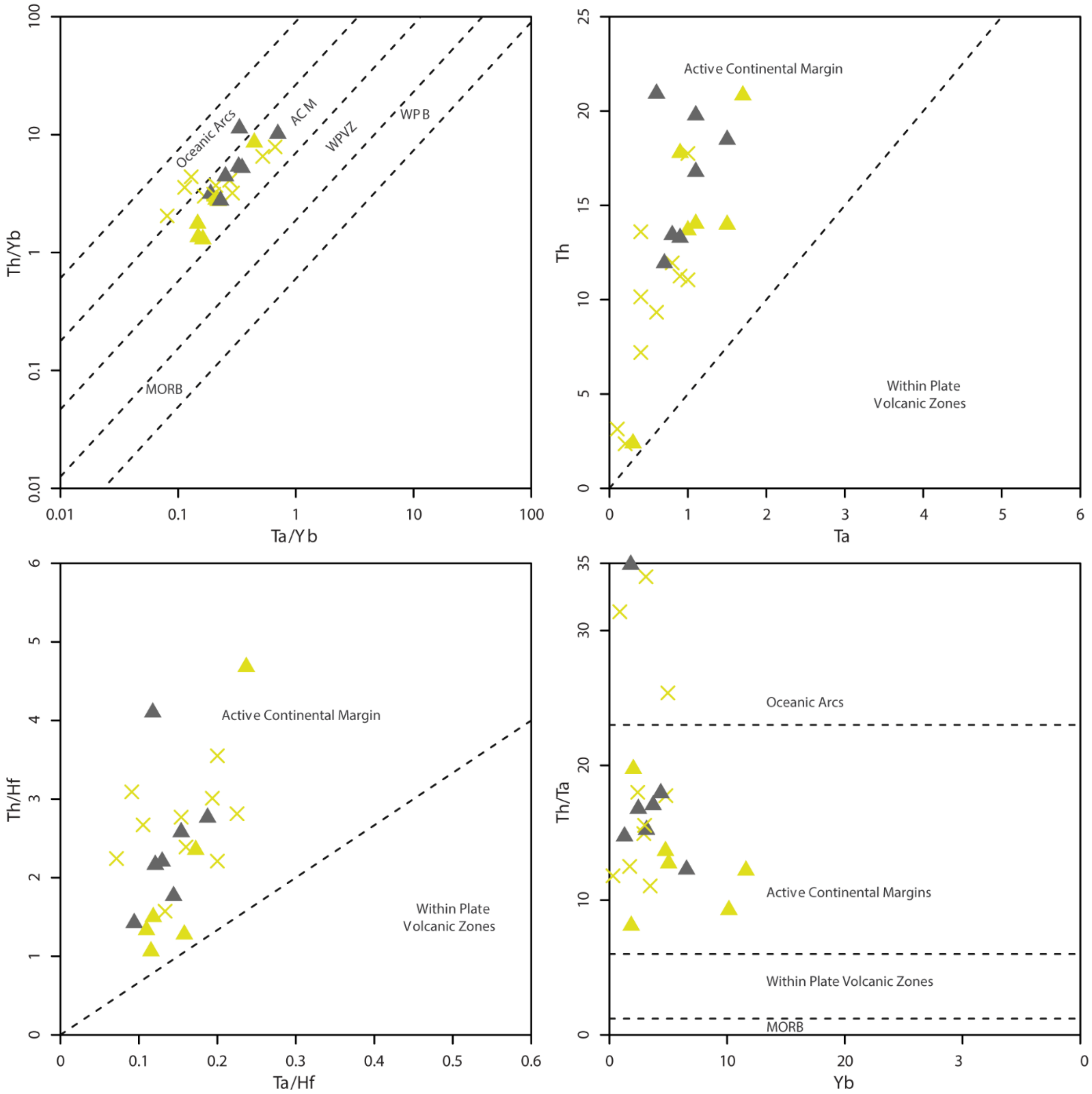

Figure 50. Geotectonic classification of volcanic rocks based on trace elements according to Schandl & Gorton (2002) indicate that the metavolcanic rocks of the Tunaberg area were formed along an active continental margin. See Figure 49 for legend.

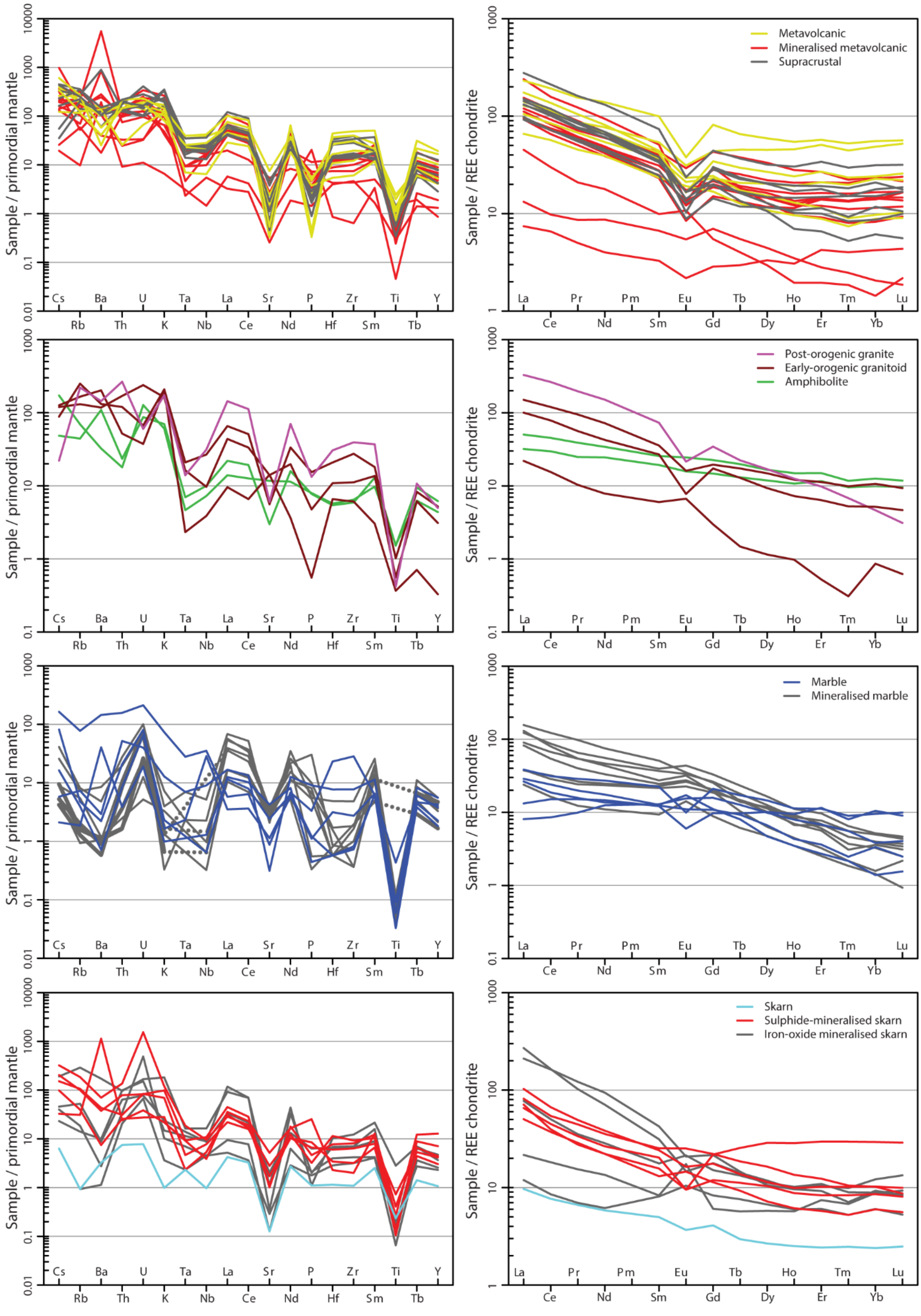

Figure 51. Trace-element distributions for the different rock types observed in the Tunaberg area, as normalised to primordial mantle (Wood et al. 1979) and REE chondrite (Boynton 1984), respectively. Some of the marble samples had Ta and Ti concentrations below the detection limit, as indicated by dashed lines.

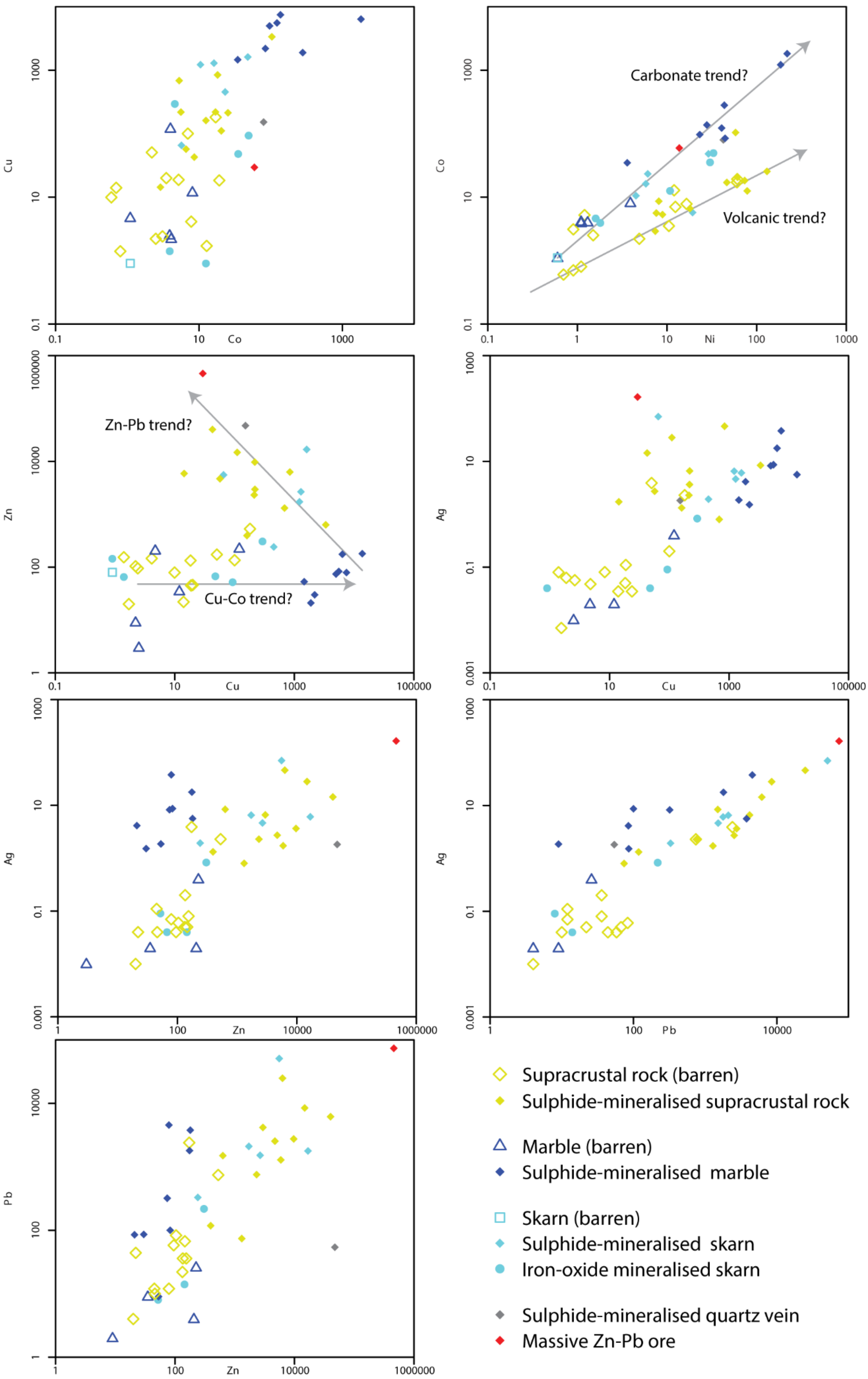

Figure 52. Bivariate plots for selected metals of mineralisations with possible trend interpretations.

Marble generally shows a similar pattern with negative anomalies for elements in feldspar (Rb, Ba, K, and Sr), elements in zircon (Hf and Zr), i.e. silicate minerals that should not be major constituents of limestone or marble. Titanium concentrations are low in seawater, very low Ti contents are therefore expected in limestone and marble. REE trends are either almost horizontal, or show a kink due to depletion of HREE, with minor positive or negative Eu anomalies. It is unknown whether the discrepant REE trends represent different primary depositional conditions or later mobilisation.

Skarn samples show similar trace-element distributions to those of marble. One sample is relatively enriched in HREE, which are likely hosted by the large abundance of garnet observed in thin section. Apparent enrichment and depletion in LREE might reflect the abundance of epidote and pyroxene in the skarn mineral assemblage.

Bivariate plots of selected metals of mineralisations show elevated concentrations in many samples (Fig. 52). Mineralised marbles are especially enriched in Cu ≤1.37% and Co ≤0.18%, whereas metavolcanic rocks are enriched in Zn ≤4.74% and Pb ≤5.09%. A sample of massive Zn-Pb ore collected from the waste piles of Börjelstorpsgruvan contained 45.9% Zn, 7.38% Pb, 0.14% Cd, and 165 ppm Ag (ALZ191049A; Fig. 44a–b). One of the drill core samples contained 2.16 ppm Au, in addition to elevated concentrations of Pb, Zn, and Ba (ALZ190005A; drill core TUN003, drilled by Boliden in 1948, interval 62.04–62.44 m).

Cobalt is as expected from the observed assemblages fairly well-correlated with Cu. A good correlation is also seen between Co and Ni, where the metavolcanic and carbonate samples, with a few exceptions, seem to follow two separate trends. For all barren samples and mineralised marbles, Cu and Zn are uncorrelated, whereas sulphide-mineralised volcanic rocks and skarns possibly are inversely correlated. Silver is fairly well-correlated with both Cu and Zn, but in both cases a significant number of exceptions are present, i.e. Ag-enriched but Zn-poor marbles or Cu-poor metavolcanics, respectively. Zinc and Pb show good correlation for the metavolcanic rocks and the skarns, but poorer correlation for the marbles. Lead, on the other hand, shows a rather good correlation with Ag for all samples, which indicates that Ag is hosted by galena.

Ore-genetic discussion

Three main types of mineralisations are present in the Tunaberg area: (1) marble- and skarn-hosted Cu-Co mineralisations, (2) volcanic or supracrustal- and skarn-hosted Zn-Pb mineralisations, and (3) skarn-hosted iron-oxide deposit. As described above (Fig. 43, 44), the textural and structural relationship between these mineralisation types is not straight forward, and they also show ample evidence of metamorphic recrystallisation and possibly also remobilisation. The relationship between Zn and Cu (Fig. 52) indicate some zonation within the mineralisations, where Cu-Co-rich samples may represent the more proximal parts of the deposit, with respect to distance from the centre of the hydrothermal cell and the assumption that it is stationary, the Zn-Pb-rich samples the more distal parts, and the remainder of the mineralised samples somewhere in between. Relocation of the hydrothermal cell during the formation of the mineralisation would also explain this kind of zonation.

Most mineralised metavolcanic rocks show rather distinct positive Ba anomalies (Fig. 51). Enrichment in comparison to unmineralized samples possibly reflects addition of Ba by fluids to allow formation of baryte ($BaSO_4$), witherite ($BaCO_3$) or other major Ba-bearing minerals as part of the mineralising processes. The richest sample contains 4.66 wt% BaO, which is equivalent of 7.09 wt% $BaSO_4$ if all Ba is assigned to baryte. The occurrence of hyalophane (Ba-rich K-feldspar) within the mineralisation provides further evidence towards a Ba-rich mineralising fluid, and intergrowths of sulphides and fluorite suggest they were also F-rich.

Rare-earth element concentrations are on average lower in mineralised metavolcanic rocks compared to their unmineralised equivalents, and in a few examples quite extremely depleted. This points towards mobilisation of REE by the mineralising fluids, which speculatively could be the source for REE enrichment in some of the iron-oxide mineralised skarns.

Marble samples from Tunaberg show a distinct fractionation trend between Co and Mn (Fig. 53). A similar trend is described for marbles from Zinkgruvan (Jansson et al. 2018), and for marbles from Håkansboda (Nils Jansson, pers.comm.). For Zinkgruvan, Jansson et al. (2018) use this trend as an argument to differentiate that the deposit is of SAS type (stratiform ash-siltstone-hosted sea floor deposit) rather than of SVALS type (stratabound volcanic-associated limestone-skarn sub-sea floor replacement deposit). The samples from Tunaberg conform very well to this trend, which indicates that the Cu-Co mineralisations of Tunaberg also are of SAS type. The fact that Co and Mn distributions are similar for marbles from three geographically separated areas may speculatively be interpreted as the existence of a general trend for SAS-mineralised carbonate rocks in the Bergslagen province. The exact processes behind such a trend remains unknown; however, likely important parameters are the pH, temperature, composition, redox state and salinity of the ore-forming hydrothermal fluids.

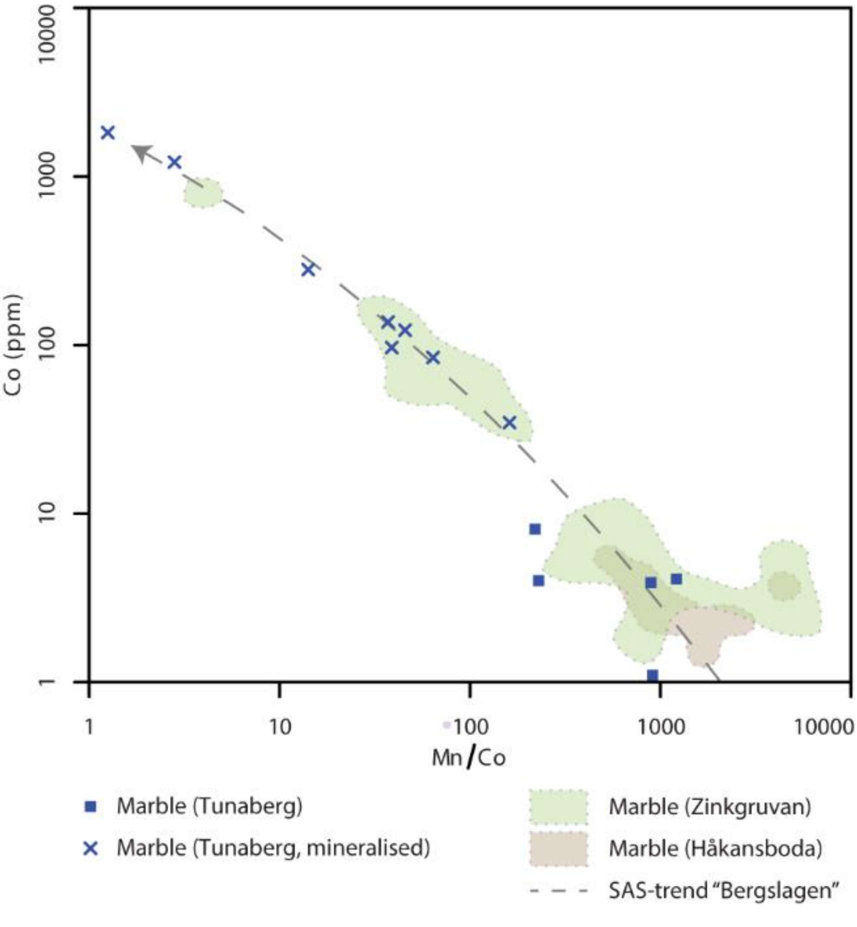

Figure 53. Plot of Co vs. Mn/Co in marble samples from Tunaberg. Contours of analogous data from Zinkgruvan (Jansson et al. 2018) and Håkansboda (Nils Jansson, pers. comm.) are shown for comparison. Zinkgruvan, Håkansboda and Tunaberg all follow a common trend, possibly a general trend for SAS-type mineralised carbonate rocks in the Bergslagen Ore Province (cf. "Zinkgruvan trend" in Jansson et al. 2018).

REFERENCES

Aleinikoff, J.N., Wintsch, R.P., Fanning, C.M. & Dorais, M.J., 2002: U–Pb geochronology of zircon and polygenetic titanite from the Glastonbury Complex, Connecticut, USA: an integrated SEM, EMPA, TIMS, and SHRIMP study. *Chemical Geology 188*, 124–147.

Antal Lundin, I., Claeson, D. & Sukotjo, S., 2006: Beskrivning till bergkvalitetskartan Nyköpings kommun. *Sveriges geologiska undersökning K48*, 18 pp.

Berzelius, J.J., 1819: *Nouveau Système de Minéralogie*. Chez Méquignon-Marvis, Paris, pp. 269–270.

BHP, 1997: Borrhålsprotokoll, T6D1, Lagarbo. 5 pp.

Blomberg, A. & Holm, G., 1902: Geologisk beskrifning öfver Nerike och Karlskoga bergslag samt Fellingsbro härad. *Sveriges geologiska undersökning Ca 2*, 124 pp.

Bolidens gruvaktiebolag, 1948: Provtagningsprotokoll, Tunaberg Nr. 3, Hultebobasen. 3 pp.

Boynton, W.V., 1984: Cosmochemistry of the rare earth elements; meteorite studies. In: P. Henderson (ed.): *Rare earth element geochemistry*. Elsevier, Amsterdam, pp. 63–114.

Brown, G.C., Thorpe, R.S. & Webb, P.C., 1984: The geochemical characteristics of granitoids in contrasting arcs and comments on magma sources. *Journal of the Geological Society, London 141*, 413−426.

Burgath, K.-P., von Rad, U., van der Linden, W., Block, M., Khan, A.A., Roeser, H.A. & Weiss, W., 2002: Basalt and peridotite recovered from Murray Ridge: are they of supra-subduction origin? In: P.D. Clift, D. Kroon, C. Gaedicke & J. Craig (eds.): The tectonic & climatic evolution of the Arabian Sea region. *Geological Society Special Publication 195*, pp. 117–135.

Chen, G.-N. & Grapes, R., 2007: *Granite genesis: in-situ melting and crustal evolution*. Springer, 278 pp.

Claeson, D.T. & Andersson, U.B., 2000: The 1.85 Ga Nygård pluton, central southern Sweden: an example of early transscandinavian igneous belt (TIB) noritic magmatism. *Abstracts Volume, 24th Nordic Geological Winter Meeting, Trondheim,* p. 50.

Claeson, D., Antal Lundin, I. & Sukotjo, S., 2013: Beskrivning till berggrundskartan del av Nyköpings kommun. *Sveriges geologiska undersökning K437*, 16 pp.

Claeson, D., Bakker, E., Bergman, T., Hallberg, A., Hedin, P., Jönberger, J., Ladenberger, A., Lewerentz, A., Morris, G., Reginiussen, H., Ripa, M. & Wedmark, M., 2020: Rapportering av regeringsuppdrag: Innovationskritiska metaller och mineral i Bergslagen. *RR 2020:02*, Sveriges geologiska undersökning, 77 pp.

Connolly, J.A.D., 2009: The geodynamic equation of state: What and how. *Geochemistry, Geophysics, Geosystems 10*, Q10014.

Daly, R.A., 1910: Average chemical compositions of igneous-rock types. *Proceedings of the American Academy of Arts and Sciences 45*, 211–240.

De la Roche, H., Leterrier, J., Grandclaude, P. & Marchal, M., 1980: A classification of volcanic and plutonic rocks using R_1R_2-diagram and major-element analyses - its relationships with current nomenclature. *Chemical Geology 29*, 183–210.

Dobbe, R.T.M., 1991a: Ullmannite, cobaltian ullmannite and willyamite from Tunaberg, Bergslagen, Central Sweden. *Canadian Mineralogist 29*, 199–205.

Dobbe, R.T.M., 1991b: Tellurides, selenides and associated minerals in the Tunaberg copper deposits, SE Bergslagen, central Sweden. *Contributions to Mineralogy and Petrology 44*, 89–106.

Dobbe, R., 1993: Bismuth tellurides (joseite-B, bismuthian tsumoite) in a Pb-Zn deposit from Tunaberg, Sweden. *European Journal of Mineralogy 5*, 165–170.

Dobbe, R.T.M., 1994a: Geochemistry of cordierite-anthophyllite rocks, Tunaberg, Bergslagen, Sweden. *Economic Geology 89*, 919–930.

Dobbe, R.T.M., 1994b: The geology and mineralizations of the Tunaberg area, SE Bergslagen, Sweden. PhD Thesis, Vrije Universiteit, Amsterdam, 184 pp.

Dobbe, R.T.M., Lustenhouwer, W.J., Zakrzweski, M.A., Goubitz, K., Fraanje, J. & Schenk, H., 1994: Kieftite, $CoSb_3$, a new member of the skutterudite group from Tunaberg, Sweden. *The Canadian Mineralogist 32*, 179–183.

Dobbe, R.T.M. & Zakrzewski, M.A., 1998: Oenite, CoSbAs, a new mineral species from the Tunaberg Cu-Co-sulfide skarns, Bergslagen, Sweden. *The Canadian Mineralogist 36*, 855–860.

Erdmann, A., 1848: *Försök till en geognostisk-mineralogisk beskrifning öfver Tunabergs socken i Södermanland, med särskildt afseende på der belägne grufvor.* Kungliga svenska vetenskapsakademiens handlingar.

Erdmann, E., 1867: Några ord till upplysning om bladet Nyköping. *Sveriges geologiska undersökning Aa 23*, 104 pp.

Erdmann, E., 1889: Beskrifning till kartbladet Askersund. *Sveriges geologiska undersökning Aa 84*, 100 pp.

Faye, G.H. & Harris, D.C., 1969: On the origin of colour and pleochroism in andalusite from Brazil. *The Canadian Mineralogist 10*, 47–56.

Ferry, J.M., 1996: Prograde and retrograde fluid flow during contact metamorphism of siliceous carbonate rocks from the Ballachulish aureole, Scotland. *Contributions to Mineralogy and Petrology 124*, 235–254.

Geisler, T., Schaltegger, U & Tomaschek, F., 2007: Re-equilibration of zircon in aqueous fluids and melts. *Elements 3*, 43–50.

Geijer, P. & Magnusson N.H., 1944: De mellansvenska järnmalmernas geologi. *Sveriges geologiska undersökning Ca 35*, , 654 pp.

Graser, G. & Markl, G., 2008: Ca-rich Ilvaite–Epidote–Hydrogarnet Endoskarns: a Record of Late-Magmatic Fluid Influx into the Persodic Ilímaussaq Complex, South Greenland. *Journal of Petrology 49*, 239–265.

Hedenberg, A.L., 1807: XII. Undersökning af ett Manganeshaltigt Mineral från Tunaberg. In: W. Hisinger & J. Berzelius (eds.): *Afhandlingar i fysik, kemi och mineralogi 2*, 164 pp.

Henriques, Å., 1957: *Protokoll från kärnkarteringar, Venafältet, kbh A-I.* Vieille-Montagne, Zinkgruvan.

Henriques, Å., 1964: Geology and ores of the Åmmeberg district (Zinkgruvan) Sweden. *Arkiv för mineralogi och geologi 4*, 1–246.

Henriques, Å., 1979: *Protokoll från kärnkarteringar, Silvergruvan, kbh 10-12*. Vieille-Montagne, Zinkgruvan.

Holland, T.J.B. & Powell, R., 1996: Thermodynamics of order-disorder in minerals. 2. Symmetric formalism applied to solid solutions. *American Mineralogist 81*, 1425–1437.

Holland, T.J.B. & Powell R., 1998: An internally consistent thermodynamic data set for phases of petrological interest. *Journal of Metamorphic Geology 16*, 309–343.

Holland, T.J.B. & Powell, R., 2003: Activity-composition relations for phases in petrological calculations: an asymmetric multicomponent formulation. *Contributions to Mineralogy and Petrology 145*, 492–501.

Holland, T. J. B. & Powell, R., 2011: An improved and extended internally consistent thermodynamic dataset for phases of petrological interest, involving a new equation of state for solids. *Journal of Metamorphic Geology 29*, 333–383.

Holland, T.J.B., Baker, J. & Powell, R., 1998: Mixing properties and activity-composition relationships of chlorites in the system $MgO\text{-}FeO\text{-}Al_2O_3\text{-}SiO_2\text{-}H_2O$. *European Journal of Mineralogy 10*, 395–406.

Hoppe, F., 1887: Karta öfver De Bescheska grufvan i Tunabergs socken, Södermanlands län, upprättad efter äldre karta och egna mätningar, afslutade den 29 nov. 1886.

Hughes, C.J., 1973: Spilites, keratophyres, and the igneous spectrum. *Geological Magazine 109*, 513–527.

Ivarsson, F., 2019: *Characterization of Fe-rich skarns and fluorapatite-bearing magnetite occurrences at the Zinkgruvan Zn-Pb-Ag and Cu deposit, Bergslagen, Sweden*. Master's thesis, Luleå University of Technology, 92 pp.

Jansson, N.F. & Allen, R.L., 2013: Timing and setting of skarn and iron oxide formation at the Smältarmossen calcic iron skarn deposit, Bergslagen, Sweden. *Mineralium Deposita* 48, 313–339.

Jansson, N.F., Zetterqvist, A., Allen, R.L., Billström, K. & Malmström, L., 2017: Genesis of the Zinkgruvan stratiform Zn-Pb-Ag deposit and associated dolomite-hosted Cu ore, Bergslagen, Sweden. *Ore Geology Reviews 82*, 285–308.

Jansson, N.F., Zetterqvist, A., Allen, R.L. & Malmström, L., 2018: Geochemical vectors for stratiform Zn-Pb-Ag sulfide and associated dolomite-hosted Cu mineralization at Zinkgruvan, Bergslagen, Sweden. *Journal of Geochemical Exploration 190*, 207–228.

Kelemen, P.B., Hanghøj, K. & Greene, A.R., 2003: One view of the geochemistry of subduction-related magmatic arcs, with an emphasis on primitive andesite and lower crust. In: R.L. Rudnick (ed.): *Treatise on geochemistry*. Elsevier, Oxford, pp. 593–659.

Klaproth, M.H., 1797: Untersuchung des Glanzkobalts von Tunaberg. Beiträge zur chemischen Kenntniss der Mineralkörper, andra bandet. Rottmann, Berlin, pp. 302–307.

Kommerskollegium, 1877: Bidrag till Sveriges officiella statistik. C, Bergshantering. Commerce Collegii underdåniga berättelse för år 1875. Stockholm, K.L. Beckman, 36 pp.

Kommerskollegium, 1880: Bidrag till Sveriges officiella statistik. C, Bergshantering. Commerce Collegii underdåniga berättelse för år 1879. Stockholm, K.L. Beckman, 34 pp.

Kommerskollegium, 1881: Bidrag till Sveriges officiella statistik. C, Bergshantering. Commerce Collegii underdåniga berättelse för år 1880. Stockholm, K.L. Beckman, 32 pp.

Kommerskollegium, 1915: Sveriges officiella statistik, industri och bergshantering. Bergshantering, berättelse för år 1914. Stockholm, K.L. Beckman, 115 pp.

Kommerskollegium, 1916: Sveriges officiella statistik, industri och bergshantering. Bergshantering, berättelse för år 1915. Stockholm, K.L. Beckman, 116 pp.

Kommerskollegium, 1917: Sveriges officiella statistik, industri och bergshantering. Bergshantering, berättelse för år 1916. Stockholm, K.L. Beckman, 116 pp.

Kowallis, B., Christiansen, E., Dorais, M., Winkel, T, Henze, P., Franzen, L. & Webb, H., 2018: Compositional Variation of Fe, Al, and F in titanite (sphene). Geological Society of America Annual Meeting, Indianapolis, Indiana. *Geological Society of America Abstracts with Programs 50-6*, 137–11.

Kumpulainen, R.A., Mansfeld, J., Sundblad, K., Neymark, L. & Bergman, T., 1996: Stratigraphy, age, and Sm-Nd isotope systematics of the country rocks to Zn-Pb sulphide deposits, Åmmeberg district, Sweden. *Economic Geology 91*, 1009–1021.

Leopardi, D., 2020: Temporal and genetical constraints of the Cu-Co Vena-Dampetorp deposit, Bergslagen, Sweden. *Dissertations in Geology at Lund University 582*, 113 pp. 45 hp (45 ECTS credits).

Lewerentz, A., Bakker, E. & Hedin, P., 2019: Undersökning av Vena gruvfält: preliminära resultat från fältarbeten 2018. *SGU-rapport 2019:08*, Sveriges geologiska undersökning, 25 pp.

Locock, A.J., 2014: An Excel spreadsheet to classify chemical analyses of amphiboles following the IMA 2012 recommendations. *Computers & Geosciences 62*, 1–11.

Lundström, I., 1974: Beskrivning till berggrundskartan Nyköping SV. *Sveriges geologiska undersökning Af 109*, 123 pp.

Masch, L. & Heuss-Aßbichler, S., 1991: Microtextures and reaction mechanisms in carbonate rocks: a comparison between the thermoaureoles of Ballachulish and Monzoni (Italy). In: Voll, G., Töpel, J., Pattison, D.R.M., Seifert, F. (eds): *Equilibrium and kinetics in contact metamorphism. The Ballachulish Igneous Complex and its aureole.* Springer, Berlin Heidelberg New York, pp. 229–249.

McDonough, W.F. & Sun, S.-S., 1995: The composition of the Earth. *Chemical Geology 120*, 223–253.

Middlemost, E.A.K., 1994: Naming materials in the magma/igneous rock system. *Earth Science Reviews 37*, 215–224.

Nilsson, M., 1992: Geochemistry of Middle Proterozoic mafic and composite mafic-felsic dykes in southeastern Sweden. *Geologiska Föreningen i Stockholm Förhandlingar 114*, 113–130.

O'Hara, M.J. & Niu, Y., 2009: MORB mantle hosts the missing Eu (Sr, Nb, Ta and Ti) in the continental crust: New perspectives on crustal growth, crust–mantle differentiation and chemical structure of oceanic upper mantle. *Lithos 112*, 1–17.

Ogiermann, J.C., 2002: *Cordierite and its retrograde breakdown products as monitors of fluid-rock interaction during retrograde path metamorphism: case studies in the Schwarzwald and the Bayerische Wald (Variscan belt, Germany).* PhD thesis, Institute of Earth Sciences, Heidelberg University.

Pearce, J.A. & Cann, J.R., 1973: Tectonic setting of basic volcanic rocks determined using trace element analyses. *Earth and Planetary Science Letters 19*, 290–300.

Pearce, J.A. & Parkinson, I.J., 1993: Trace element models for mantle melting: application to volcanic arc petrogenesis. In: H.M. Prichard, T. Alabaster, N.B.W. Harris & C.R. Neary (eds.): Magmatic processes and plate tectonics. *Geological Society Special Publication 76*, 373–403.

Pearce, J.A., 1996: A user's guide to basalt discrimination diagrams. In: Wyman, D.A. (ed.): Trace element geochemistry of volcanic rocks: applications for massive sulphide deposits. *Geological Association of Canada, Short Course Notes 12*, 79–113.

Persson, K.S. & Sjöström, H., 2003: Late-orogenic progressive shearing in eastern Bergslagen, central Sweden. *GFF 125*, 23−36.

Persson, P.-O. & Wikström, A., 1993: A U–Pb dating of the Askersund granite and its marginal augen gneiss. *Geologiska Föreningen i Stockholm Förhandlingar 115*, 321–329.

Plissart, G., Féménias, O., Mãruntiu, M., Diot, H., Demaiffe, D., 2009: Mineralogy and geothermometry of gabbro-derived listvenites in the Tisovita-Iuti ophiolite southwestern Romania. *Canadian Mineralogist 47*, 81–105.

Risku-Norja, H., 1992: Geochemistry of the dolerite dykes in Södermanland, eastern central Sweden. *Geologiska Föreningen i Stockholm Förhandlingar 114*, 67–91.

Powell, R. & Holland, T.J.B., 1999: Relating formulations of the thermodynamics of mineral solid solutions: Activity modeling of pyroxenes, amphiboles, and micas. *American Mineralogist 84*, 1–14.

Putnis, A., Hinrichs, R., Putnis, C.V., Golla-Schindler, U. & Collins, L.G., 2007: Hematite in porous red-clouded feldspars: Evidence of large-scale crustal fluid–rock interaction. *Lithos 95*, 10–18.

Sahlström, F., Jonsson, E., Högdahl, K., Troll, V.R., Harris, C., Jolis, E.M. & Weis, F., 2019: Interaction between high-temperature magmatic fluids and limestone explains 'Bastnäs-type' REE deposits in central Sweden. *Scientific reports 9*, 1–9.

Schaltegger, U., 2007: Hydrothermal zircon. *Elements 3*, 51–79.

Schandl, E.S. & Gorton, M. P., 2002: Applications of high field strength elements to discriminate tectonic setting in VMS environments. *Economic geology 97*, 629–642.

Skelton, A., Mansfeld, J., Ahlin, S., Lundqvist, T., Linde, J. & Nilsson, J., 2018: A compilation of metamorphic pressure–temperature estimates from the Svecofennian province of eastern and central Sweden. *GFF 140*, 1–10.

Solyom, Z., Lindqvist, J.-E. & Johansson, I., 1992: The geochemistry, genesis, and geotectonic setting of Proterozoic mafic dyke swarms in southern and central Sweden. *Geologiska Föreningen i Stockholm Förhandlingar 114*, 47–65.

Stephens, M.B. & Jansson, N. F., 2020: Paleoproterozoic (1.9–1.8 Ga) syn-orogenic magmatism, sedimentation and mineralization in the Bergslagen lithotectonic unit, Svecokarelian orogen. *Geological Society of London Memoirs 50*, 155–206.

Stephens, M.B., Ripa, M., Lundström, I., Persson, L., Bergman, T., Ahl, M, Wahlgren, C.-H., Persson, P.-O. & Wickström, L., 2009: Synthesis of bedrock geology in the Bergslagen region, Fennoscandian Shield, south-central Sweden. *Sveriges geologiska undersökning Ba 58*, 259 pp.

Setterberg, J., 1839: Undersökning af ett nytt mineral, funnet uti Hvena Kobolt-grufvor uti Nerike. *Kongliga vetenskapsacademiens handlingar 27*, 188–193.

Simeonov, A., 1990: *Borrhålsprotokoll VENA8903*. Vieille-Montagne, Zinkgruvan, 13 pp.

Suckow, G., 1831: *Die bedeutendsten Erz- und Gesteinlager und ihre hauptsächlichsten Begleiter im Schwedischen Urgebirge*. Verlag der Grökerschen Buchhandlung, Jena, 88 pp.

Sundblad, K., 1994: A genetic interpretation of the Falun and Åmmeberg ore types, Bergslagen, Sweden. *Mineralium Deposita 29*, 170–179.

Söderlund, U., Isachsen, C., Bylund, G., Heaman, L., Patchett, P.J., Vervoort, J.D. & Andersson, U.B., 2005: U-Pb baddeleyite ages and Hf, Nd isotope chemistry constraining repeated mafic magmatism in the Fennoscandian Shield from 1.6 to 0.9 Ga. *Contributions to Mineralogy and Petrology 150,* 174–194.

Tegengren, F.R. m.fl., 1924: Sveriges äldre malmer och bergverk. *Sveriges geologiska undersökning Ca 17*, , 406 pp.

Tischendorf, G., Förster, H.-J., Gottesmann, B. & Rieder, M., 2007: True and brittle micas: composition and solid-solution series. *Mineralogical Magazine 71*, 285–320.

Trägårdh, J., 1991: Metamorphism of magnesium-altered felsic volcanic rocks from Bergslagen, central Sweden. A transition from Mg-chlorite- to cordierite-rich rocks. *Ore Geology Reviews 6*, 485–497.

Walmstedt, L.E., 1849: *De under namnen Feldspath och Skapolith bekanta, kristalliserade mineralierna från Tunaberg.* Doktorsavhandling, Lefvler och Sebell, Uppsala, 38 pp.

Wasström, A., 1991a: *Borrhålsprotokoll VENA9002*. Vieille-Montagne, Zinkgruvan, 8 pp.

Wasström, A., 1991b: *Borrhålsprotokoll VENA9003*. Vieille-Montagne, Zinkgruvan, 8 pp.

Wasström, A., 1991c: *Borrhålsprotokoll VENA900*4. Vieille-Montagne, Zinkgruvan, 9 pp.

White, R.W., Powell, R. & Johnson, T.E., 2014: The effect of Mn on mineral stability in metapelites revisited: new a–x relations for manganese-bearing minerals. *Journal of Metamorphic Geology 32*, 809–828.

Whitney, D.L. & Evans, B.W., 2010: Abbreviations for names of rock-forming minerals. *American Mineralogist 95*, 185–187.

Wiewióra, A. & Weiss, Z.,1990: Crystallochemical classifications of phyllosilicates based on the unified system of projection of chemical composition: II. The chlorite group. *Clay Minerals 25*, 83–92.

Wikström, A. & Karis, L., 1991: Beskrivning till berggrundskartorna Finspång NO, SO, NV, SV. *Sveriges geologiska undersökning Af 162, 163, 164, 165*, 216 pp.

Wood, D.A., Joron, J.L., Treuil, M., Norry, M. & Tarney, J., 1979: Elemental and Sr isotope variations in basic lavas from Iceland and the surrounding ocean floor; the nature of mantle source inhomogeneities. *Contributions to Mineralogy and Petrology 70*, 319–339.

Zakrzewski, M.A. & Makovicky, E., 1986: Izoklakeite from Vena, Sweden, and the kobellite homologous series. *Canadian Mineralogist 24*, 7–18.

Åberg, A., 1987: *Protokoll över diamantborrhål Vena gruvfält: Vena DBH A, B, G, H, I samt Silvergruvan DBH 10 och 12*. Vieille-Montagne, Zinkgruvan, 17 pp.

Åberg, A., 1988: Ädelmetaller och deras relation till Co-Ni-arsenider i den svekokarelska orogenesen. *STU-rapport*, 12 pp.

Xie, L., Wang, R.-C., Chen, J. & Zhu, J.-C., 2010: Mineralogical evidence for magmatic and hydrothermal processes in the Qitianling oxidized tin-bearing granite (Hunan, South China): EMP and (MC)-LA-ICPMS investigations of three types of titanite. *Chemical Geology 276*, 53–68.

Xie, X., Byerly, G.R. & Ferrell, R.E., 1997: IIb trioctahedral chlorite from the Barberton greenstone belt: crystal structure and rock composition constraints with implications to geothermometry. *Contributions to Mineralogy and Petrology 126*, 275–291.

APPENDIX 1. MINERAL ASSEMBLAGES, VENA GRUVFÄLT

Appendix 1A. Summary of mineral identifications and point counting results: silicates and other non-opaque minerals.

vol%	Pl	Qz	Bt	Kfs	Chl	Zrn	Grt	Ms	Ttn	Ap	Tur	Ep	Ser	Cal	Act	Cpx	Hbl	Crd	Mnz	Opx	Ath	Zo	Sil	And	Xtm	Prh	Sd	Aln	Srp	Par	Opq	n*
ALZ180002A	21.1																74.1												0.8		4.1	663
ALZ180008A	10.8	57.6	10.2	19.6		x	x	x		x	x								x												1.8	500
ALZ180033A	23.3	0.6															74.7														1.4	695
ALZ180034A	3.3	75.8	1.6	4.5	0.7	x	x	13.8			x			0.1					x												0.1	669
ALZ180035A	23.8	2.8	31.5	0.3				3.3						0.4		2.4	35.6															720
ALZ180037A	25.7	20.5	40.9	6.8	0.8	x	x	0.9		x				0.6					x		1.2				x						2.5	643
ALZ180052B	48.3	18.9	x	3.3		0.7		1.0	0.3			x			21.6																5.8	582
ALZ180059A	40.4	18.5	27.4	8.8	0.3	x		3.1			0.1																				1.3	674
ALZ180067A	26.2	35.4	24.1	5.3	0.6	x	0.2	1.1				x								4.6											2.6	656
ALZ180072A	37.0	3.0		1.1	43.6		x					10.2																			5.1	629
ALZ180076A	28.3	34.9	28.3	5.6		x	x	2.0			0.5							x		0.3				x	x						0.2	611
ALZ180085A	36.2	26.4	18.5	16.6	x	x	1.1	1.1																								265
ALZ180087A	18.1	17.4		61.0	2.8			0.3				x																			0.3	287
ALZ180089A-1		8.2				x	30.1		1.4					11.7		10.7						36.9									1.1	366
ALZ180089A-1		96.5				0.5								3.1																		424
ALZ180089A-2	22.8	11.9		28.6	0.6	0.1		3.4	0.6					0.1		11.9					2.2		0.7								17.0	681
ALZ180089A-3	22.6	19.7		1.2		0.3		0.5	0.3	x						10.4					1.5	0.5									43.0	651
ALZ190012A																																-
ALZ190015A																			x													-
ALZ190034A	x	x	x	x	x	x	x		x	x																						-
ALZ190037A	x	x	x	x	x	x	x			x					x				x									x		x		-
ALZ190087A	x	x			x										x			x				x										-
ALZ190088A-1	x	x	x	x		x																										-
ALZ190088A-2	x	x	x	x		x					x																					-
EDB180002A	18.6	45.6	25.0	1.0	0.2	x	x	4.8					4.4										0.4									500
EDB180003A	22.4		13.4										5.6				58.0														0.6	500
EDB180005A	24.8	34.2	14.2	2.2	9.8	x	x	2.2		x			12.6																			500
EDB180020A	5.6	35.2	25.2	13.4	0.4		0.4	2.0		1.2			11.4					5.0					0.2									500
EDB180026A	9.2				45.2				1.6			31.4				2.6					5.8										4.0	500
EDB180026B	34.8				63.8				0.1			0.8																			0.3	600
EDB180028A	27.8		4.0		0.4	0.2			1.4				29.2				36.8									0.4						500
EDB180031A	15.0	56.0	15.6		0.4				0.8																						12.4	500
EDB180034A	23.6	28.0	23.2	6.0	0.4				0.2	1.4			3.0																		14.2	500
EDB180039A	23.8	20.0	49.8								0.2				5.0					0.2											1.0	500
EDB180050A	10.8	33.6	17.6	2.8			0.2																				29.4				4.8	500
EDB180057A	0.2	29.8	49.0		x	0.2						x																			19.4	500
EDB180060A	2.8	18.2		29.2	13.6							16.6																			2.8	500
EDB180071A	2.8	5.2	27.6	8.4							x							33.8					9.0	x								500
EDB180072A	29.1	25.0		18.3	x		x		x	x					x																3.3	120
EDB190001A	x	x	x	x	x						x							x		x												-
EDB190012A	x	x	x	x	x	x	x				x																					-
EDB190018A	x	x									x		x																			-
EDB190018B		x	x				x			x	x			x																		-
EDB190020A	x	x	x	x																												-
EDB190021A		x	x	x		x																										-
EDB190023B	x	x	x	x	x		x	x	x	x																						-
EDB190035A	x	x	x		x		x		x	x					x	x						x										-

The rightmost column "n" gives the number of counts from point counting, which the mineral mode calculations are based on, samples with a dash in this column were not systematically point counted. Columns marked with "x" reflect either: (1) for point counted samples, minerals that were identified in very low abundance (<0.2 vol% at 500 counts), or (2) for samples not point counted, identified minerals regardless of their abundance. Abbreviations according to Whitney & Evans (2010), except parisite = Par.

Appendix 1B. Summary of mineral identifications: opaque phases.

	Ccp	Py	Po	Sp	Gn	Mag	Apy	Cob	Gr	Mol	Hem	Cv	Pn	Rt	Car	Bis
ALZ180002A																
ALZ180008A		x														
ALZ180033A	x	x	x	x												
ALZ180034A																
ALZ180035A	x	x														
ALZ180037A	x	x		x	x		x	x								x
ALZ180052B	x	x	x	x							x					
ALZ180059A		x	x	x												
ALZ180067A		x	x	x												
ALZ180072A	x							x	x	x					x	
ALZ180076A	x	x	x													
ALZ180085A			x									x				
ALZ180087A	x		x													
ALZ180089A-1	x	x														
ALZ180089A-1																
ALZ180089A-2		x			x						x					
ALZ180089A-3	x	x	x		x											
ALZ190012A	x	x	x	x												
ALZ190015A	x	x	x	x	x											
ALZ190034A	x	x	x	x		x								x		
ALZ190037A	x		x			x										
ALZ190087A	x	x		x				x								
ALZ190088A-1	x	x	x										x			
ALZ190088A-2	x	x	x										x			
EDB180002A																
EDB180003A						x								x		
EDB180005A																
EDB180020A											x					
EDB180026A		x							x							
EDB180026B	x			x												
EDB180028A																
EDB180031A	x		x	x												
EDB180034A	x		x													
EDB180039A	x															
EDB180050A	x		x	x		x	x									
EDB180057A	x	x				x										
EDB180060A	x			x								x				
EDB180071A																
EDB180072A	x	x	x	x	x				x							
EDB190001A	x	x	x	x			x									
EDB190012A	x	x	x	x			x			x						
EDB190018A	x	x	x	x												
EDB190018B	x	x	x	x												
EDB190020A	x	x	x	x												
EDB190021A	x	x	x	x				x		x						
EDB190023B	x	x	x	x												
EDB190035A	x	x	x	x												

Abbreviations according to Whitney & Evans (2010), except cobaltite = Cob, carrollite = Carr, and bismuthinite = Bis.

APPENDIX 2. MINERAL ASSEMBLAGES, TUNABERG

Appendix 2A. Summary of mineral identifications and point counting results: silicates and other non-opaque phases.

	Qz	Grt	Bt	Kfs	Cal	Cpx	Ms	Ap	Hbl	Pl	Ol	Ttn	Gru	Chl	Zrn	Act	Crd	Opx	Srp	Tur	Zo	Sil	Ser	Tr	Mnz	Fl
ALZ190001A	x	x	x	x	x		x			x				x	x										x	
ALZ190002A	x	x	x	x			x	x		x				x			x						x			
ALZ190004A	x	x	x	x			x	x		x		x			x											
ALZ190005A	x	x	x	*		x	x			x		x			x	x										
ALZ190006A	x	x			x						x	x							x							
ALZ190007A	x	x		x		x						x		x	x						x					
ALZ190008A		x	x	x	x	x		x	x	x																
ALZ190009A	x		x	x		x			x																	
ALZ190010A-1	x	x		x	x	x					x	x														
ALZ190010A-2					x					x		x		x							x					
ALZ190011A-1	x	x	x		x	x			x				x													
ALZ190011A-2	x	x	x		x				x				x													
ALZ191049A	x		x	x																						x
ALZ191051A	x		x	x			x										x			x		x				
ALZ191059A-1	x	x	x					x																		
ALZ191059A-2	x	x	x					x	x				x													
ALZ191060A	x		x						x																	
ALZ191070B	x	x	x	x			x	x									x			x						
ALZ191074A	x	x	x	x			x	x	x													x				
EDB190054A	x	x			x	x		x			x					x		x								
EDB190054B	x	x			x	x		x			x			x		x			x					x		
EDB190067A	x	x	x		x	x		x			x							x								
EDB190069A	x				x	x	x				x					x		x	x							
EDB190070B-1	x	x	x		x	x					x		x					x	x							
EDB190070B-2	x	x	x		x		x						x													
EDB190076A	x	x				x			x				x													
EDB190083A	x	x	x	x			x			x					x		x									

*Hyalophane. Other abbreviations according to Whitney & Evans (2010).

Appendix 2B. Summary of mineral identifications and point counting results: opaque phases.

	Po	Ccp	Sp	Gn	Gr	Py	Mag	Pn	Cbn	Cob	Skut	Btp	Mrc	Apy	Hem	Cv	Ilm
ALZ190001A	x		x	x	x												
ALZ190002A	x	x	x	x	x												
ALZ190004A	x		x		x												
ALZ190005A	x		x	x	x												
ALZ190006A	x			x													
ALZ190007A	x	x	x	x	x	x											
ALZ190008A	x	x	x														
ALZ190009A	x	x	x	x													
ALZ190010A-1	x	x	x	x													
ALZ190010A-2	x	x	x														
ALZ190011A-1	x	x	x	x			x										
ALZ190011A-2		x	x	x			x										
ALZ191049A	x	x	x	x	x	x						x	x				
ALZ191051A																	
ALZ191059A-1	x	x	x		x												
ALZ191059A-2	x	x	x	x	x	x											x
ALZ191060A			x				x										
ALZ191070B										x	x						
ALZ191074A																	
EDB190054A	x	x	x	x	x		x	x	x	x		x				x	
EDB190054B		x						x	x								
EDB190067A	x	x	x	x	x		x	x	x						x		
EDB190069A	x	x	x	x		x		x	x								
EDB190070B-1	x	x						x	x	x	x			x			
EDB190070B-2	x	x					x	x	x	x	x						
EDB190076A		x				x											
EDB190083A					x	x											

Abbreviations according to Whitney & Evans (2010), except Cob = Cobaltite, Btp = breithauptite, and Skut = skutterudite.

APPENDIX 3. SEM-EDS DATA, VENA GRUVFÄLT

Appendix 3A. SEM-EDS compositional data for aluminous minerals from Vena gruvfält.

	ALZ180076A				
wt%	**volcanic andalusite**	**andalusite**	**cordierite**	**cordierite**	**cordierite**
SiO_2	51.66	51.96	69.37	68.93	68.63
Al_2O_3	85.44	88.94	48.37	46.16	46.97
Fe_2O_3*	1.93	1.74			
FeO			6.61	6.38	6.03
MgO			14.91	14.59	15.11
Total	139.03	142.64	139.27	136.06	136.74
atoms per formula unit					
Mg			1.59	1.59	1.64
Al	1.96	1.99	4.07	3.97	4.02
Si	1.01	0.99	4.96	5.03	4.98
Fe^{+3}	0.03	0.02			
Fe^{+2}			0.39	0.39	0.37
Cations	3.00	3.00	11.01	10.98	11.01
O	5	5	18	18	18
#Mg			0.80	0.80	0.82

*Calculated from total Fe content, all Fe assumed to substitute for ^{VI}Al.

Appendix 3B. SEM-EDS compositional data for amphiboles from Vena gruvfält.

	ALZ180037A				**ALZ180089A**			**EDB180072A**			
	volcanic (♀)				**skarn (♀)**			**volcanic (♀)**			
Wt%	**actinolite**	**actinolite**	**actinolite**	**actinolite**	**actinolite**	**actinolite**	**actinolite**	**tremolite**	**tremolite**	**tremolite**	**tremolite**
SiO_2	52.91	55.30	55.28	53.06	58.87	58.06	57.23	40.43	40.88	39.86	40.69
Al_2O_3	3.91	2.10	1.93	1.85	1.53	1.72	1.15	1.34	1.38	1.55	0.96
MnO			0.58	0.63		0.36		0.36		0.34	
Mn_2O_3*		0.69									
FeO	11.00		10.61	6.74	6.68	6.38	6.52	2.11	0.00	2.51	2.51
Fe_2O_3*	2.67	10.24		3.59					3.16		
MgO	15.31	17.36	18.22	17.26	21.21	20.70	20.33	15.59	16.00	15.27	15.62
CaO	12.36	11.84	12.30	11.75	13.56	13.46	13.28	9.26	9.44	9.21	9.40
Na_2O	0.50			0.40					0.26	0.22	
K_2O	0.18									0.16	
Total	98.83	97.53	98.93	95.29	101.85	100.68	98.51	69.10	71.12	69.10	69.19
T (ideally 8 atoms per formula unit)											
Si	7.53	7.90	7.73	7.74	7.86	7.85	7.91	7.85	7.75	7.76	7.90
Al	0.47	0.11	0.27	0.26	0.14	0.15	0.09	0.15	0.25	0.24	0.11
T total	8	8	8	8	8	8	8	8	8	8	8
C (ideally 5 apfu)											
Al	0.19	0.25	0.05	0.06	0.10	0.12	0.09	0.16	0.06	0.12	0.12
Fe^{3+}	0.29		0.22	0.20	0.05	0.04			0.18	0.12	
Mn^{2+}										0.04	
Fe^{2+}	1.28	1.06	0.93	0.99	0.64	0.68	0.72	0.33	0.24	0.29	0.37
Mg	3.25	3.70	3.80	3.75	4.22	4.17	4.19	4.51	4.52	4.44	4.52
C total	5	5	5	5	5	5	5	5	5	5	5
B (ideally 2 atoms per formula unit)											
Mn^{2+}		0.08	0.07	0.08		0.04		0.06		0.02	
Fe^{2+}	0.03	0.04	0.09	0.03	0.06	0.01	0.03	0.01	0.04		0.04
Ca	1.88	1.81	1.84	1.84	1.94	1.95	1.97	1.93	1.92	1.92	1.96
Na	0.09			0.06					0.04	0.06	
B total	2.00	1.93	2.00	2.00	2.00	2.00	2.00	2.00	2.00	2.00	2.00
A (from 0 to 1 atoms per formula unit)											
Na	0.05			0.06					0.05	0.02	
K	0.03									0.04	
A total	0.08	0.00	0.00	0.06	0.00	0.00	0.00	0.00	0.05	0.06	0.00
O	22	22	22	22	22	22	22	22	22	22	22
OH	2	2	2	2	2	2	2	2	2	2	2
Sum T,C,B,A	15.08	14.93	15.00	15.06	15.00	15.00	15.00	15.00	15.05	15.06	15.00

*Calculated from charge balance (Locock 2014).

Appendix 3C. SEM-EDS compositional data for carbonates from Vena gruvfält.

	ALZ180089A				ALZ190037A				
	skarn (♀)				skarn (♂)				
Wt%	**calcite**	**calcite**	**calcite**	**calcite**	**parisite -(La)**	**parisite-(La)**	**parisite-(La)**	**parisite-(La)**	**parisite-(La)**
CaO	75.30	72.25	54.85	55.53	5.21	2.78	1.71	9.54	3.79
MnO		0.63							
FeO		0.64							3.82
SiO_2						0.41		2.29	11.12
Al_2O_3									5.61
La_2O_3					38.08	40.88	37.26	33.92	26.66
Ce_2O_3					23.67	22.86	29.60	22.22	24.80
Nd_2O_3					3.37	3.48	3.36	3.01	3.78
F					5.43	5.28	5.83	4.43	3.08
Total	75.30	73.53	54.85	55.53	75.76	75.69	77.75	75.41	82.66

Appendix 3D. SEM-EDS compositional data for epidote, allanite, clinozoisite, and zoisite from Vena gruvfält.

	ALZ190037A							ALZ180089A									EDB190023B
	skarn (♂)							skarn (♀)									volcanic (♀)
wt%	**Aln-Ep**	**Aln-Ep**	**Aln-Ep**	**Aln-Ep**	**Aln-Ep**	**Aln-Ep**	**Aln-Ep**	**Czo-Ep**	**Czo-Ep**	**Czo-Ep**	**Czo-Ep**	**Czo-Ep**	**Czo-Ep**	**Czo**	**Zo**	**Zo**	**Czo**
SiO_2	33.16	35.81	32.07	32.28	32.15	33.20	33.24	53.42	40.07	38.70	39.68	54.27	54.51	40.05	45.67	45.07	39.47
TiO_2													0.23				
Al_2O_3	17.52	20.48	17.29	17.18	17.69	19.69	18.44	38.43	28.78	27.40	27.95	38.41	38.11	31.55	25.72	25.56	30.35
FeO	12.22	10.86	12.07	10.67	12.21	12.32	11.46	10.81	6.81	7.91	7.01	10.97	10.33	4.43			5.91
MgO	1.94	1.06	1.74	1.51	1.79	1.09	1.29										
CaO	11.66	14.69	11.68	9.98	11.25	13.95	12.94	32.70	24.51	24.05	24.15	33.79	33.04	24.96	27.90	27.83	24.23
La_2O_3	11.76	8.88	10.65	10.16	11.20	8.20	10.31										
Ce_2O_3	11.75	8.21	10.16	9.96	10.08	8.32	8.97										
Nd_2O_3				1.60	2.06												
Total	100.00	99.99	95.65	93.32	98.44	96.77	96.66	135.35	100.16	98.06	98.79	137.45	136.22	100.99	99.29	98.47	99.95

atoms per formula unit																	
Si	3.13	3.15	3.11	3.22	3.09	3.05	3.13	2.99	3.02	2.99	3.03	3.00	3.03	2.98	3.42	3.41	2.97
Ti													0.01				
Al	1.95	2.13	1.98	2.02	2.01	2.13	2.05	2.53	2.56	2.50	2.52	2.50	2.49	2.76	2.27	2.28	2.69
Fe^{+3}	0.97	0.80	0.98	0.89	0.98	0.95	0.90	0.51	0.43	0.51	0.45	0.51	0.48	0.28			0.37
Mg	0.27	0.14	0.25	0.22	0.26	0.15	0.18										
Ca	1.18	1.39	1.22	1.07	1.16	1.37	1.31	1.96	1.98	1.99	1.98	2.00	1.97	1.99	2.24	2.26	1.96
La	0.14	0.10	0.13	0.12	0.13	0.09	0.12										
Ce	0.14	0.09	0.12	0.12	0.12	0.09	0.10										
Nd				0.02	0.02												
H	1	1	1	1	1	1	1	1	1	1	1	1	1	1	1	1	1
Cations	8.77	8.79	8.78	8.69	8.77	8.83	8.79	8.99	8.99	9.00	8.98	9.00	8.98	9.00	8.94	8.95	8.99
O	12.5	12.5	12.5	12.5	12.5	12.5	12.5	12.5	12.5	12.5	12.5	12.5	12.5	12.5	12.5	12.5	12.5

end members																	
Czo	0	13	0	2	1	13	5	53	56	50	52	50	49	76			69
Aln	27	18	25	26	27	19	22	0	0	0	0	0	0	0			0
Ep	73	69	75	71	72	69	73	47	44	50	48	50	51	24			31
Total	100	100	100	100	100	100	100	100	100	100	100	100	100	100			100

The proportion of clinozoisite was calculated as Al (apfu) - 2 [if Al (apfu) > 2; otherwise taken as zero], the proportion of allanite is equal to REE (apfu), and epidote is 1 - (allanite + clinozoisite) in accordance with Graser & Markl (2008).

Appendix 3E. SEM-EDS compositional data for feldspars from Vena gruvfält.

	ALZ180076A				**ALZ180089A**					**ALZ190034A**	**ALZ190037A**		**EDB180034A**	**EDB180072A**	**EDB190023B**
	volcanic				**skarn (♀)**					**volcanic (♀)**	**skarn (♂)**		**volcanic (♀)**	**volcanic (♀)**	**volcanic (♀)**
wt%	**plagioclase**	**plagioclase**	**plagioclase**	**plagioclase**	**K-feldspar**	**K-feldspar**	**plagioclase**	**plagioclase**	**plagioclase**	**K-feldspar**	**anorthoclase**	**plagioclase**	**plagioclase**	**plagioclase**	**K-feldspar**
SiO_2	85.16	83.41	85.93	84.43	66.49	65.61	40.62	59.43	59.68	64.11	62.23	55.96	60.54	41.80	68.05
Al_2O_3	35.07	33.88	34.28	34.50	19.03	20.37	18.65	28.04	26.70	19.80	26.26	28.97	21.65	18.84	19.59
FeO												0.60			0.69
CaO	8.54	8.07	8.42	8.62			5.99	9.12	9.11		0.77	10.33	5.11	5.85	
BaO						1.91				1.32					
Na_2O	11.38	10.97	11.67	11.24	0.54	0.40	4.61	6.58	6.69	0.89	7.31	5.86	7.52	4.89	0.44
K_2O	0.00	0.28	0.00	0.25	16.42	16.18	0.14	0.34	0.25	12.97	3.23	0.00	0.33	0.18	16.79
Total	140.14	136.61	140.30	139.05	102.47	104.47	70.02	103.51	102.43	99.09	99.80	101.72	95.15	71.56	105.57
atoms per formula unit															
Si	2.70	2.71	2.72	2.70	3.00	2.93	2.60	2.57	2.61	3.02	2.77	2.48	2.84	2.61	2.98
Al	1.31	1.30	1.28	1.30	1.01	1.07	1.41	1.43	1.38	1.10	1.38	1.51	1.20	1.39	1.01
Fe^{+3}												0.02			
Fe^{+2}															0.03
Ca	0.29	0.28	0.29	0.30			0.41	0.42	0.43		0.04	0.49	0.26	0.39	
Ba						0.03				0.02					
Na	0.70	0.69	0.72	0.70	0.05	0.04	0.57	0.55	0.57	0.08	0.63	0.50	0.68	0.59	0.04
K		0.01		0.01	0.94	0.92	0.01	0.02	0.01	0.78	0.18		0.02	0.01	0.94
Cations	5	5	5	5	5	5	5	5	5	5	5	5	5	5	5
O	8.01	8.01	8.00	7.99	8.01	7.99	8.01	8.00	8.01	8.14	8.05	7.99	8.09	8.00	8.00
endmembers															
An	29	29	29	29	0	0	41	43	42	0	4	49	27	39	0
Ab	71	70	71	70	5	4	58	56	56	9	74	51	71	59	4
Or	0	1	0	1	95	96	1	2	1	91	22	0	2	1	96
Total	100	100	100	100	100	100	100	100	100	100	100	100	100	100	100

Appendix 3F. SEM-EDS compositional data for garnet from Vena gruvfält.

wt%	**ALZ180089A skarn (♀) garnet**	**garnet**	**garnet**	**garnet**	**garnet**	**garnet**	**EDB190023B volcanic (♀) garnet**
MgO							1.63
Al_2O_3	23.73	25.26	17.61	17.99	17.91	27.47	16.93
SiO_2	53.12	54.68	38.18	40.43	39.34	55.36	26.23
CaO	46.16	46.65	32.57	34.90	33.24	48.19	
TiO_2						0.62	
MnO	1.02	1.07	0.70	0.80	0.94	0.93	
FeO	11.50	12.52	8.25	8.54	8.40	9.46	43.64
Total	135.53	140.18	97.31	102.66	99.84	142.03	88.42

end members							
almandine	5	7	7	6	7	6	91
pyrope							9
grossular	75	75	76	75	76	80	
spessartine	2	2	2	2	2	1	
uvarovite							
andradite	18	17	15	17	15	11	
Ca-Ti Gt						1	
Total	100	100	100	100	100	100	100

Appendix 3G. SEM-EDS compositional data for chlorite and mica group minerals from Vena gruvfält.

wt%	ALZ18 0037A volc. (♀) Bt	ALZ18 0076A volc. Bt	Bt	Bt	Bt	Bt	Bt	Bt	ALZ18 0089A skarn (♀) Chl	Chl	ALZ19 0034A volc. (♀) Chl	Chl	Chl	ALZ19 0037A skarn (♂) Chl	EDB1800 34A volc. (♀) Bt	Chl	EDB18 0072A volc. (♀) Bt	Bt	Chl	Chl	Chl	Chl	EDB19 0023B volc. (♀) Chl	EDB19 0035A volc. (♀) Chl
SiO_2	36.58	50.42	50.25	49.74	50.46	51.13	51.19	51.90	30.27	29.18	33.86	34.18	36.73	30.83	39.08	25.73	24.66	25.86	19.12	19.30	22.18	20.86	29.26	34.25
Al_2O_3	17.16	26.21	26.32	25.02	28.00	27.13	26.76	27.25	14.21	11.66	26.79	27.66	29.53	14.87	16.42	15.13	11.94	10.52	11.77	12.19	10.62	10.09	20.48	22.84
TiO_2	1.23	2.10	1.78	2.34	2.09	2.64	2.20	1.42							2.14		0.72	0.60						0.67
FeO	18.41	18.49	17.59	18.77	17.43	18.41	19.22	19.05	38.78	36.78	28.08	27.44	21.90	32.37	6.69	36.76	8.00	6.42	22.86	25.05	17.92	19.28	13.60	17.05
MnO															0.40		0.41	0.54	0.35				0.88	0.81
MgO	12.45	19.19	20.25	19.58	19.30	19.42	19.68	20.15	8.77	8.09	11.26	9.48	10.45	7.69	19.42	5.39	14.51	13.65	6.38	5.36	10.89	10.02	24.59	23.61
CaO										0.42				0.36						0.20		0.15		0.38
K_2O	9.19	13.40	13.66	13.20	13.61	13.72	13.03	13.31						0.71	9.85		3.49	4.22						0.40
Cl	0.20																							
Total	95.23	129.80	129.85	128.64	130.90	132.44	132.09	133.07	92.03	86.13	100.00	98.77	98.61	86.83	94.00	83.01	63.74	61.81	60.49	62.08	61.62	60.40	88.81	100.01
atoms per formula unit																								
Si	5.54	5.47	5.44	5.46	5.40	5.43	5.45	5.47	3.23	3.34	3.05	3.10	3.22	3.39	5.67	3.08	5.30	5.68	3.04	3.03	3.29	3.22	2.85	2.98
Al^{IV}	2.46	2.53	2.56	2.54	2.60	2.57	2.55	2.53	0.77	0.66	0.95	0.90	0.78	0.61	2.33	0.92	2.70	2.32	0.96	0.97	0.71	0.78	1.15	1.02
Al^{VI}	0.60	0.81	0.79	0.69	0.93	0.82	0.80	0.86	1.02	0.92	1.90	2.06	2.28	1.32	0.48	1.21	0.32	0.41	1.25	1.28	1.15	1.05	1.21	1.33
Ti^{VI}	0.14	0.17	0.15	0.19	0.17	0.21	0.18	0.11							0.23		0.12	0.10						0.04
Fe^{+2}	2.33	1.68	1.59	1.72	1.56	1.63	1.71	1.68	3.46	3.52	2.12	2.08	1.61	2.98	0.81	3.68	1.44	1.18	3.04	3.28	2.22	2.49	1.11	1.24
Mn															0.05		0.08	0.10	0.05				0.07	0.06
Mg	2.81	3.10	3.27	3.20	3.08	3.07	3.12	3.17	1.40	1.38	1.51	1.28	1.37	1.26	4.20	0.96	4.65	4.47	1.51	1.25	2.41	2.30	3.58	3.07
Ca										0.05				0.04						0.03		0.03		0.04
K	1.77	1.85	1.89	1.85	1.86	1.86	1.77	1.79						0.10	1.82		0.96	1.18						0.04
Cl	0.05																							
Cat	15.65	15.61	15.68	15.66	15.60	15.59	15.58	15.61	5.88	5.87	5.53	5.42	5.25	5.70	15.60	5.85	15.55	15.44	5.85	5.85	5.78	5.87	5.97	5.82
O	20	20	20	20	20	20	20	20	10	10	10	10	10	10	20	10	20	20	10	10	10	10	10	10
OH	3.95	4	4	4	4	4	4	4	8	8	8	8	8	8	4	8	4	4	8	8	8	8	8	8
#Mg	0.55	0.65	0.67	0.65	0.66	0.65	0.65	0.65	0.29	0.28	0.42	0.38	0.46	0.30	0.84	0.21	0.76	0.79	0.33	0.28	0.52	0.48	0.76	0.71
T (°C)*									180	145	490	534	622	278		226			264	261	271	232	343	371

*Formation temperature of chlorite, as calculated from the thermometer proposed by Xie et al. (1997).

Appendix 3H. SEM-EDS compositional data for pyroxene from Vena gruvfält.

	ALZ180089A skarn (♀)			
wt%	**Di-Hd**[1]	**Di-Hd**[1]	**diopside**	**diopside**
SiO_2	73.10	68.60	55.64	55.23
FeO	21.81	20.69	7.10	5.39
MnO		0.98	0.59	
MgO		10.83	15.17	15.74
CaO	33.48	31.78	25.41	24.92
Total	140.76	132.88	103.91	101.28

apfu[2]				
Si	2.01	2.00	1.99	2.01
Fe^{+3}			0.02	
Fe^{+2}	0.50	0.51	0.19	0.16
Mn		0.02	0.02	
Mg	0.51	0.47	0.81	0.85
Ca	0.99	0.99	0.97	0.97
O	6.01	6.00	5.99	6.01

End members				
Wollastonite	49	50	49	49
Enstatite	25	24	41	43
Ferrosilite	25	26	10	8
Total	100	100	100	100

[1] Di-Hd: composition represents the 50/50 component between diopside and hedenbergite. High analytical totals are due to error in instrument setup, stoichiometric calculations conform well with the pyroxene formula.

[2] Fe^{3+} is calculated based on site vacancies.

Appendix 3I. SEM-EDS compositional data for phosphates and sulphates from Vena gruvfält.

	ALZ180037A						ALZ180089A		ALZ190037A	EDB180034A			EDB180072A		EDB190035A	
	volcanic (♀)						skarn (♀)		skarn (♂)	volcanic (♀)			volcanic (♀)		volcanic (♀)	
wt%	**apatite**	**apatite**	**apatite**	**apatite**	**apatite**	**monazite**	**apatite**	**apatite**	**apatite**	**apatite**	**apatite**	**apatite**	**apatite**	**apatite**	**apatite**	**baryte**
SO_3																40.13
P_2O_5	42.92	42.46	42.39	41.29	42.67	30.27	43.70	43.15	42.49	42.81	42.56	42.94	28.74	28.55	43.33	
La_2O_3						32.58										
Ce_2O_3						29.54										
Nd_2O_3						4.39										
CaO	55.02	54.44	54.89	53.53	55.13		56.70	55.80	54.32	54.72	54.64	55.04	37.46	37.48	52.04	
BaO																59.53
CoO																0.34
Cl			0.23	0.20					0.52	0.21						
F	3.12	2.80	3.03	2.63	3.21		3.73	3.19	3.56	3.28	3.02	3.19	2.86	2.73	4.63	
Total	101.06	99.71	100.55	97.66	101.01	96.78	104.13	102.14	100.88	101.02	100.21	101.18	69.05	68.77	100.00	100.01

atoms per formula unit																
S																1.06
P	5.87	5.89	5.84	5.86	5.85	1.02	5.81	5.85	5.83	5.86	5.87	5.87	5.77	5.76	5.93	
La						0.48										
Ce						0.43										
Nd						0.06										
Ca	9.52	9.55	9.58	9.62	9.56		9.54	9.57	9.44	9.48	9.54	9.52	9.51	9.57	9.00	
Ba																0.82
Co																0.01
Cl	0.00	0.00	0.06	0.06	0.00		0.00	0.00	0.14	0.06	0.00	0.00	0.00	0.00	0.00	
F	1.59	1.45	1.56	1.39	1.64		1.85	1.61	1.83	1.68	1.56	1.63	2.14	2.06	2.36	
OH	-0.59	-0.45	-0.62	-0.45	-0.64		-0.85	-0.61	-0.97	-0.73	-0.56	-0.63	-1.14	-1.06	-1.36	
Cations	16.40	16.44	16.42	16.48	16.41	1.99	16.36	16.42	16.27	16.34	16.41	16.38	16.28	16.33	15.93	0.83
O	24	24	24	24	24	4	24	24	24	24	24	24	24	24	24	4

Appendix 3J. SEM-EDS compositional data for titanite from Vena gruvfält.

wt%	ALZ180089A skarn (♀) titanite	titanite	titanite	titanite	titanite	titanite	titanite	titanite	titanite	titanite	titanite	titanite	titanite	titanite	titanite	titanite	titanite	EDB180072A volcanic (♀) titanite	titanite	EDB190035A volcanic (♀) titanite
SiO_2	30.46	31.21	34.66	31.13	30.83	31.90	31.13	31.40	33.24	31.96	31.10	37.16	33.39	31.21	30.98	31.49	29.59	20.86	21.03	32.58
TiO_2	38.17	34.95	37.73	37.78	36.43	37.05	37.48	37.78	37.20	37.45	36.58	43.04	36.18	37.50	39.18	40.08	34.58	24.37	26.01	38.22
Al_2O_3	1.47	3.76	0.94	1.15	1.40	2.25	1.98	1.38	1.70	2.38	2.97	2.38	3.53	1.55	1.10	1.38	1.64	1.44	1.30	1.38
V_2O_5		0.73	0.79		0.89								0.64		0.77					
Y_2O_3																		0.57		
Ce_2O_3																	1.53			
Nd_2O_3																	1.04			
FeO	0.78			0.48		0.42		0.71				0.55		0.80		0.98	3.74	2.14		
MgO																		0.20		
CaO	28.33	28.54	26.63	28.32	27.77	27.94	28.10	27.89	27.86	29.13	28.87	33.20	27.42	26.04	28.57	28.39	20.78	17.21	19.50	27.82
Na_2O												0.27								
K_2O												0.30	0.87							
Total	99.22	99.19	100.74	98.86	97.32	99.56	98.69	99.16	100.00	100.92	99.52	116.90	102.04	97.10	100.59	102.32	92.90	66.78	67.84	99.99

apfu																				
Si	1.00	1.02	1.10	1.02	1.03	1.04	1.02	1.03	1.07	1.03	1.01	1.03	1.06	1.04	1.00	1.00	1.05	1.02	1.01	1.05
Ti	0.94	0.86	0.90	0.94	0.92	0.91	0.93	0.93	0.90	0.90	0.90	0.90	0.86	0.94	0.96	0.96	0.92	0.90	0.94	0.93
Al	0.06	0.14	0.04	0.04	0.06	0.09	0.08	0.05	0.06	0.09	0.11	0.08	0.13	0.06	0.04	0.05	0.07	0.08	0.07	0.05
V		0.02	0.02		0.02								0.01		0.02					
Y																		0.01		
Ce																	0.02			
Nd																	0.01			
Fe^{+2}	0.02			0.01		0.01		0.02				0.01		0.02		0.03	0.11	0.09		
Mg																		0.01		
Ca	1.00	1.00	0.91	1.00	0.99	0.97	0.99	0.98	0.96	1.00	1.01	0.99	0.93	0.93	0.99	0.97	0.79	0.90	1.00	0.96
Na												0.01								
K												0.01	0.04							
Cations	3.02	3.04	2.97	3.02	3.02	3.01	3.01	3.01	3.00	3.02	3.03	3.04	3.03	2.99	3.01	3.01	2.98	3.03	3.02	2.99
O	5	5	5	5	5	5	5	5	5	5	5	5	5	5	5	5	5	5	5	5

Appendix 3K. SEM-EDS compositional data for zircon from Vena gruvfält.

wt%	**ALZ180037A volcanic (♀) zircon**	**ALZ180089A skarn (♀) zircon**	**zircon**	**zircon**	**EDB180034A volcanic (♀) zircon**
SiO_2	30.78	41.65	43.58	43.30	31.45
ZrO_2	65.80	91.35	96.01	95.58	68.93
CaO	0.62	0.41			
FeO	0.71				
HfO_2	1.32				
Total	99.22	133.41	139.59	138.88	100.38

apfu					
Si	0.96	0.96	0.96	0.96	0.96
Zr	1.00	1.03	1.03	1.03	1.03
Ca	0.02	0.01			
Fe^{+2}	0.02				
Hf	0.01				
Cations	2.02	2.01	2.00	2.00	1.99
O	4	4	4	4	4

High analytical totals are due to error in instrument setup, stoichiometric calculations conform well with the zircon formula.

Appendix 3L. SEM-EDS compositional data for ore-forming minerals from Vena gruvfält.

Mineral	wt%	O	S	Ti	Fe	Co	Ni	Cu	Zn	As	Nb	Sb	Pb	Bi	Total
Arsenopyrite	ALZ180037A	0.25	15.65		23.87	9.31				52.64					101.70
	2σ (n = 12)	0.31	0.61		0.82	0.30				0.92					1.67
	EDB180034A	1.85	16.47		27.31	6.54				52.20					104.72
	(n = 1)														
Bismuthinite	ALZ180037A	2.54	18.08		0.42	2.10	0.10	1.95				0.43		72.61	98.20
	2σ (n = 2)	2.03	1.44		0.58	0.16	0.13	2.70				0.60		3.90	6.87
Chalcopyrite	ALZ180037A		35.23		31.27			40.26							106.77
	2σ (n = 4)		0.49		0.49			0.67							1.56
	ALZ180089A	0.36	36.23		31.31			39.51							107.41
	2σ (n = 9)	0.45	0.27		0.25			0.62							0.70
	ALZ190037A	1.32	34.29		32.63			39.52							107.74
	2σ (n = 2)	1.82	1.57		0.10			0.70							0.55
	EDB180034A	1.59	35.61		29.76			39.65							106.61
	(n = 1)														
	EDB190023B	0.17	35.79		31.72			40.12							107.79
	2σ (n = 5)	0.18	0.20		0.56			0.41							0.83
Cobaltite	ALZ180037A		19.36		1.19	33.58	0.55			46.85					101.53
	2σ (n = 8)		0.24		0.38	0.84	0.59			0.51					1.27
Galena	ALZ180037A	1.17	12.28		0.65								84.07	5.85	104.02
	(n = 1)														

Appendix 3L. Continuation.

Mineral	wt%	O	S	Ti	Fe	Co	Ni	Cu	Zn	As	Nb	Sb	Pb	Bi	Total
Galena	ALZ180089A	1.23	12.41		0.50								89.99		104.13
	2σ (n = 5)	0.61	0.19		0.54								0.84		0.75
Hematite	ALZ180089A	36.54	1.59		52.31			0.98							91.42
	2σ (n = 3)	1.56	1.28		4.04			1.57							0.92
Magnetite	ALZ190034A	28.38	3.25		62.95										94.57
	2σ (n = 2)	0.09	0.14		0.02										0.03
	ALZ190037A	26.30			71.43										97.72
	2σ (n = 4)	0.52			0.43										0.56
Native Bi	ALZ180037A	2.38										1.54		100.09	104.01
	2σ (n = 3)	0.26										0.23		1.53	1.65
Ni-cattierite	ALZ180037A		43.06		1.53	38.15	15.26	0.55							98.55
	(n = 1)														
Pyrite	ALZ180089A	5.02	51.58		45.24	0.63	0.10	0.02	0.01						102.60
	2σ (n = 26)	0.98	1.11		0.68	0.68	0.20	0.04	0.01						0.74
	ALZ190037A		53.39		47.09										100.48
	(n = 1)														
	EDB180034A	0.38	52.68		45.41										98.47
	2σ (n = 9)	0.70	0.80		0.69										1.24
	EDB190023B	3.07	52.23		47.29										102.59
	(n = 1)														

Appendix 3L. Continuation.

Mineral	wt%	O	S	Ti	Fe	Co	Ni	Cu	Zn	As	Nb	Sb	Pb	Bi	Total
Pyrrhotite	ALZ180037A		36.60		57.16			4.68							98.44
	(n = 1)														
	ALZ180089A	0.27	40.67		61.18										102.12
	2σ (n = 16)	0.28	0.17		0.42										0.57
	EDB180034A	0.59	38.71		58.42				0.01						97.73
	2σ (n = 19)	0.35	0.62		0.75				0.02						1.35
	EDB190023B	0.38	38.96		59.07				0.01						98.41
	2σ (n = 6)	0.44	0.72		0.72				0.01						1.58
Rutile	ALZ190034A	40.18	0.41	58.08							0.82				99.48
	2σ (n = 2)	0.08	0.10	1.05							0.15				0.72
Sphalerite	ALZ180089A	0.98	34.40		7.92				59.69						102.99
	2σ (n = 13)	0.26	0.12		0.73				1.03						0.48
	EDB190023B	0.34	33.59		6.92				61.64						102.49
	2σ (n = 4)	0.35	0.47		0.36				1.86						2.28
Willyamite	ALZ180089A	0.07	15.29		0.29	26.17	1.17					60.09			103.08
	2σ (n = 6)	0.13	0.08		0.35	0.33	0.68					0.39			0.74
	EDB190023B	0.60	15.28		1.30	24.55	2.17					47.63		12.04	103.57
	2σ (n = 5)	0.09	0.15		0.19	0.71	1.32					20.88		21.11	1.01

APPENDIX 4. SEM-EDS DATA, TUNABERG

Appendix 4. SEM-EDS mineral compositional data minerals analysed in thin sections from Tunaberg.

Mineral group	Sample	Species	Na_2O	K_2O	MgO	CaO	BaO	MnO	FeO	CoO	NiO	CuO	ZnO	PbO	SiO_2	V_2O_5	As_2O_3	P_2O_5	Al_2O_3	S	F	Total
Amphiboles	ALZ190005A	Actinolite		0.35	20.03	12.86		1.52	5.91						56.50				2.36			99.53
	ALZ190011A	Grunerite			3.32	2.95		1.87	40.09						49.18				1.15			98.56
		Grunerite			3.35	0.64		1.85	42.71						49.67							98.22
		Grunerite			3.81	0.52		2.01	41.99						49.05							97.39
	EDB190054B	Tremolite			21.59	9.93			1.51						50.68				1.28			84.99
		Tremolite			20.66	8.94			1.18						47.25				0.98			79.02
		Tremolite			19.96	8.19			0.94						45.07				1.21			75.37
Carbonates	ALZ190011A	Calcite				51.28		1.41	1.89													54.58
	EDB190054B	Calcite			0.53	33.83																34.36
		Calcite			0.30	28.63		0.32														29.25
		Calcite				34.41																34.41
		Calcite			0.80	34.22		0.54														35.56
		Calcite				33.48																33.48
		Calcite			0.48	54.58		0.89														55.95
		Calcite				51.38		0.79														52.17
Chlorites	ALZ190005A	Chamosite			14.18	0.36		0.81	24.38					1.80	29.59	0.55			16.27			87.94
Feldspars	ALZ190005A	Albite	10.46		0.83		1.53		3.87						64.58				19.80	0.37		101.45
		Hyalophane	0.40	12.95			8.38								58.87				20.27			100.88
Pyroxenes	EDB190054B	Diopside			15.89	16.82		0.37	0.85						44.22							78.14
		Diopside			8.99	7.40		0.71	10.21						42.74							70.06
		Diopside			6.28	7.60		0.71	10.91						40.47							65.98
		Diopside			8.37	9.65		0.94	15.41						47.60							81.98
	EDB190070B	Diopside			16.95	25.76		0.74	4.73						56.77				0.64			105.59
		Diopside			14.51	22.92		0.83	5.67						51.49				1.47			96.89
	ALZ190011A	Hedenbergite			0.85	11.46			34.94						50.46							97.71
Other silicates	EDB190070B	Antigorite			27.63	0.32		0.61	17.37						39.17				6.78			91.87
	EDB190054B	Serpentine			16.91	1.18			5.27						34.76				5.01			63.13

Appendix 4. Continuation.

Mineral group	Sample	Species	Na_2O	K_2O	MgO	CaO	BaO	MnO	FeO	CoO	NiO	CuO	ZnO	PbO	SiO_2	V_2O_5	As_2O_3	P_2O_5	Al_2O_3	S	F	Total
Other silicates	ALZ190011A	Hisingerite			2.06	1.30		0.59	36.61						29.71				5.73			76.00
		Hisingerite			1.64	1.64		0.72	34.34						37.35				3.17			78.86
		Garnet				6.79		6.07	27.44						34.61				19.03			93.94
Phosphates	EDB190054B	Apatite-(CaF)				19.16												21.93			5.07	46.16
	EDB190070B	Apatite-(CaF)				56.49												44.62			4.04	105.14
Sulphides	EDB190070B	Arsenopyrite		0.25		1.47			41.09								10.21			30.23		83.25
	ALZ190011A	Chalcopyrite							42.56			51.01								36.48		130.05
		Chalcopyrite							40.49			48.49								34.68		123.66
	EDB190054B	Chalcopyrite							28.61			48.36								31.84		108.81
		Chalcopyrite							24.98			43.61								28.63		97.23
		Chalcopyrite							29.81			46.82								31.18		107.81
		Chalcopyrite				0.49			20.83			44.84								28.29		94.45
		Chalcopyrite							13.29			38.94								23.43		75.66
		Chalcopyrite							9.61			37.58								20.97		68.16
	EDB190070B	Chalcopyrite							53.16			34.40								35.70		123.26
		Chalcopyrite							51.91			34.30								35.56		121.77
		Chalcopyrite							53.48			36.49								36.34		126.31
		Chalcopyrite							53.33			34.83								35.70		123.85
		Chalcopyrite							53.70			35.96								36.34		126.00
		Chalcopyrite							49.41			31.62								33.08		114.11
		Chalcopyrite							49.79			34.45								34.21		118.45
		Chalcopyrite							47.11			117.31								32.05		196.47
	EDB190070B	Cobaltite								44.48							64.44			20.11		129.03
		Cobaltite							1.36	41.83	2.15						62.27			18.77		126.38
		Cobaltite							1.20	42.32	1.78						62.30			19.14		126.74
	EDB190054B	Cobaltpentlandite							11.99	30.61	13.31									28.39		84.30
		Cobaltpentlandite							4.67	8.80	3.87			1.43	0.49					13.68		32.94

Appendix 4. Continuation.

Mineral group	Sample	Species	Na$_2$O	K$_2$O	MgO	CaO	BaO	MnO	FeO	CoO	NiO	CuO	ZnO	PbO	SiO$_2$	V$_2$O$_5$	As$_2$O$_3$	P$_2$O$_5$	Al$_2$O$_3$	S	F	Total
Sulphides	ALZ190005A	Galena												94.74						12.06		106.80
		Galena												96.36						11.61		107.97
		Galena												92.61						11.67		104.28
	ALZ190005A	Galena												89.53						11.18		100.71
	ALZ190005A	Pyrrhotite							78.90											40.20		119.10
		Pyrrhotite							75.94											39.40		115.34
		Pyrrhotite							64.39											41.40		105.79
		Pyrrhotite							75.02											38.53		113.55
	ALZ190011A	Pyrrhotite							74.64											37.29		111.93
		Pyrrhotite							80.65											39.79		120.44
		Pyrrhotite							79.02											39.84		118.86
		Pyrrhotite							79.45											39.47		118.92
	EDB190054B	Pyrrhotite				0.53			40.24											28.32		69.09
	EDB190070B	Skutterudite							9.48	26.12	2.49						101.80			0.72		140.61
		Skutterudite							9.37	24.21	2.53						97.60			0.69		134.39
	ALZ190005A	Sphalerite						2.07	8.63				71.43							33.94		116.06
		Sphalerite						2.62	8.10				70.78							33.37		114.88
Oxides	ALZ190011A	Magnetite							92.20													92.20
		Magnetite							94.98													94.98
		Magnetite							94.82													94.82
		Magnetite							92.16													92.16

APPENDIX 5. SUMMARY OF PETROPHYSICAL DATA, VENA

Appendix 5. Results from petrophysical analysis of bedrock samples from mining waste rock and outcrop in the areas around the Vena and Dampetorp ore fields.

Sample ID	Bedrock	Density (kg/m^3)	Magnetic Susceptibility (µSI)	Natural Remanent Magnetization (mA/m)	Q-value
ALZ180008A	Rhyolite	2699.76	3419.70	189.47	1.35
ALZ180051A	Granodiorite	2702.09	284.39	46.20	3.96
ALZ180062A	Extrusive rock	2673.48	283.45	24.33	2.09
ALZ180072A	Amphibolite	2858.42	541.12	22.70	1.02
ALZ180076A	Granodiorite	2706.92	201.87	11.66	1.41
ALZ180087A	Granite	2580.01	47.08	22.80	11.82
ALZ180089A	Sulphide mineralisation	3141.30	526.30	20.76	0.96
EDB180002A	Quartz diorite	2718.20	263.77	9.62	0.89
EDB180015A	Rhyolite	2633.39	36.54	39.35	26.28
EDB180030A	Felsic rock	2697.69	245.61	37.82	3.76
EDB180035A	Extrusive rock	2704.39	373.70	38.66	2.52
EDB180054A	Extrusive rock	2772.97	847.71	557.90	16.06
EDB180071A	Volcanic rock	2726.24	384.48	46.82	2.97
PHN190001A	Granodiorite	2627.97	67.41	26.15	9.47
PHN190002A	Amphibolite	2952.85	768.79	26.73	0.85
PHN190003A	Granodiorite	2736.55	335.29	10.29	0.75
PHN190004A	Granodiorite	2711.44	321.98	10.96	0.83
PHN190005A	Volcanic rock	2672.72	201.56	29.46	3.57
PHN190007A	Volcanic rock	2731.98	367.53	31.61	2.10
PHN190008A	Granodiorite	2727.37	316.50	12.42	0.96
PHN190009A	Volcanic rock	2751.69	378.76	18.18	1.17
PHN190009B	Granodiorite	2692.32	321.80	27.95	2.12
PHN190010A	Volcanic rock	2701.82	310.00	791.42	62.29
PHN190013A	Amphibolite	2856.99	33108.39	2954.16	2.18
PHN190014A	Andesite	2833.26	676.68	22.11	0.80
PHN190014B	Amphibolite	2837.17	552.40	71.59	3.16
PHN190015A	Granodiorite	2710.78	233.04	6.92	0.72
PHN190016A	Granodiorite	2727.09	342.28	12.00	0.86
PHN190016B	Granodiorite	2716.94	331.77	30.20	2.22
PHN190018A	Composite rock, primarily mafic	2945.17	1791.00	16.54	0.23
PHN190018B	Composite rock, primarily mafic	2962.95	864.09	22.73	0.64
PHN190018C	Composite rock, primarily felsic	2727.30	322.13	51.18	3.88
PHN190019A	Composite rock, primarily mafic	2877.49	784.26	12.62	0.39
PHN190019B	Composite rock, primarily mafic	2804.40	756.49	52.43	1.69
PHN190022A	Composite rock, primarily mafic	2924.31	690.53	21.81	0.77
PHN190022B	Composite rock, primarily felsic	2751.80	2444.20	30.83	0.31
PHN190022C	Composite rock, primarily felsic	2723.02	1891.39	37.77	0.49
PHN190023A	Volcanic rock	2762.00	14120.51	715.31	1.24
PHN190023B	Volcanic rock	2760.87	1106.40	53.25	1.17
PHN190023C	Granite-Pegmatite	2640.93	12758.29	258.98	0.50

APPENDIX 6. SUMMARY OF PETROPHYSICAL DATA, TUNABERG

Appendix 6. Results from petrophysical analysis of bedrock samples from mining waste rock and outcrop in the Tunaberg ore field and surrounding area.

Sample ID	Bedrock	Density (kg/m^3)	Magnetic Susceptibility (µSI)	Natural Remanent Magnetization (mA/m)	Q-value
EDB190072A	Amphibolite	3 152.75	15 647.95	102.03	0.16
EDB190090A	Dacitoid	2 759.04	198.48	8.87	1.10
EDB190090B	Marble	2 784.73	6 364.49	250.97	0.97
EDB190090C	Calcsilicate rock	3 442.79	727.23	17.31	0.59
EDB190094A	Sulphide mineralisation	2 685.03	7 768.62	3 821.71	12.15
ALZ191049A	Sulphide mineralisation	3 819.94	546.69	187.25	8.46
ALZ191059A	Sulphide mineralisation	2 963.72	25 640.41	5 515.82	5.31
PHN191001A	Granite	2 606.06	58.22	23.24	9.85
PHN191002A	Limestone	2 823.19	243.73	21.35	2.16
PHN191002B	Volcanic rock	2 766.94	118.52	22.79	4.75
PHN191002C	Granite	2 633.18	161.76	31.18	4.76
PHN191003A	Limestone	2 853.70	9 631.45	21 136.58	54.18
PHN191003B	Limestone	2 763.64	24 493.56	20 858.73	21.02
PHN191003D	Limestone	2 982.63	310.09	47.09	3.75
PHN191005A	Limestone-Sulphide mineralisation	2 837.98	567.75	1 370.88	59.61
PHN191005B	Volcanic rock-Sulphide mineralisation	2 856.67	253.51	37.88	3.69
PHN191005C	Skarn-Sulphide mineralisation	3 233.81	840.12	36.60	1.08
PHN191006A	Limestone-Sulphide mineralisation	2 853.11	280.40	25.87	2.28
PHN191006B	Volcanic rock-Sulphide mineralisation	3 126.77	3 099.02	21 789.42	173.59
PHN191009A	Granite-Pegmatite	2 606.45	60.82	55.42	22.50
PHN191010A	Granite-Pegmatite	2 590.97	34.91	10.24	7.24
PHN191011A	Volcanic rock	2 788.20	394.51	14.52	0.91
PHN191012A	Granodiorite	2 638.92	113.50	54.58	11.87
PHN191013A	Granite	2 637.69	69.52	24.64	8.75
PHN191013B	Granite	2 928.39	913.82	11.75	0.32
PHN191013C	Granite	2 704.73	210.03	33.36	3.92
PHN191014A	Granite	2 648.50	66.41	11.65	4.33
PHN191015A	Volcanic rock	2 665.35	229.12	19.94	2.15
PHN191015B	Granodiorite	2 633.52	100.78	16.89	4.14
PHN191016A	Volcanic rock	2 823.13	356.85	11.76	0.81
PHN191017A	Volcanic rock	2 806.91	907.19	60.82	1.66
PHN191018A	Volcanic rock-Skarn	3 406.27	2 167 979.00	329 683.50	3.75
PHN191018B	Volcanic rock-Skarn	3 403.34	1 990 281.00	473 158.20	5.87
PHN191019A	Dacite-Andesite	2 896.00	1 003.00	95.28	2.35
PHN191019B	Skarn	3 421.16	1 327 917.00	403 242.70	7.50
PHN191020A	Dacite	2 649.36	127.83	7.50	1.45
PHN191020B	Rhyolite-Quartzite	2 615.63	38.92	25.31	16.06
PHN191020C	Pegmatite- Granite	2 571.08	23.77	29.22	30.35
PHN191023A	Volcanic rock	2 654.24	127.67	125.01	24.17
PHN191024A	Volcanic rock	2 720.83	132.43	39.55	7.37
PHN191024B	Volcanic rock	2 867.09	2 545.33	10 614.88	102.96
PHN191024C	Volcanic rock	3 021.84	1 739.67	5 229.99	74.22
PHN191024D	Granite	2 608.24	65.71	20.45	7.68
PHN191025A	Granite	2 626.51	37.80	32.53	21.25
PHN191025B	Granite	2 698.39	212.39	12.82	1.49
PHN191025C	Rhyolite-Dacite	2 651.70	80.74	84.35	25.79

APPENDIX 7. SUMMARY OF SPECTROMETRIC DATA, VENA

Appendix 7. Results from spectrometry measurements on outcrop in the areas around the Vena and Dampetorp ore fields.

Observation ID	Bedrock	K (%)	U (ppm)	Th (ppm)	Total
PHN190001	Granodiorite	3.600	4.950	15.087	13.063
PHN190002	Amphibolite	1.247	1.190	3.463	3.673
PHN190003	Granodiorite	3.135	3.550	17.775	12.235
PHN190004	Granodiorite	3.720	3.360	14.683	12.093
PHN190005	Volcanic rock	2.630	4.035	10.785	9.750
PHN190006	Volcanic rock	3.200	4.620	11.490	11.200
PHN190007	Volcanic rock	3.510	3.360	13.870	11.540
PHN190008	Granodiorite	3.563	3.253	19.380	13.147
PHN190010	Volcanic rock	2.783	4.067	12.517	10.507
PHN190020	Volcanic rock	5.957	2.103	13.877	14.447
PHN190021	composite mafic-felsic rock	1.840	4.483	11.177	8.957
PHN190022	composite mafic-felsic rock	2.563	6.553	17.283	13.170